



Title	Study on Cu-containing High Entropy Alloys for Nuclear Fusion Application
Author(s)	LEI, Yu
Citation	北海道大学. 博士(工学) 甲第14432号
Issue Date	2021-03-25
DOI	10.14943/doctoral.k14432
Doc URL	<a href="http://hdl.handle.net/2115/81324">http://hdl.handle.net/2115/81324</a>
Type	theses (doctoral)
File Information	Lei_Yu.pdf



[Instructions for use](#)

# Study on Cu-containing High Entropy Alloys for Nuclear Fusion Application



**HOKKAIDO UNIVERSITY**

*A thesis submitted in partial fulfilment for the degree of doctor of philosophy*

Yu LEI

Graduate School of Engineering

Hokkaido University

## Acknowledgements

At the end of my studies at Hokkaido University, I want to express my heartfelt gratitude to everyone who supported me with invaluable support during my Ph.D. studies here over three years. I know very well that I can not get a Ph.D. without their help.

Firstly, I would like to express my heartfelt gratitude to my supervisor, Professor Naoyuki Hashimoto, for giving me the chance to study for a doctorate. I know that I am not a satisfactory student who can meet the expectations of the professor. But even so, he spared no effort to provide me with guidance and help.

Secondly, I would like to give my hearty thanks to Professor Shigehito Isobe, Professor Seiji Miura, and Professor Munekazu Ohno. Professor Isobe, Thank him for helping me during my Ph.D. research. Not only did he provide research assistance, but he also always gave me confidence. Professor Seiji Miura is an erudite professor of more knowledge. I am grateful to him for sharing knowledge in the HEAs field, spending his time on discussion. Professor Ohno, I wish to express my appreciation to him for help with my graduation. He is mighty and modest in my mind.

Thirdly, I would like to thank secretary Kaori Kobayashi for providing my study and life with all kinds of assistance over the three years. I am indebted to assistant professor Hiroshi Oka for his helpful discussion and constructive suggestions. I also would like to express my appreciation to the members of the laboratory of Nano-Mirco Materials Analysis (NMA) for their support on the use of instruments. Special thanks to Specially Appointed Assistant Professor Yongming Wang for giving me TEM training and helping me whenever I encounter problems.

I also owe my sincere gratitude to all the former and present students in LOAM. I was not able to talk in Japanese when I first came to Japan.. Even so, everyone communicated with me enthusiastically, helped me solve problems in experiments and life, and invited me to a dinner

party. Many gratitude for the warmth you gave to me in a foreign land. Dr. Jingming Shi, thanks for his contribution to the simulation part of chapter 5 of the thesis.

Lastly, my thanks would go to my beloved family for their loving considerations of me all through three years.

## Abstract

At present, nuclear energy systems have acquired a great deal of expertise through the operation of reactors from generation I to generation III. With a performance target for the next 20 years, the next generation of water-cooled nuclear reactors has been planned to optimize the performance of superseded generations. Aspects such as life, protection, performance, and power production are necessarily related to their design and have been considered. These reactors require radiation doses of up to 100-200 displacements per atom (dpa) and outlet temperatures ranging from 550-850°C. The properties that the next generation of nuclear materials would possess include increased resistance to irradiation, swelling, relaxing, growth, and corrosion. No high radiation resistance austenitic stainless steels are currently eligible for extended use at high temperatures for the next generation of nuclear energy systems. High entropy alloys (HEAs) have acquired substantial interest due to their outstanding mechanical properties, good corrosion resistance, and high tolerance to irradiation. Thus, one of the candidate materials for next-generation nuclear reactor components could be FCC type HEAs. It is noticeable that most of the reported HEAs contained cobalt. Considering a candidate HEA for nuclear application, the radioactive elements should be eliminated from the material design based on radiation shielding requirements. This dissertation contains research work attempting to prepare new face-centered cubic Co-free Cu-containing solid solution concentrated alloys, Cu, CuNi, CuNiFe, Cu<sub>0.3</sub>NiFeCr, Al<sub>0.4</sub>CuFeCrNi<sub>2</sub>, and evaluate their properties. Experimental and computational methods have been employed and their microstructure, hardness, tensile strengths, and irradiation effects at 500°C were investigated.

First of all, face-centered cubic Co-free Cu-containing solid solution concentrated alloys, CuNi and CuNiFe alloys of the equal molar ratio were prepared by arc-melting, and Cu<sub>0.3</sub>NiFeCr and Al<sub>0.4</sub>CuFeCrNi<sub>2</sub> alloys were prepared by induction furnace in a high purity argon atmosphere. The investigation by X-Ray diffractometer (XRD), scanning electron microscope (SEM), and energy dispersive spectroscopy (EDS) were conducted for as-cast and annealed samples. Mechanical properties were also investigated by Vickers microhardness test and tensile test. All the as-cast alloys were identified as single-phase FCC alloys by X-ray diffraction analysis.

While, the SEM observation indicated a new Cr-rich phase with Cu-rich phase in the annealed  $\text{Cu}_{0.3}\text{NiFeCr}$  alloy, which is probably due to the low solubility of Cr and Cu in the alloy. After annealing at 1076 °C for 120 hours,  $\text{Cu}_{0.3}\text{NiFeCr}$  alloy became a single-phase FCC. Mechanical property examinations indicated the severe lattice distortion in HEA has effects on mechanical properties. The general solid solution effects lead to the highest Vickers hardness and tensile strength in the  $\text{Al}_{0.4}\text{CuFeCrNi}_2$ .

Secondly, in order to understand the irradiation effects and the impact of the compositional complexity in Co-free high entropy alloys, high purity Cu-containing solid solution concentrated alloys, CuNi,  $\text{Cu}_{0.3}\text{NiFeCr}$ ,  $\text{Al}_{0.4}\text{CuFeCrNi}_2$  without apparent pre-existing defect sinks were conducted in-situ ion irradiation experiments with 1 MeV Krypton ion irradiation at 500 °C up to 1 dpa. The irradiation effects were assessed through the measurement of the defect type, defect density and defect size. The Orowan equation was applied to estimate the irradiation hardening contributed by stacking fault tetrahedra (SFT), black dot (BD) and Frank loop (FL). In-situ electron irradiation experiment showed that CuNi,  $\text{Cu}_{0.3}\text{NiFeCr}$  alloys but  $\text{Al}_{0.4}\text{CuFeCrNi}_2$  present SFTs. The irradiation introduced a high density of SFTs in CuNi alloy. The high entropy alloy ( $\text{Al}_{0.4}\text{CuFeCrNi}_2$ ) had the smallest FL size (the highest density), followed by  $\text{Cu}_{0.3}\text{NiFeCr}$  and then CuNi. It reported that the key parameters for the formation of SFTs and FLs are the stacking fault energy (SFE) and the shear modulus. The smaller the ratio of the SFE to the shear modulus, the easier it is to form SFT and large size FLs. The lowest density of SFTs and the smallest FL size in HEA ( $\text{Al}_{0.4}\text{CuFeCrNi}_2$ ) can be inferred to have a large ratio of the SFE to the shear modulus. In addition, the lowest estimated irradiation hardening in HEA ( $\text{Al}_{0.4}\text{CuFeCrNi}_2$ ) than in 316H SS indicated the potential for the nuclear application of Co-free high-entropy alloy at 500°C.

At last, the first-principles DFT calculations have been conducted to explore the properties and formation energies of point defects (The monovacancy and self-interstitial) in the face-centered cubic Co-free alloys, CuNi, CuNiFe, CuNiFeCr, and  $\text{Cu}_{0.3}\text{NiFeCr}$ . The consistency of the results of the XRD measurements and the first estimations confirms the validity of the

calculation. Calculated coherent energy and formation enthalpy for CuNi, CuNi, CuNiFeCr, and Cu<sub>0.3</sub>NiFeCr alloys indicates that the face-centered Co-free alloys we have developed are stable alloys. And the strongest structural corrugation in equimolar HEA (CuNiFeCr) suggests that higher entropy is a stronger local structural disorder. Also, the computed defect energy (interstitial formation energy:  $E_i^f$ ) and the vacancy formation energy:  $E_v^f$  of the Cu and Ni atoms in these alloys indicate that the different elements can have different energy effects, which may also suggest that the selection of the elements can't be random when developing a high entropy alloy and that not all the elements can be influenced by the value of the entropy. Furthermore, DFT calculation showed that impurity effects should not be ignored when HEA was used as a nuclear reactor component because those light elements could affect microstructural evolution behaviour in HEAs.

This work has indicated that high purity Co-free Cu-containing high-entropy alloys are potential candidate materials for nuclear fusion reactors at higher operation temperatures.

# Contents

Acknowledgements .....	i
Abstract.....	iii
Chapter 1 Introduction.....	1
1.1 New generation energy system .....	2
1.2 A short overview of nuclear materials .....	4
1.3 High-entropy alloys.....	6
1.3.1 Definitions and microstructures .....	6
1.3.2 Mechanical properties .....	7
1.3.3 Irradiation resistance .....	9
1.3.4 Simulation of HEAs .....	12
1.4 Objective of this study.....	14
Chapter 2 Methodology.....	15
2.1 Vacuum melting .....	16
2.2 X-ray fluorescence (XRF) spectrometry .....	18
2.3 X-ray diffraction.....	19
2.4 Scanning electron microscopy .....	21
2.5 Transmission electron microscopy.....	23
2.6 Ion irradiation .....	25
2.7 Density Functional Theory Calculation .....	27
Chapter 3 Microstructure and mechanical properties in Cu-containing high entropy alloys .....	28
3.1 Introduction .....	29



3.2 Fabrication of single-phase face-centered cubic Co-free Cu-containing alloys.....	31
3.3 Microstructure analysis .....	36
3.4 Vickers hardness.....	42
3.5 Tensile strength .....	43
3.6 Summary .....	45
Chapter 4    Irradiation effects at 500°C in Cu-containing HEAs.....	46
4.1 Introduction .....	47
4.2 Kr ions irradiation experiment .....	48
4.3 Irradiation effects on microstructure .....	51
4.4 Irradiation hardening .....	61
4.5 Summary .....	63
Chapter 5    Computational approach on the stability of HEAs by the first-principles DFT calculations .....	64
5.1 Introduction .....	65
5.2 Calculation method .....	67
5.3 Fundamental properties of CuNi, CuNiFe, CuNiFeCr and Cu <sub>0.3</sub> NiFeCr alloys .....	68
5.4 Magnetic and electronic properties of CuNi, CuNiFe, CuNiFeCr and Cu <sub>0.3</sub> NiFeCr alloys.....	73
5.5 Monovacancy and self-interstitial in CuNi, CuNiFe, CuNiFeCr and Cu <sub>0.3</sub> NiFeCr alloys.....	76
5.6 Physical properties of CrCoFeNi HEA .....	79
5.7 Dissolution of H, He, C and N in CrCoFeNi HEA .....	81
5.8 Effect of H, He, C and N on the physical properties of CrCoFeNi HEA .....	86

5.9 Summary .....	90
Chapter 6    Conclusions .....	91
References .....	96

# List of Figures

Figure 1.1	Primary energy consumption by the source of the world. ....	2
Figure 1.2	Irradiation-induced void distribution. (a) Cross-sectional TEM images of nickel, NiCo, NiFe and NiCoFeCr irradiated with 1.5 MeV Ni <sup>+</sup> ions to $3 \times 10^{15} \text{ cm}^{-2}$ at 773 K, scale bars in the zoomed images are 50 nm. (b) Cross-sectional TEM images of nickel, NiFe, NiCoFe and NiCoFeCrMn irradiated with 3 MeV Ni <sup>+</sup> ions to $5 \times 10^{16} \text{ cm}^{-2}$ at 773 K. The ions enter the specimen from the top of the images [45]. ....	10
Figure 1.3	(a) The hardness measured by nanoindentation for the as-received and irradiated Al <sub>0.3</sub> CoCrFeNi, CoCrFeMnNi and 316H SS to 1 dpa. The error bar is equal to one standard deviation. (b) The hardness increases of the three materials after irradiation to 1 dpa. (c) The relative hardness increases of the three materials after irradiation to 1 dpa. The error bar in (b) and (c) are uncertainty propagation calculated from the error bar in (a). (d) Calculated increase in yield strength using Orowan equation [46] .....	11
Figure 2.1	Arc melting furnace with an enclosed crucible .....	17
Figure 2.2	X-Ray Diffractometer and standard Bragg-Brentano experimental XRD setup .	20
Figure 2.3	Schematic drawing of the electron and x-ray optics of a combined SEM-EPMA as searched in Web of Geochemical Instrumentation and Analysis .....	22
Figure 2.4	Intermediate Voltage Electron Microscopy-Tandem as searched in Web of Argonne national laboratory.....	26
Figure 3.1	Cu-Ni phase diagram [79].....	32
Figure 3.2	Ternary phase diagram Cu-Fe-Ni at 1273 K: 1 – single-phase alloy, 2 – two-phase alloy. The miscibility gap based on experimental results and thermodynamic reassessment [80] .....	32
Figure 3.3	Typical SEM-BEC images of as-cast CuNiFeCr.....	33
Figure 3.4	XRD patterns for the as-cast Al <sub>x</sub> CrCuFeNi <sub>2</sub> alloys [57]. ....	34
Figure 3.5	XRD patterns for the Co-free Cu-containing solid solution concentrated alloys	37
Figure 3.6	Typical SEM-BEC images and EDS Mapping images of solution annealed Al <sub>0.4</sub> CuFeCrNi <sub>2</sub> .....	38
Figure 3.7	Typical SEM-BEC images of Al <sub>0.4</sub> CuFeCrNi <sub>2</sub> at different magnifications (X5000, X1000, and X200).....	39
Figure 3.8	Typical SEM BEC images and the EDS Mapping of (a) as-cast and (b) 1000 °C /24h annealed Cu <sub>0.3</sub> NiFeCr alloy.....	41
Figure 3.9	Typical SEM-BEC images of Cu <sub>0.3</sub> NiFeCr annealed at 1076°C for (a) 24, (b) 48, (c) 72 and (d) 120 hours. ....	41
Figure 3.10	Vickers Hardness of all the alloys of as-cast and solution-annealed for 24 hours. ....	42

Figure 3.11 Stress-strain curves of all the solution-annealed alloys, 316H, and CuCrZr as a comparison. ....	44
Figure 4.1 SRIM plots showing the calculated damage (blue line) and implanted ion profiles (black line) of 1 MeV Krypton ions in CSAs normalized to an ion fluence of $6.3 \times 10^{14}$ ions/cm <sup>2</sup> . ....	50
Figure 4.2 The BF (top) and WBDF (bottom) TEM micrographs of CuNi irradiated with 1 MeV Kr ions at 500 °C. The WBDF diffraction condition was $g = 200$ ( $g, 5g$ ) at 011zone. ....	52
Figure 4.3 The BF (top) and WBDF (bottom) TEM micrographs of Cu <sub>0.3</sub> NiFeCr irradiated with 1 MeV Kr ions at 500 °C. The WBDF diffraction condition was $g = 200$ ( $g, 5g$ ) at 011zone. ....	53
Figure 4.4 The BF (top) and WBDF (bottom) TEM micrographs of Al <sub>0.4</sub> CuFeCrNi <sub>2</sub> irradiated with 1 MeV Kr ions at 500 °C. The WBDF diffraction condition was $g = 200$ ( $g, 5g$ ) at 011zone. ....	54
Figure 4.5 Bright-field TEM images and the size distribution of SFTs, black dots, and Frank loops in CuNi irradiated with 1 MeV Kr ions at 500 °C to 1 dpa. Micrographs were taken of the foil at 011zone where $g = 111$ was strongly reflected. ....	56
Figure 4.6 Bright-field TEM images and the size distribution of SFTs, black dots, and Frank loops in Cu <sub>0.3</sub> NiFeCr irradiated with 1 MeV Kr ions at 500 °C to 1 dpa. Micrographs were taken of the foil at 011zone where $g = 111$ was strongly reflected. ....	56
Figure 4.7 Bright-field TEM images and the size distribution of SFTs, black dots, and Frank loops in Al <sub>0.4</sub> CuFeCrNi <sub>2</sub> irradiated with 1 MeV Kr ions at 500 °C to 1 dpa. Micrographs were taken of the foil at 011zone where $g = 111$ was strongly reflected. ....	57
Figure 4.8 Number density and average size of stacking fault tetrahedra (SFTs), black dots and Frank loops in CuNi, Cu <sub>0.3</sub> NiFeCr, and Al <sub>0.4</sub> CuFeCrNi <sub>2</sub> irradiated with 1 MeV Kr ions at 500 °C to 1 dpa. ....	58
Figure 5.1 XRD patterns of annealed CuNi, CuNiFe, CuNiFeCr and Cu <sub>0.3</sub> NiFeCr alloys. ....	69
Figure 5.2 Structural corrugation in (100), (110) and (111) plane of CuNi, CuNiFe, CuNiFeCr and Cu <sub>0.3</sub> NiFeCr alloys. ....	72
Figure 5.3 Charge transfer of each solute atom in (a)CuNi, (b)CuNiFe, (c)CuNiFeCr and (d)Cu <sub>0.3</sub> NiFeCr alloys. ....	73
Figure 5.4 Magnetic moment of each solute atom in (a)CuNi, (b)CuNiFe, (c)CuNiFeCr and (d)Cu <sub>0.3</sub> NiFeCr alloys. ....	74
Figure 5.5 The defect energy of Cu and Ni atoms in CuNi, CuNiFe, CuNiFeCr and Cu <sub>0.3</sub> NiFeCr alloys. ....	77
Figure 5.6 The vacancy formation energy for Cu and Ni atomic positions in CuNi, CuNiFe, CuNiFeCr and Cu <sub>0.3</sub> NiFeCr alloys. ....	78
Figure 5.7 The magnetic moment (a) and charge transfer (b) of each solute in CrCoFeNi HEA. ....	80

Figure 5.8	The dissolution energy of H, He, C and N in CrCoFeNi HEA.....	83
Figure 5.9	The number of solutes (Cr, Co, Fe and Ni) located at the first coordination shell of H (a), He (b), C (c) and He (d), and the average bond length between interstitial atoms and solutes (e) .....	85
Figure 5.10	The magnetic moment of Cr (a), Co (b), Fe (c) and Ni (d) next to interstitial in CrCoFeNi HEA and the charge transfer of interstitial atoms (e).....	87
Figure 5.11	The projected density of states of Cr, Co, Fe and Ni of d-state in HEA without interstitial (a), s-state of H (b) and He (c), p-state of C (d) and N (e), and the nearest Cr, Co, Fe and Ni of d-state. ....	889

# List of Table

Table 1.1	Tensile properties of HEAs [32] .....	8
Table 3.1	EDS analysis of as-cast CuNiFeCr focused on areas [001] and [0072].....	33
Table 3.2	The nominal chemical composition (at%) of Co-free Cu-containing alloys .....	35
Table 3.3	Solution annealing conditions of Co-free Cu-containing alloys .....	35
Table 3.4	The values of ultimate strength, yield strength ( $\sigma_{0.2}$ ) and elongation of the alloys .....	44
Table 4.1	The nominal chemical composition (at%) of Co-free Cu-containing alloys .....	49
Table 4.2	Electro-polishing conditions of Co-free Cu-containing alloys .....	49
Table 4.3	Kr ion irradiation conditions of Co-free Cu-containing alloys .....	49
Table 4.4	Mean diameter and number density of SFTs, black dots, Frank loops, and hardness measured of Co-free Cu-containing alloys.....	62
Table 5.1	Lattice constant, cohesive energy and formation enthalpy of CuNi, CuNiFe, CuNiFeCr and Cu <sub>0.3</sub> NiFeCr alloys .....	70
Table 5.2	The calculated lattice constant of CrCoFeNi HEA in comparison with the previous studies. ....	79
Table 5.3	The calculated average dissolution energy (eV) of H, He, C and N at T site and O site in CrCoFeNi HEA. ....	82

# Chapter 1

---

## Introduction

---

## 1.1 New generation energy system

The utilization of energy is regarded as the key to human civilization, which enables humankind to build their society. As technology develops, the efficiency of energy utilization has made great progress, humankind has been using energy from nature like wind power, hydropower, and solar power for thousands of years. However, fossil fuels like coal, petroleum, and natural gas are still the main energy sources, see Figure 1.1, and these fossil fuels are believed to exhaust in several hundreds of years [1]. Besides, fossil fuel could lead to global warming because its combustion releases plenty of carbon dioxide which causes the greenhouse effect. Global warming is regarded to cause severe local climate disasters and climate change which not only threatens the survival of plants and wild animals but also threatens human society [2]. Thus, it is necessary to solve energy problems to ensure the sustainability of human development, one solution is to develop nuclear energy resources.

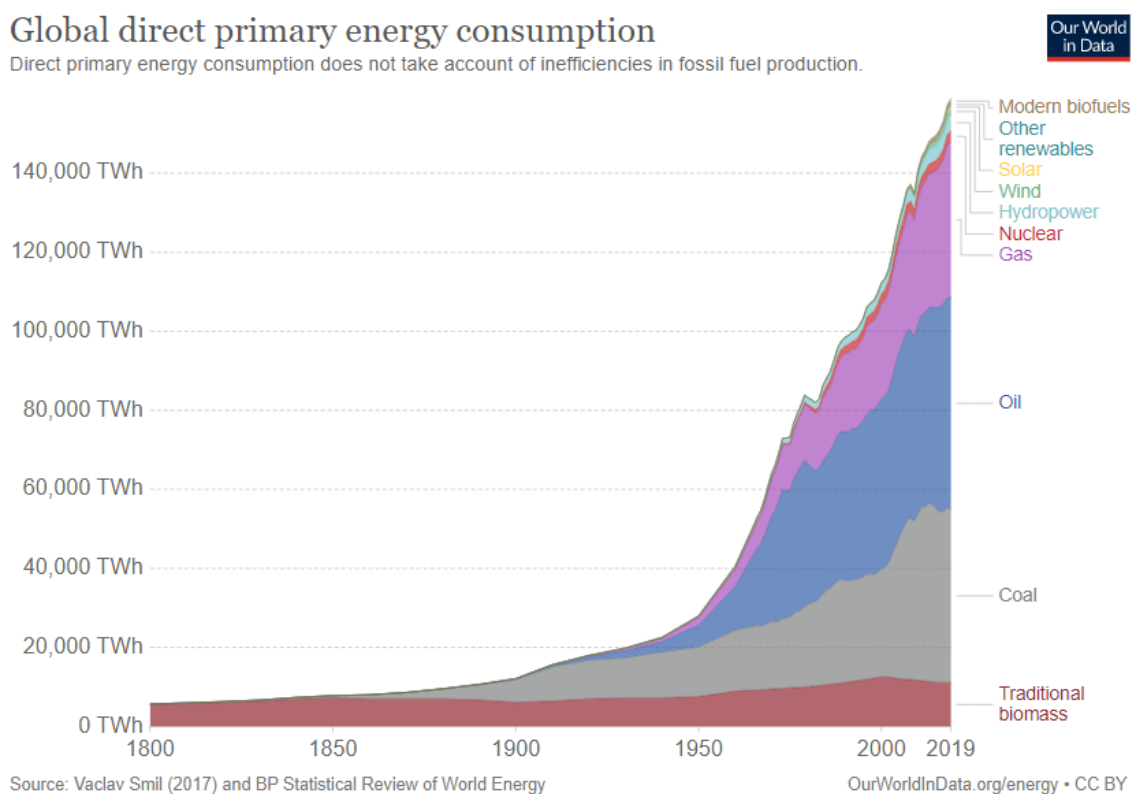


**Figure 1.1 Primary energy consumption by the source of the world.**



At present, nuclear energy systems have acquired a great deal of expertise through the operation of reactors from generation I to generation III and the design of reactors dominated by water-cooled reactors[3]. With a performance target for the next 20 years, the next generation of water-cooled nuclear reactors has been planned to optimize the performance of superseded generations. Aspects such as life, protection, performance, and power production are necessarily related to their design and have been considered from the outset. Next-generation nuclear energy systems include the lead-cooled fast reactor (LFR), the gas-cooled fast reactor (GFR), the sodium-cooled fast reactor (SFR), the molten salt reactor (MSR) and the supercritical-water-cooled reactor (SCWR) as well as smaller, compact reactor designs such as the pebble bed reactor (PBR). These reactors require radiation doses of up to 100-200 displacements per atom (dpa) and outlet temperatures ranging from 550-850 ° C, and new corrosion problems are emerging both in MSR and SCWR [4]. Although the technical advancement of fusion reactors is relatively low, the performance criteria for containment materials are similar. The properties that the next generation of nuclear materials must possess include enhanced resistance to irradiation, dimensional stability under irradiation, swelling, relaxation, growth, and corrosion. Besides, the expense of manufacturing and running the life of the components in each reactor design must also be taken into account [5]. No high radiation resistant austenitic stainless steels are currently eligible for prolonged use at elevated temperatures for the next generation of nuclear energy systems. One of the candidate materials for next-generation nuclear reactor components could be FCC type HEAs. Some recent papers have reported the initial examination of the fundamental irradiation behavior in HEAs [6,7], thereby giving insight into the potential of those materials for nuclear applications.

## 1.2 A short overview of nuclear materials

Many materials for use in nuclear reactors, both in-core and out-of-core elements, have been developed in recent decades, such as Fe, Ti, Zr alloys,  $\text{ZrO}_2$ , Ni-alloys, SiC-based ceramics [8-10], and low-alloy ferritic-steels [11]. Because materials will undergo property changes that are different from normal applications after being irradiated, there are some special requirements for nuclear materials. Ni alloys have been reported to have excellent corrosion resistance and high-temperature mechanical properties. Since they display better creep-rupture strength at high temperatures, they are sometimes preferred over steels for use in high-temperature structural applications [12]. There is no phase transition in Ni alloys. The formation of dispersed intermetallics is aimed to increase strength [13]. The Ni-based alloys, therefore, are currently for use in very-high-temperature reactors as turbine blades [14]. However, the relatively large thermal neutron cross-section and associated with Ni's hydrogen affinity limit the applications of these alloys as a cladding material.

Stainless steels, which have very strong mechanical properties and corrosion resistance extending to high temperatures, are commonly used for structural applications. For example, the 18-8 series of stainless steels with a lot of accumulated data on irradiation properties are used as structural materials in fast-breeding reactors in various countries. However, there is a major downside of swelling after a dosage of more than 100 dpa in this form of substance. Other materials such as (2-12)-Cr ferric steels which have a lower irradiation swelling were considered to affect the mechanical properties of the materials to solve the swelling. The swelling under the same irradiation conditions of ferric steels as (2-12)-Cr ferric steels could be almost of a degree smaller than in austenitic stainless steels [15]. Yet there are other disadvantages of ferric steel. They have a poor resistance at high temperatures, and the DBTT of ferric steels has a large rise after irradiation [16]. Some high strength ferritic and martensitic

steels, such as (9-12) Cr-Mo-V-Nb steels and 9Cr-2Mo steels, were produced in Japan in the 1970s to solve the problem of low strength in high temperature and increased DBTT after irradiation. Ever around 1985, there have been questions over radioactivity induced by neutron irradiation. Around the same time, the disposal of fuel and the decommissioning of reactors have begun to be troublesome, and the production of nuclear materials has begun to be important to resolve these problems. After irradiation, Mo and Nb shape long-lived nuclides such that they are substituted by W, V, Ti, which form comparatively shorter-lived nuclides after irradiation in ferritic steel. Japan Atomic Energy Agency (JAEA) produced F82H steels (8Cr-2W-0.2V-0.04 T ferritic/martensitic steels) by analyzing different variables in a systematic manner. F82H has better strength at high temperatures and better DBTT behavior after irradiation [17,18]. Due to these advantages, it became the first primary candidate for the first wall and blanket structural material in the DEMO reactor.

## 1.3 High-entropy alloys

### 1.3.1 Definitions and microstructures

Initial findings were published in 2004 on high entropy crystalline alloys [8,19-22], but history studies started much earlier [23]. The latest ideas of this approach capacity to affect the consistency of the solid solution process by regulating the configuration entropy, which has caught the interest and efforts of increasing numbers in the materials science community. This field is distinguished by numerous unexplained outcomes, new discoveries, vigorous debate, and new philosophical concerns. Several points of view sets and compilations [24-27] and two books [23,28] have been written.

The entropy-based description results in more complexity and logical difficulties as entropy-based and composition-based definitions are taken together. These problems are deepened by mixing concepts with the expected result of the development of single-phase SS alloys. The entropy for a random ideal solid solution can be calculated by:

$$\Delta S_{mix} = -R \sum_{i=1}^N C_i \ln C_i \quad (1.1)$$

where R is the ideal gas constant, N is the number of components, and  $C_i$  is the atomic fraction of component i. Some studies defined as HEA must be equimolar or single-phase and others defined to include 4 component systems and alloys with  $S^{SS,ideal} > 1.36R$  or  $S^{SS,ideal} > 1.5R$  [29]. However, HEAs were defined as "those consisting of five or more main elements in equimolar ratios" and "principal elements with a concentration of each element between 35 and 5 at.%. The criterion for equimolar concentrations is limiting, thus, HEAs do not need to be equimolar, raising the number of HEAs considerably. HEAs can also contain minor elements to change the properties of the HEA base and to further increase the number of HEAs [29]. This composition-based definition prescribes elemental concentrations only and places no bounds on the

magnitude of entropy, and this definition further places no requirement on the presence of a single-phase solid solution (SS) [30].

The HEA area proposes new ideas to investigate the enormous realm of hyper-dimensional complex composition space and to control configurational entropy by alloy composition in order to favor solid solution (SS) alloys. It is well known that solid solution hardening is an important reinforcement mechanism, and some studies have stated that intermetallic (IM) phase alloys embrittle and make processing difficult, whereas SS alloys are engineered to be strong and maintain ductility and damage tolerance [19,29,31]. Thus, the HEA sector has come to put a heavy focus on the search for single-phase solid solutions.

### **1.3.2 Mechanical properties**

Mechanical properties are strongly dependent on microstructure and composition. Composition sets out atomic interactions and elastic properties that determine dislocation behaviors. The composition also determines the phases present and their volume fractions which affect the properties of the phases by their inherent properties.

A lot of HEAs tensile data is being analyzed, see Table 1.1 [32]. Most of the studies mentioned here demonstrate tensile properties after thermo-mechanical processing and annealing in order to create a uniform, even, recrystallized microstructure that enhances the efficiency of the results. Mechanical properties of the CoCrFeMnNi alloy have been analyzed in detail [33-39]. The research agreement is fairly good after accounting for variations in strain and grain size, see Table 6. Microstructures have been found to be single-phase FCC stable solutions, with the exception of small oxides [35], Mn-rich or Cr-rich second-phase particles [33].

**Table 1.1 Tensile properties of HEAs [32]**

Alloy	Processing <sup>a</sup>	Microstructure <sup>a</sup>	$\dot{\epsilon}$ (s <sup>-1</sup> )	T (°C)	$\sigma_y$ (MPa)	$\sigma_{uts}$ (MPa)	$\epsilon$ (%)
Al <sub>0.3</sub> CoCrFeNi (7.0 at.% Al)	AC	FCC + L1 <sub>2</sub>	$4 \times 10^{-4}$	23	224 ± 51	434 ± 94	48 ± 10
	AC, 700°C/72 h/WQ	FCC + L1 <sub>2</sub>	$4 \times 10^{-4}$	23	310	525	44
	AC, 900°C/72 h/WQ	FCC + B2+L1 <sub>2</sub>	$4 \times 10^{-4}$	23	240	570	45
	Bridgman casting	SX near [001]	$4 \times 10^{-4}$	23	185	399	~80
Al <sub>0.5</sub> CoCrCu <sub>0.5</sub> FeNi <sub>2</sub> (8.3 at.% Al)	AC	FCC + L1 <sub>2</sub>	$3.3 \times 10^{-3}$	23	357	459	9
				500	315 ± 12	334 ± 1	0.7 ± 0.3
	AC, 700°C/5 h/SC	FCC + L1 <sub>2</sub> +Cr-rich IM at GB	$3.3 \times 10^{-3}$	23		365	0.1
	AC, 1150°C/5 h/WQ	FCC + L1 <sub>2</sub>	$3.3 \times 10^{-3}$	500		310 ± 2	0.02
				23	215	489	39
Al <sub>0.5</sub> CoCrCuFeNi (9.1 at.% Al)	AC	FCC + FCC	$1 \times 10^{-3}$	23	360	707	19
				23	1284	1344	7.6
				23	655	800 ± 30	29 ± 1
				300	460 ± 90	600 ± 50	6 ± 2
				400	500	590 ± 20	4 ± 2
				500	430 ± 20	450 ± 50	2 ± 2
				600	270 ± 20	310 ± 40	3 ± 1
				700	170 ± 40	190 ± 30	13 ± 4
Al <sub>0.5</sub> CrCuFeNi <sub>2</sub> (9.1 at.% Al)	AC, CR 43%	FCC + FCC	$1 \times 10^{-3}$	23	363 ± 60	500 ± 20	16 ± 7
					630 ± 270	922 ± 240	4.2 ± 1.3
					704 ± 180	1088 ± 20	5.6 ± 3.2
					360 ± 100	639 ± 5	3.4 ± 0.4
AlCoCrCuFeNi (16.7 at.% Al)	AC	BCC + FCC + B2+L1 <sub>2</sub>	$1 \times 10^{-3}$	20	790	790	0.2
				600	648	551	0.4
				700	350	360	4.7
				800	161	180	12.1
				900	88	100	30
	AC, 960°C/50 h, a-b-c forged at 950 °C	BCC/B2+FCC + FCC+σ	$1 \times 10^{-3}$	1000	37	44	77
				20	1040	1170	1.0
				300	810	880	0.4
				600	300	350	1.3
				700	63	91	63

In the early stages ( $\epsilon \leq 2.4$  percent), deformation in CoCrFeMnNi occurs by planar dislocation glide on  $1/2\langle 110 \rangle$  structures that are common for FCC metals [36]. Stacking faults are often sometimes used, indicating that dislocations of  $1/2\langle 110 \rangle$  dissociate into partial dislocations of  $1/6\langle 112 \rangle$ . Dislocations lose their planar character after plastic strains of  $> 20$  percent at  $T \geq 300$  K and assemble into cell structures that are common for FCC metals. When  $\epsilon \geq 20$  percent [33,36] and after plane-strain rolling at 77 K and 293 K [40], substantial deformation via nano-twinning is seen in tension at 77 K. To improve the alloy work-hardening and to delay necking, prolific nano-twinning is recommended, leading to increases in  $\sigma_{uts}$  and  $\epsilon$  [34,36]. At low strains below RT, nano-twinning is not observed and can thus not justify the rise in  $\sigma_y$  with declining T, which is instead suggested to arise from an inherent solvent effect in FCC metals.

### 1.3.3 Irradiation resistance

Currently, the irradiation resistance of austenitic stainless steel is often widely considered. Only a handful of irradiation studies have been conducted on HEAs, most of which are CoCrFeMnNi-type high-entropy alloys. It is thought that some improvement in the irradiation resistance of HEAs should be expected due to the strongly reduced diffusivity and distorted lattice in HEAs, which could immobilize the irradiation-induced point defects and hinder the clustering of defects. Immobilization of point defects is one of the proposed alternatives to the production of radiation-resistant components, as suggested by Zinkle and Snead [41]. Experimentally, HEAs were seen to exhibit less radiation-induced segregation (RIS) than conventional Fe-Cr-Ni alloys [42]. Also, radiation and swelling damage have been shown to decrease with increasing compositional complexity [43-45], see Figure 1.2. Besides, irradiation effects on  $\text{Al}_{0.3}\text{CoCrFeNi}$  and  $\text{CoCrMnFeNi}$  high-entropy alloys and 316H stainless steel at 500 °C have been reported [46]. The irradiation at 500 °C resulted in an ordered L12 phase transformation in the  $\text{Al}_{0.3}\text{CoCrFeNi}$ . No phase transformation was observed in the CoCrFeMnNi and 316H SS. The  $\text{Al}_{0.3}\text{CoCrFeNi}$  has the largest loop size, followed by the CoCrFeMnNi and 316H SS, and the 316H SS has the largest loop density, followed by the CoCrFeMnNi and  $\text{Al}_{0.3}\text{CoCrFeNi}$ . More importantly, as shown in Figure 1.3, the nanoindentation results indicate that the irradiation hardening at 500 °C was less in the HEAs than in the 316H SS, which provides a promising sign for the applications of HEAs at high-temperature nuclear reactors.

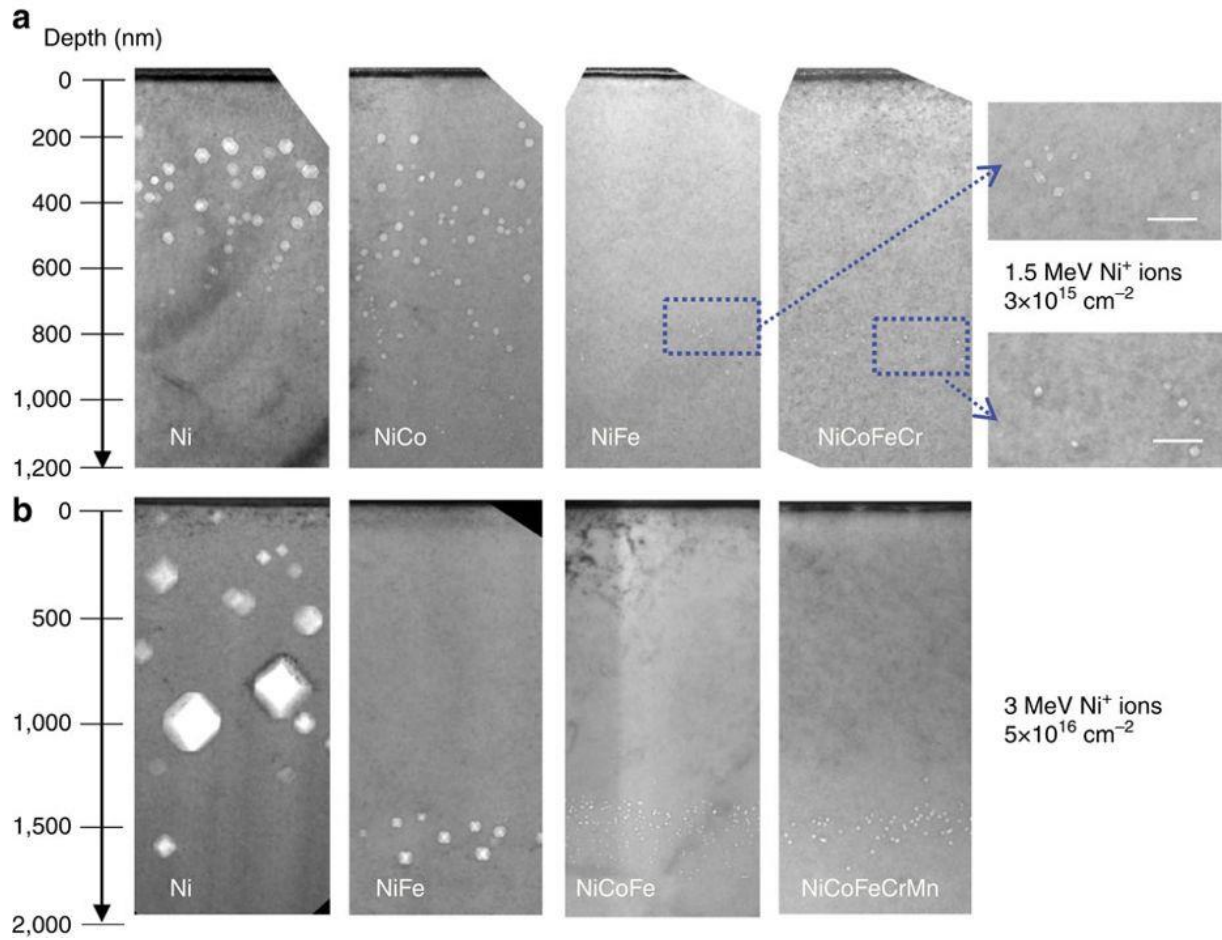


**Figure 1.2** Irradiation-induced void distribution. (a) Cross-sectional TEM images of nickel, NiCo, NiFe and NiCoFeCr irradiated with 1.5 MeV Ni<sup>+</sup> ions to  $3 \times 10^{15} \text{ cm}^{-2}$  at 773 K, scale bars in the zoomed images are 50 nm. (b) Cross-sectional TEM images of nickel, NiFe, NiCoFe and NiCoFeCrMn irradiated with 3 MeV Ni<sup>+</sup> ions to  $5 \times 10^{16} \text{ cm}^{-2}$  at 773 K. The ions enter the specimen from the top of the images [45].



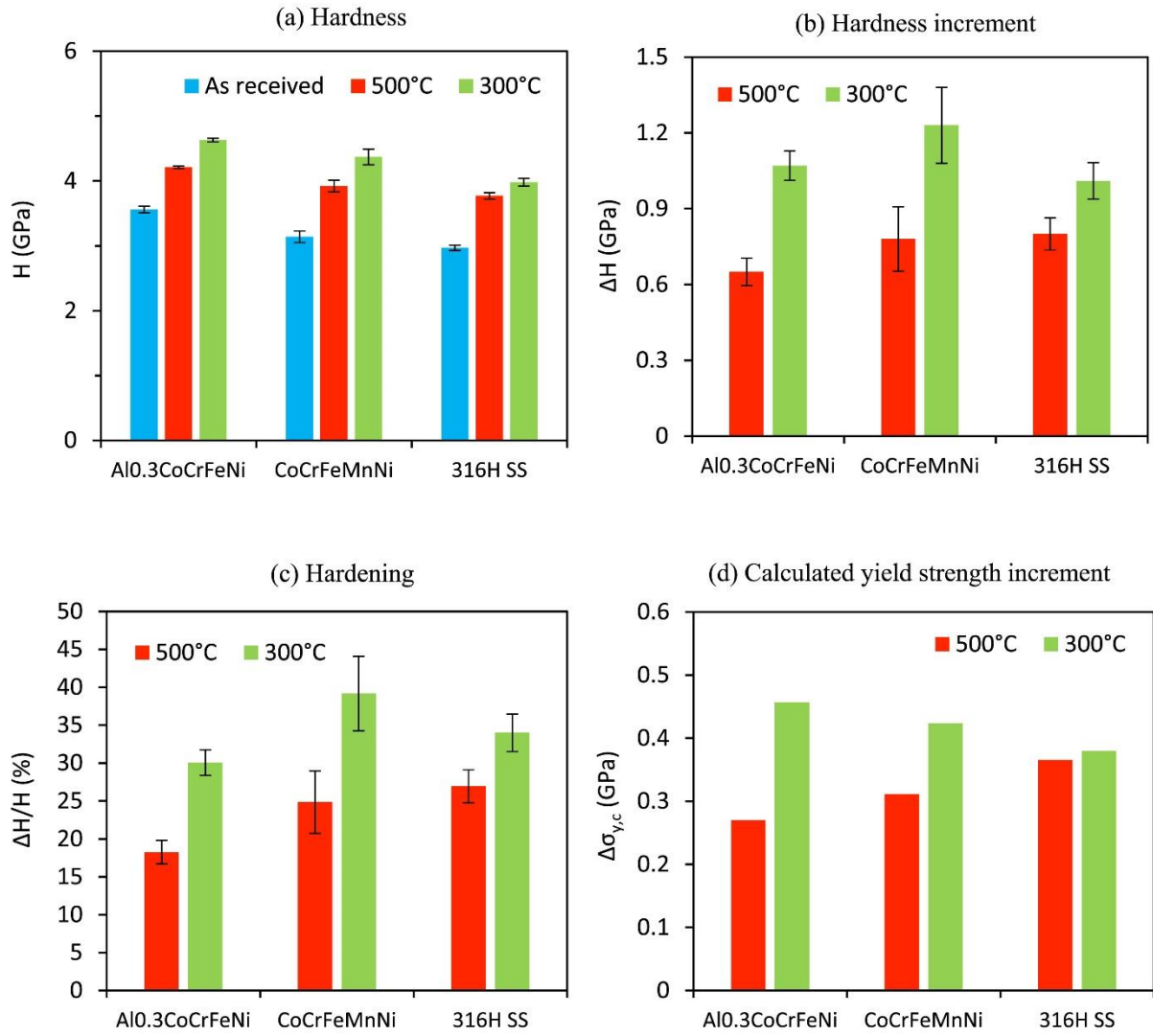


**Figure 1.3** (a) The hardness measured by nanoindentation for the as-received and irradiated Al<sub>0.3</sub>CoCrFeNi, CoCrFeMnNi and 316H SS to 1 dpa. The error bar is equal to one standard deviation. (b) The hardness increases of the three materials after irradiation to 1 dpa. (c) The relative hardness increases of the three materials after irradiation to 1 dpa. The error bar in (b) and (c) are uncertainty propagation calculated from the error bar in (a). (d) Calculated increase in yield strength using Orowan equation [46] .

Although Co-based alloys probably constitute a good solution for the use in nuclear reactors. Unfortunately, the neutron irradiation leads to activation of Co which becomes radioactive, leading to increase radiation shielding requirements during handling during the reprocessing

and the maintenance of such elements. Therefore, the nuclear industry is still looking for successors of those alloys.

#### **1.3.4 Simulation of HEAs**

First-principles methods (mainly density functional theory DFT) provide the material properties, which then serve as input to “mechanistic theory”. DFT can be and has been, used to compute the fundamental material properties such as lattice constants, elastic constants, stacking fault energies and Gamma surfaces, vacancy formation energies, and migration barriers, and cohesive energies as a function of composition and crystal structure. Performing such calculations in systems with magnetic elements remains difficult, and various approaches are being developed [47]. Stacking fault energies pose a particular challenge, and results to date vary considerably for some important systems [48,49]. It is stated at its stage that normal spin-polarized DFT using standard exchange-correlation potentials is well known to vary from experiments in certain substantial amounts. Atomic quantities of the elements, for example, often deviate from tests by modest proportions. This can lead to errors in the calculation of solute failure volumes, atom-atom spacing, and other quantities, such as the stacking of fault energies. Alternative functionals can offer various volumes, but consistent errors remain throughout the components. Elastic constants can also be mistaken, the most noticeable error being the estimation of the  $C_{44}$  scissor module in the BCC elements; this may lead to unexplained errors when calculating other mechanical properties or defects. Thus, while first-principle approaches offer the fastest route to chemically-precise atomic energy, the quantitative effects of computationally-feasible methods such as DFT must still be carefully considered [32,50].

Based on the PAW method, GPAW is now a stable and fairly mature real-space realization of DFT and TDDFT. For rapid computations of more limited accuracy, a localized atomic orbital basis is available in addition to the grid-based description. Several features have been introduced, including a wide range of functionals for exchange-correlation. The code is currently being developed by an expanding community of developers based mainly in Denmark, Finland, Sweden, and Germany, with users from all over the world eligible [51].

Atomistic simulations (molecular dynamics or statics; here collectively referred to as MD) can provide insights into operative deformation mechanisms in alloys, including HEAs, in parallel with DFT simulations. The most powerful use of MD is probably in the testing of mechanistic theories. Atomic simulations provide a precise laboratory in which all material quantities are known/calculated and in which complex interactions of dislocations with other defects can be studied in detail. While simulations are rarely accurate for any real material, due to the limitations of the underlying semi-empirical interatomic potentials typically used, simulated materials may be very suitable model materials for testing the inevitable approximations/assumptions that arise in theory. As long as the interatomic potentials do not have pathologies, i.e. unphysical behaviour, they can be used to test theories. The use of the ternary Cr-Fe-Ni potential for FCC structures by Bonny et al. [52] is an example. For any Cr-Fe-Ni materials, this potential is not quantitative but is not pathological and was thus used in FCC HEAs [53] to test a theory for solvent reinforcement.

## 1.4 Objective of this study

In the current water-cooled nuclear fission reactors, austenitic stainless steels are widely used as structural materials. Future nuclear energy systems require radiation doses up to 100-200 displacements per atoms (dpa), and there are no austenitic stainless steels that are widely used as structural materials in the current water-cooled nuclear fission reactors available for the next generation of nuclear energy systems. Some recent papers have reported the initial examination of the fundamental irradiation behavior in HEAs [6,7], thereby giving insight into the potential of those materials for nuclear applications. Although Co-based HEAs were reported to exhibit excellent mechanical behavior and constitute a good solution for the use in next-generation nuclear energy systems [6,19,54]. Unfortunately, the neutron irradiation leads to activation of Co which becomes radioactive, leading to increase radiation shielding requirements during handling during the reprocessing and the maintenance of such elements [55,56].

In this study, therefore, face-centered cubic Co-free solid solution concentrated alloys were prepared in order to investigate their microstructure, mechanical properties, and irradiation effect at 773K up to 1 dpa as a basic study of the development of HEA applicable to the nuclear environment.

# Chapter 2

---

## Methodology

---

## 2.1 Vacuum melting

Arc melting and induction heating are pretty common methods of producing alloys from components with high melting temperatures. They can be used in small laboratory environments or manufacturing settings on a wide scale. For arc melting, as shown in Figure 2.1, the heating process is through an electrical arc between a tungsten electrode and metals placed in a crucible in a copper core. In the melting of the vacuum arc, the chamber is evacuated and filled back with argon gas. Basic Principle: The regular Tungsten Inert Gas (TIG) welding unit is used as a source of strength. The heat produced by the electric arc between the electrode and the metals is used to melt the metals placed in the crucible to create an alloy. Repeated melting is achieved to increase the homogeneity of the alloy. Since Ar is an inert gas that does not react with molten metal, the evacuation of the chamber prevents the oxidation of the melt. The metals can be heated to a high temperature of more than 3000°C. For induction furnaces, capacity varies from less than one kilogram to one hundred tons and is used for the melting of iron and steel, copper, aluminum, and precious metals. Since no arc or combustion is used, the material's temperature can be controlled. But the lack of refining capacity is the one big downside to the use of an induction furnace in a foundry; charge materials must be clean of oxidation products and proven composition and some alloying elements might be lost due to oxidation.

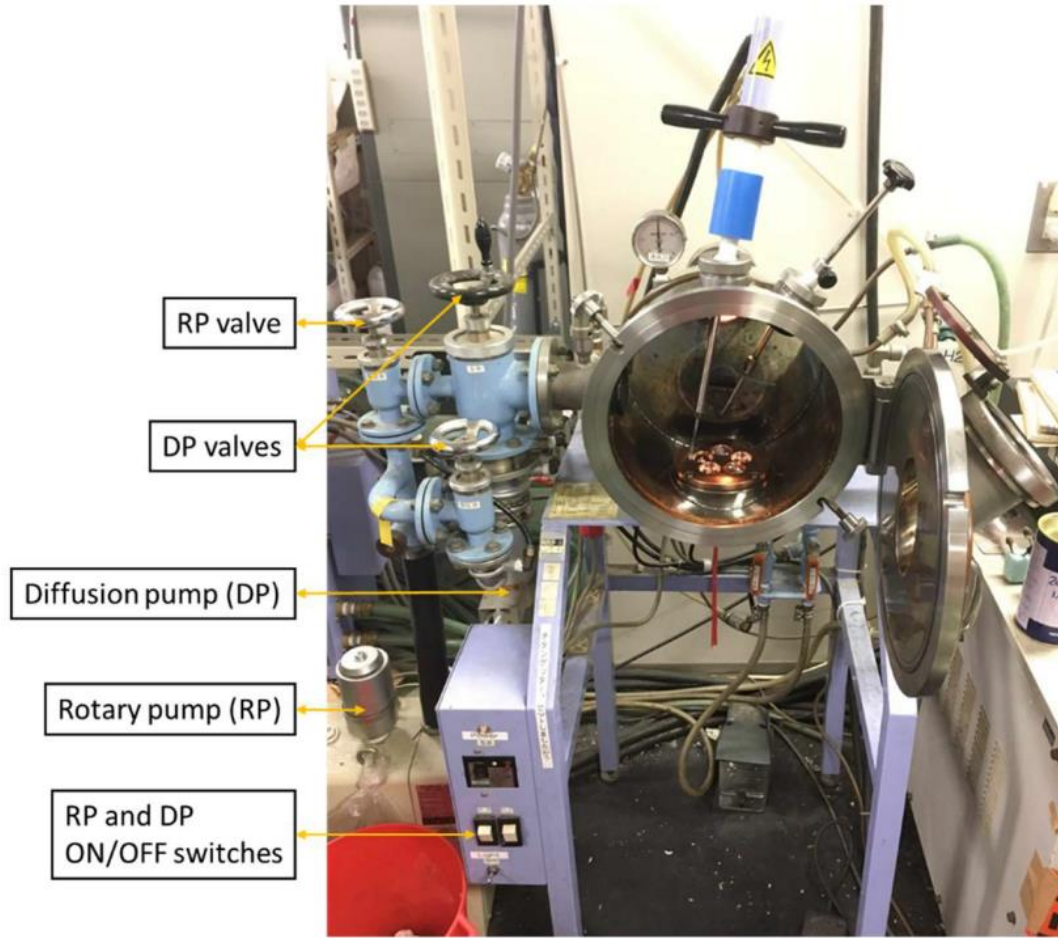


**Figure 2.1 Arc melting furnace with an enclosed crucible**

In this study, pure copper, nickel, iron, chromium, and aluminum (>99.9% purity) were used as raw materials for the fabrication of the face-centered cubic Co-free Cu-containing single-phase concentrated solid-solution alloys. CuNi and CuNiFe alloys were prepared by arc-melting with the buttons flipped and melted more than ten times to ensure well-mixed before drop-casting into a copper mold. Based on previous research [57], non-equimolar composition  $\text{Cu}_{0.3}\text{NiFeCr}$  and  $\text{Al}_{0.4}\text{CuFeCrNi}_2$  were chosen for getting single-phase alloys.  $\text{Cu}_{0.3}\text{NiFeCr}$  and  $\text{Al}_{0.4}\text{CuFeCrNi}_2$  alloys were prepared by induction furnace in a high purity argon atmosphere.

## **2.2 X-ray fluorescence (XRF) spectrometry**

X-ray fluorescence (XRF) spectrometry is a non-destructive analytical technique used to extract elementary information from various types of materials. It is used in many sectors and applications, such as cement manufacturing, glass manufacturing, mining, coal processing, iron, steel, non-ferrous metals, and so on.

In EDXRF spectrometers, the X-ray tube serving as a source directly irradiates the sample and the fluorescence from the sample is determined by an energy dispersion detector. The interaction of the X-ray beam with the sample results in electrons being displaced from the atom's inner orbital shells. Then, given that the atoms tend to fill the lower orbital shells in order to reclaim lower energy, the displaced electrons tend to descend to the lowest orbital layer. Since the area between the orbital shells of an atom is unique to each molecule, the energy lost by the primary X-ray beam during the orbital displacement can be used to classify each element in the sample. The program that includes data on each member of the periodic table is then used to pick the possible elements contained in the sample and to identify the amount of each element using their individual energies.



## 2.3 X-ray diffraction

There are many analytical issues related to the crystalline construction of material samples in materials research. One of laboratory technique that reveals structural information such as chemical composition, crystal structure, crystallite size, strain, preferred orientation, and thickness of the layer is X-ray diffraction (XRD). Therefore, materials researchers use XRD to analyze a broad range of materials from X-ray diffraction (XRPD) powder to solids, thin films, and nanomaterials.

The X-ray diffraction (XRD) enables the microstructure of the sample to be determined. The X-ray wavelength is close to the distance between atoms in a crystal, which is why this procedure is suitable to determine the microstructure of a sample. The scattering of the X-ray from the atoms then produces a diffraction pattern that provides details on the atomic structure within the crystal. Diffraction occurs only when Bragg's Law is a satisfying condition for constructive interference from planes with spacing  $d$ .

$$n\lambda = 2d\sin\theta \quad (2.1)$$

where  $n$  is the order,  $\lambda$  is the wavelength of the incident radiation,  $d$  is the interplanar spacing and  $\theta$  is the reflected angle, see Figure 2.2, interfere constructively and appear as reflections that are detected. Note that this analysis cannot provide information on amorphous structures due to the lack of periodic sequences in the crystalline structure. The interatomic structure shall determine the position of the diffraction peaks, while the atom types and positions shall determine the intensity of the diffraction peaks.

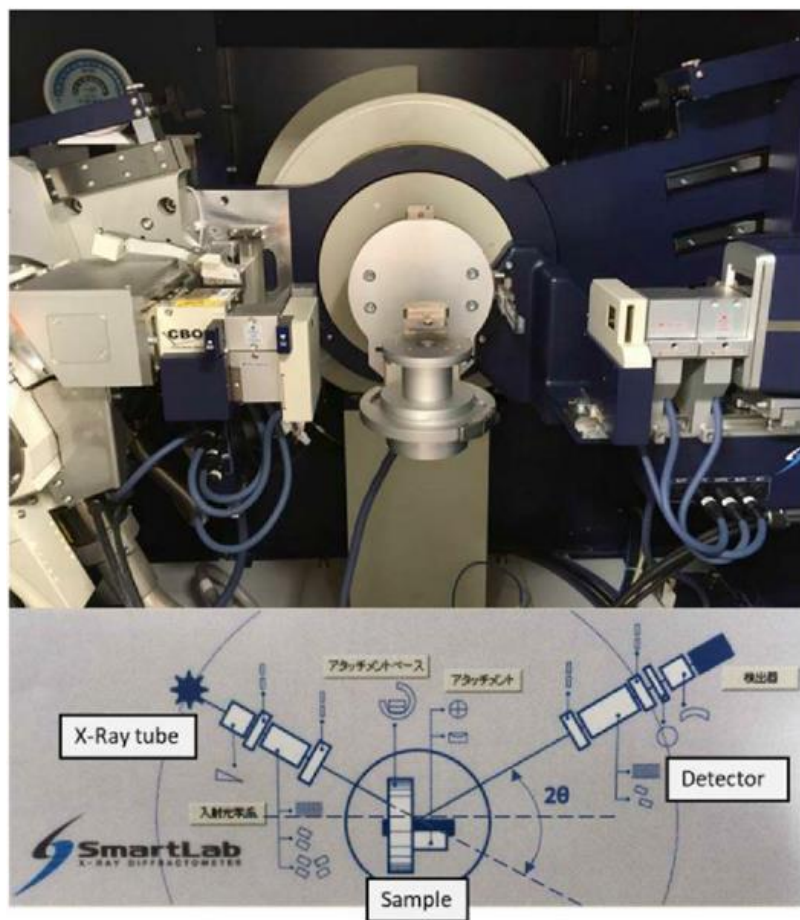
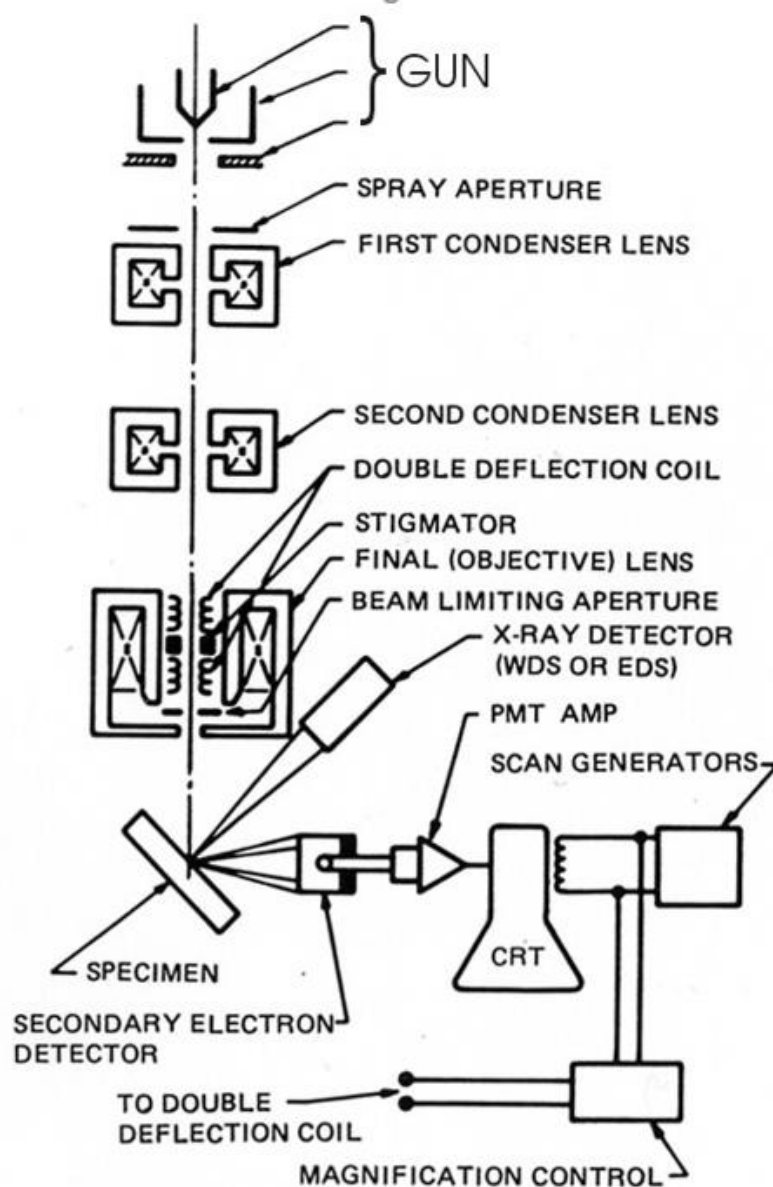


Figure 2.2 X-Ray Diffractometer and standard Bragg-Brentano experimental XRD setup

## **2.4 Scanning electron microscopy**

Another standard laboratory analysis technique that utilizes electrons to test a material's microstructure, surface morphology, and chemical distribution is scanning electron microscopy (SEM). Signals obtained from electron-sample interactions reveal knowledge about the sample, including external morphology, chemical composition, and the crystalline structure and orientation of the sample materials. Owing to the very small electron beam, SEM micrographs have a broad depth of field giving a typical three-dimensional appearance that is useful for understanding the surface structure of the sample[58]. Signals used by the SEM to create a picture are the product of electron beams that encounter atoms at varying depths within the sample. Many types of signals are generated, including secondary electrons (SEs), mirrored or backscattered electrons (BSEs), characteristic X-rays and lights (CLs), absorbed currents (sample currents), and transmitted electrons. And EDS (Energy Dispersive Spectroscopy) could be run with the SEM used in the laboratory. SEI images are obtained by the program to do this analysis. EDS methodology uses an analysis of pulse height: a detector providing output pulses equal to the X-ray photon energy is used in combination with an analysis of pulse height. Incident X-ray photons induce ionization in a solid-state detector, creating an electrical charge that is intensified by a sensitive preamplifier placed above a solid-state detector.



**Figure 2.3** Schematic drawing of the electron and x-ray optics of a combined SEM-EPMA as searched in Web of Geochemical Instrumentation and Analysis

For bulk Cu-containing samples, the JSM-6510LA scanning electron microscope (SEM) operating at 15 kV and fitted with the Norman Voyager Series IV energy-dispersive spectroscopy system (EDS, Thermo Electron Corporation) was used for microstructural and phase-composition research.

## 2.5 Transmission electron microscopy

Transmission electron microscopy is a microscopy technique in which the electron beam is transmitted through a specimen to create an image. Very commonly, the specimen is an ultra-thin segment less than 80 nm thick, which means the sample preparation is difficult and time-consuming. Comparing with SEM, which can only provide details on the morphology of the specimen. TEM can inform us about a substance's structure, crystallization, morphology, and stress.

An electron gun releases a beam of electrons inside a transmission electron microscope. Using electric coils and voltages of up to several million volts, the gun accelerates the electrons to incredibly high velocities. The electrons zoom through the ultra-thin specimen until achieving their highest intensity, and portions of the beam are distributed based on how translucent the sample is to electrons. The objective lens focuses on the component of the beam emitted into an image from the sample. The image (micrograph) created by TEM is visualized by projection on a phosphorescent screen. This screen emits photons when irradiated by an electron beam. A film camera located below the screen can be used to record an image or a digital capture can be accomplished using a charge-coupled (CCD) camera.

One of the simplest optical microscopies is Bright-field (BF) microscopy. The illumination light is transmitted through the sample in bright-field microscopy, and the contrast is provided by light absorption in dense areas of the specimen. Due to the distorted nature of out-of-focus material, the restrictions of bright-field microscopy include poor contrast for weakly absorbed samples and low resolution. Dark-field (DF) Illumination usually results in a light field or background image. The dark-field condensing device uses a central circular disk stop that stops direct condenser rays from penetrating the objective prism. Just those rays that have been

adequately dispersed in an object join the objective lens to produce the final image. The detail of the source responsible for the scattering appears light against a dark backdrop or area. In transmitting mode, this lighting system finds valuable applications in the study of low-contrast materials — but which diffuse light — such as small particles or internal inclusions and pores in thin parts. Incident dark-field lighting will also offer better image contrast over bright-field approaches for objects with topographical anomalies [59]. The concept 'weak-beam microscopy' applies to the development of a diffraction-contrast image in either BF or DF where weakly excited beams offer useful information. Historically, the technique of weak-beam dark-field (WBDF) is important because dislocations can be imaged as thin lines that are approximately 1.5 nm wide under some special diffraction conditions. The fact that the positions of these lines are well established with regard to the dislocation cores is almost equally important; they are also reasonably indifferent to both the thickness of the foil and the direction of the dislocations in the specimen [60]. The technique is particularly helpful for researching dislocations.

Within this dissertation, ex-situ TEM images and diffraction patterns were obtained using a JEOL 2010F operated at 200 kV. The grains were monitored via bright-field images, weak-beam dark-field images, and selected area electron diffraction patterns.

## 2.6 Ion irradiation

In general, ion irradiation involves using particle accelerators to fire energetic ions through a substance. As fast heavy ion irradiation from particle accelerators causes ion tracks that can be used for nanotechnology.

In this study, CuNi, Cu<sub>0.3</sub>NiFeCr and Al<sub>0.4</sub>CuFeCrNi<sub>2</sub> alloys were used for the preparation of TEM specimens and irradiated with 1 MeV krypton ions at 500 ° C to a fluence of  $6.3 \times 10^{14}$  ions·cm<sup>-2</sup> within the Hitachi-9000 TEM in the Intermediate-Voltage Electron Microscopy (IVEM)-Tandem facility at the Argonne National Laboratory. The IVEM-Tandem facility, see Figure 2.4, is a unique facility used for in situ TEM studies of defect structures in materials under controlled ion irradiation and sampling conditions, capable of imagining changes in the atomic structure and the creation of defects during irradiation at high magnification. The main benefits of IVEM include real-time observation of defect formation and evolution during irradiation. Well-controlled experimental conditions (constant orientation and area of the specimen, the temperature of the specimen, ion form, ion energy, dose rate, dose, and applied strain). Refine and verify the simulation of the radiation defect condition of the computer model. High-dose ion exposure results in hours, rather than years, and may enable some damage in a nuclear reactor to support studies of material reaction to high doses of particle (ion and neutron) irradiation. In situ ion irradiation shall not contain any radioactivity in the samples.



**Figure 2.4** Intermediate Voltage Electron Microscopy-Tandem as searched in Web of Argonne national laboratory

In the irradiation tests, the ion flux was around  $1.3 \times 10^{12} \text{ ions} \cdot \text{cm}^{-2} \cdot \text{s}^{-1}$ . At 300 kV, the microscope worked. With the Stopping and Range of Ions in Matter (SRIM) with the fast Kinchin-Pease option [18] for each material, the profile of irradiation damage was determined as shown in Fig. 1. The displacement dose was used on the SRIM profile at 100 nm below the irradiation surface as the nominal dose for each irradiation experiment.



## 2.7 Density Functional Theory Calculation

As mentioned in Chapter 1.3.4, DFT includes different simulation approaches within which GPAW [51] would be used in this research. In the DFT process, the energy of the models is determined by the functions of the electrons. However, cost efficiency is relatively low to solve all the functions of the electrons. Thus, the PAW process, which measures small electrons but still provides useful results, is frequently used. GPAW is a subset of PAW that divides the crystal lattice of the atom models in the calculation process. GPAW requires some math Libraries like Basic Linear Algebra Subprograms (BLAS) and Linear Algebra Package (LAPACK) and some modules like Atomic Simulation Environment (ASE).

BLAS and LAPACK are the basic math Libraries for vector scaling, matrix multiplications and numerical linear algebra. Those math Libraries are essential for commonly used DFT softwares including VASP. Intel Math Kernel Library (MKL) is a library of optimized math routines, its core math functions include BLAS, LAPACK, ScaLAPACK, sparse solvers, fast Fourier transforms, and vector math. The routines in MKL are hand-optimized specifically for Intel processors. So, compared with the basic BLAS and LAPACK Libraries, MKL can provide high performance in general. Therefore, GPAW was compiled with MKL to achieve high calculation efficiency.

## Chapter 3

---

# Microstructure and mechanical properties in Cu-containing high entropy alloys

---

### 3.1 Introduction

In recent years, high entropy alloys (HEAs) has been attracting attention as a unique material. Some HEAs have single-phase crystal structures due to the increase in the configurational entropy [61-68]. The entropy-based definition characterizes the HEA by the maximum entropy possible and implies that such a state is achieved at high temperatures or in the liquid state [69]. During the last decade, many types of research have been carried out in understanding the criteria governing the formation of a simple solid solution with multiple components. Takeuchi et al. [70] suggested that the formation of simple solid solution phases was promoted if the enthalpy of mixing ( $\Delta H_{\text{mix}}$ ) was in the range of 7–22 kJ/mol and an atomic size difference factor ( $\delta$ ) was less than 8.5%. Furthermore, it has been reported that several HEAs have good mechanical properties from cryogenic temperatures to high temperatures [71-75]. Based on those researches, some HEAs can be suggested as a structural material and as coatings [76-78]. George et al. [79] have summarized the research on HEAs.

In the current water-cooled nuclear fission reactors, austenitic stainless steels are widely used as structural materials. High-performance steels are considered to be essential for numerous proposed nuclear energy systems that require radiation doses up to 100-200 displacements per atoms (dpa). Currently, there is no high radiation resistance austenitic stainless steels available for extended operations at elevated temperatures for the next generation of nuclear energy systems. One of the candidate materials for next-generation nuclear reactor components could be FCC type HEAs.

Considering a candidate HEA for nuclear application, the radioactive elements should be eliminated from the material design based on radiation shielding requirements during handling and the maintenance of components. Copper alloy, Cu-Cr-Zr alloy having constituents in the

range of 0.6 - 0.8 % in Cr, 0.07 - 0.15 % in Zr, due to its excellent thermal conductivity, mechanical properties, resistance to corrosion, creep resistance, and radiation resistance, is used as a component for the candidate International Thermonuclear Experimental Reactor (ITER) [80]. Therefore, copper was chosen as one of the fundamental elements for preparing solid solution concentrated alloys. In this chapter, face-centered cubic Co-free Cu-containing solid solution concentrated alloys were prepared in order to investigate their microstructure, mechanical properties as a basic study of the development of HEA applicable to the nuclear environment.

### **3.2 Fabrication of single-phase face-centered cubic Co-free Cu-containing alloys.**

The first step that was taken in this research was to prepare face-centered cubic Co-free Cu-containing single-phase concentrated solid-solution alloys. Thus, pure copper, nickel, iron, chromium, and aluminum (>99.9% purity) were used as raw materials for the fabrication of the Cu-containing concentrated solid-solution alloys.

Based on phase diagrams which reflect the relationship between the temperature and the composition of phases present at equilibrium, see Figure 3.1 and Figure 3.2, CuNi and CuNiFe alloys of the equal molar ratio were prepared by arc-melting with the buttons flipped and melted more than ten times to ensure well-mixed before drop-casting into a copper mold. Figure 3.1 shows the Cu-Ni diagram [81], which is an isomorphous alloy system. In that system, the two elements have unlimited solubility, which means that they are like water and alcohol as they mix-they still form a solid solution independent of the ratio of atoms to molecules. Figure 3.2 shows the ternary phase diagram Cu-Fe-Ni at 1273 K [82], which also provides the possibility of forming single-phase alloys with equal atomic Cu, Ni, and Fe at about 1000°C.

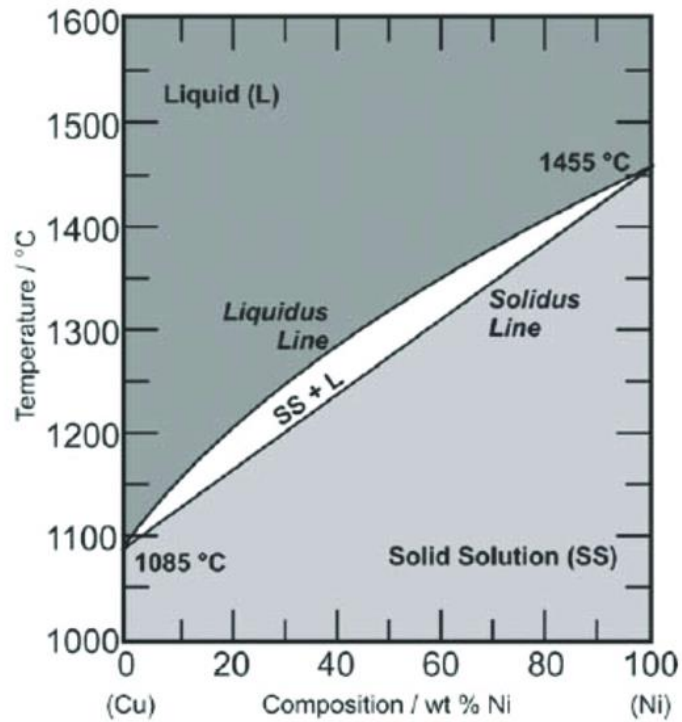


Figure 3.1 Cu-Ni phase diagram [79].

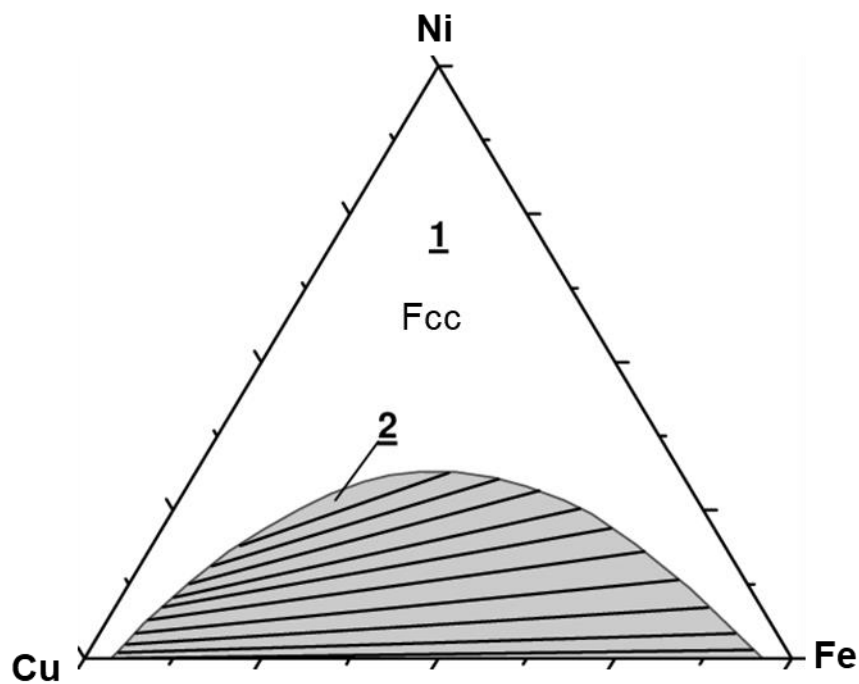
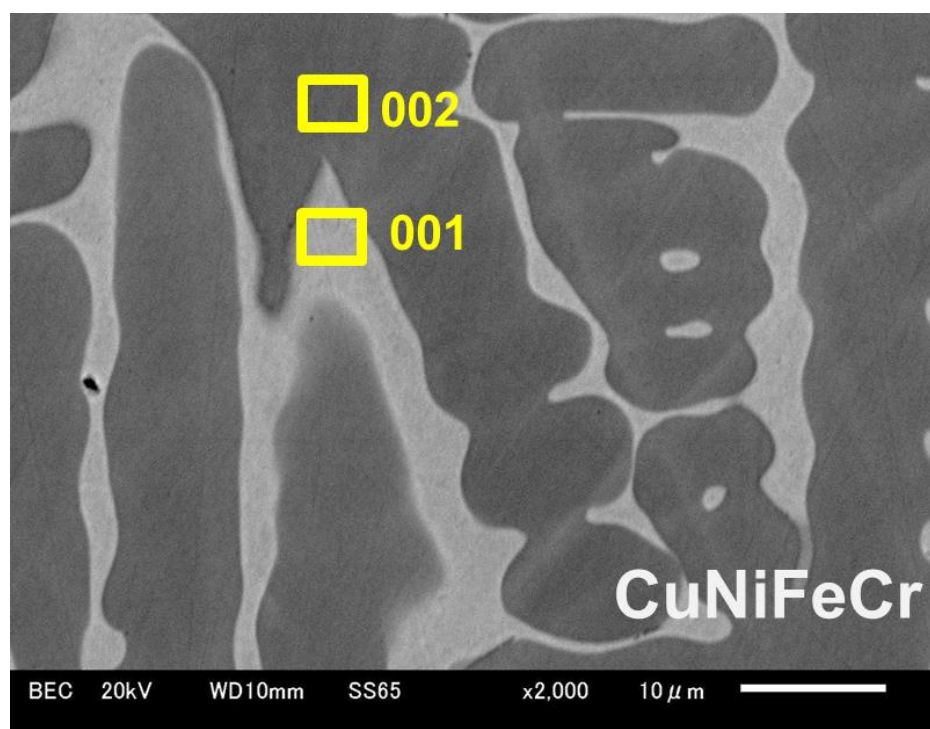


Figure 3.2 Ternary phase diagram Cu-Fe-Ni at 1273 K: 1 – single-phase alloy, 2 – two-phase alloy. The miscibility gap based on experimental results and thermodynamic reassessment [80]

For quaternary alloy, the initially prepared equimolar ratio alloy showed obvious two phases under the scanning electron microscope (SEM) observation, see Figure 3.3. The 001 region was an obvious copper-rich phase region, see Table 3.1. In order to obtain a single-phase quaternary alloy, the non-equimolar composition  $\text{Cu}_{0.3}\text{NiFeCr}$  of the 002 region was selected to prepare the quaternary alloy.



**Figure 3.3** Typical SEM-BEC images of as-cast CuNiFeCr

**Table 3.1** EDS analysis of as-cast CuNiFeCr focused on areas [001] and [0072]

Component (at%)	Cu	Ni	Fe	Cr	Total
001	78.92	8.64	6.18	6.20	100.00
002	11.27	28.03	30.02	30.68	100.00

For high entropy alloy, based on previous research [57], a series of Co-free  $\text{Al}_x\text{CrCuFeNi}_2$  high entropy alloys were developed, and their microstructures were observed. The XRD patterns for

the  $\text{Al}_x\text{CrCuFeNi}_2$  alloys as shown in Figure 3.4. Only fcc-typed solid solutions have been observed at  $x \leq 0.7$ . Bcc solid solutions began to be detected at  $x = 0.8$  and the quantity of fcc solid solutions declined with Al increasing [57]. Thus, the non-equimolar composition  $\text{Al}_{0.4}\text{CuFeCrNi}_2$  was chosen for getting a single-phase high-entropy alloy.  $\text{Cu}_{0.3}\text{NiFeCr}$  and  $\text{Al}_{0.4}\text{CuFeCrNi}_2$  alloys were prepared by induction furnace in a high purity argon atmosphere.

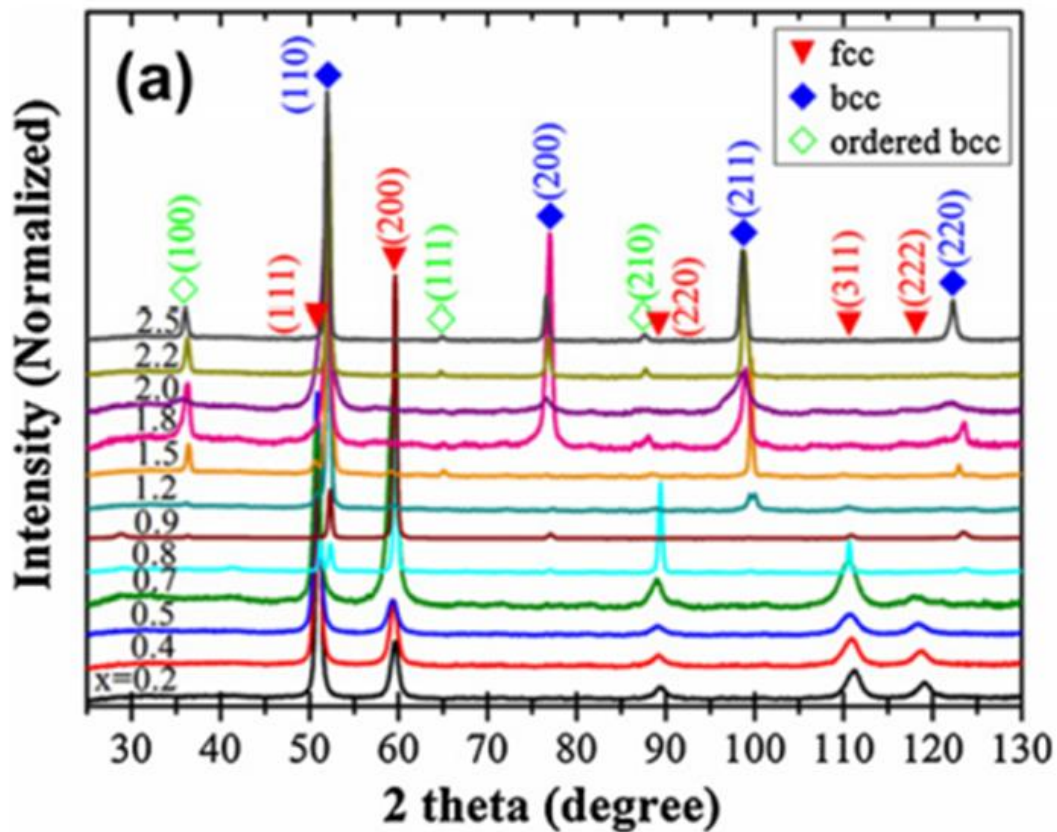


**Figure 3.4** XRD patterns for the as-cast  $\text{Al}_x\text{CrCuFeNi}_2$  alloys [57].

The chemical compositions of the five alloys which were identified by ED-XRF (Energy Dispersive X-Ray Fluorescence) spectrometer are listed in Table 3.2. Based on phase diagrams and previous research [57], all ingots were solution-annealed in order to obtain homogeneity. The solution annealing conditions of the five alloys are listed in Table 3.3. For  $\text{CuNi}$ ,  $\text{CuNiFe}$ ,  $\text{Cu}_{0.3}\text{NiFeCr}$  and  $\text{Al}_{0.4}\text{CuFeCrNi}_2$  alloys,  $S^{\text{SS,ideal}}$  is equal to 0.69R, 1.10R, 1.30R and 1.50R,



respectively. Based on the definition of high-entropy alloys in Section 1.3.1, here we define  $\text{Al}_{0.4}\text{CuFeCrNi}_2$  alloy as a high-entropy alloy.

**Table 3.2 The nominal chemical composition (at%) of Co-free Cu-containing alloys**

Alloys	Cu	Ni	Fe	Cr	Al	C	N
Cu	99.99	-	-	-	-	0.004	0.0002
CuNi	49.9	49.9	-	-	-	0.007	0.0008
CuNiFe	33.3	33.3	33.3	-	-	0.013	0.0004
$\text{Cu}_{0.3}\text{NiFeCr}$	9.9	29.9	29.9	29.9	-	0.005	0.0007
$\text{Al}_{0.4}\text{CuFeCrNi}_2$	18.4	37	18.4	18.4	7.4	0.011	0.0004

**Table 3.3 Solution annealing conditions of Co-free Cu-containing alloys**

	Solution annealing condition
Cu	600 °C/ 2 h
CuNi	1000 °C/24 h
CuNiFe	1050 °C/24 h
$\text{Cu}_{0.3}\text{NiFeCr}$	1076 °C/120 h
$\text{Al}_{0.4}\text{CuFeCrNi}_2$	1000 °C/24 h

### 3.3 Microstructure analysis

The microstructure of the alloys was observed by scanning electron microscope (SEM, JSM-6510LA) equipped with an energy dispersive spectrometer (EDS) with an accelerating voltage of 15 kV. The crystal structure of the as-cast and annealed specimens was identified by X-ray diffraction (SmartLab XRD) at a speed of 6°/min with Cu K $\alpha$ 1 radiation.

The phases in the Cu-containing alloys were firstly determined by using XRD. Figure 3.5 shows the diffraction peaks of CuNi, CuFeNi, Cu<sub>0.3</sub>NiFeCr, and Al<sub>0.4</sub>CuFeCrNi<sub>2</sub>. The diffraction peaks of both as-cast and solution-annealed CuNi matched with a single-phase FCC CuNi. While, the diffraction peaks of both as-cast and solution-annealed CuFeNi, Cu<sub>0.3</sub>NiFeCr and Al<sub>0.4</sub>CuFeCrNi<sub>2</sub> matched with a single-phase FCC Cu. Therefore, all the prepared Co-free Cu-containing alloys would have face-centered cubic structures. The BEC image and the EDS mapping image of CuNi, CuFeNi, and Al<sub>0.4</sub>CuFeCrNi<sub>2</sub> showed no contrast and homogeneity, respectively. Figure 3.6 and Figure 3.7 shows the typical SEM-BEC (Backscattered Electron Composition) images and the EDS mapping of solution-annealed Al<sub>0.4</sub>CuFeCrNi<sub>2</sub>.

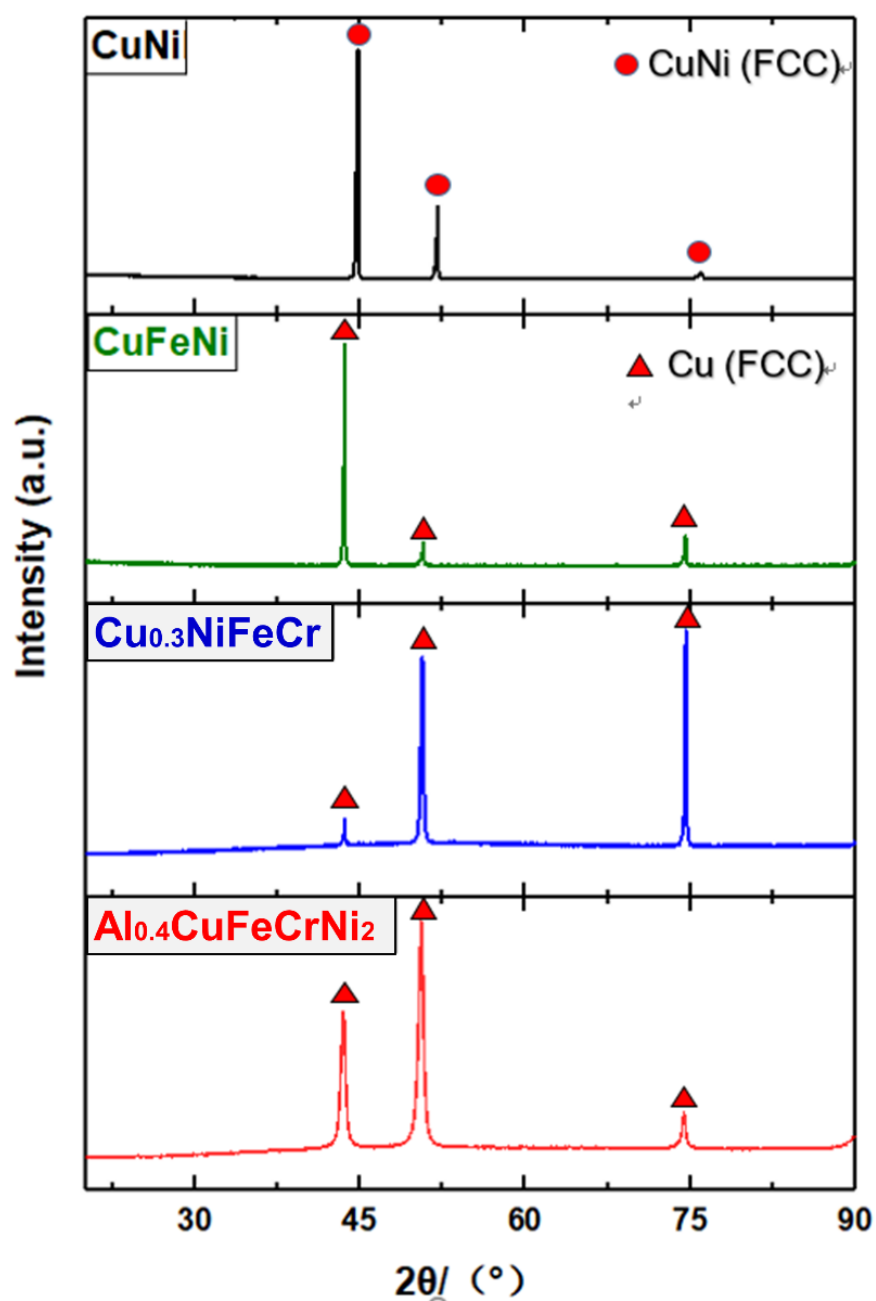


Figure 3.5 XRD patterns for the Co-free Cu-containing solid solution concentrated alloys

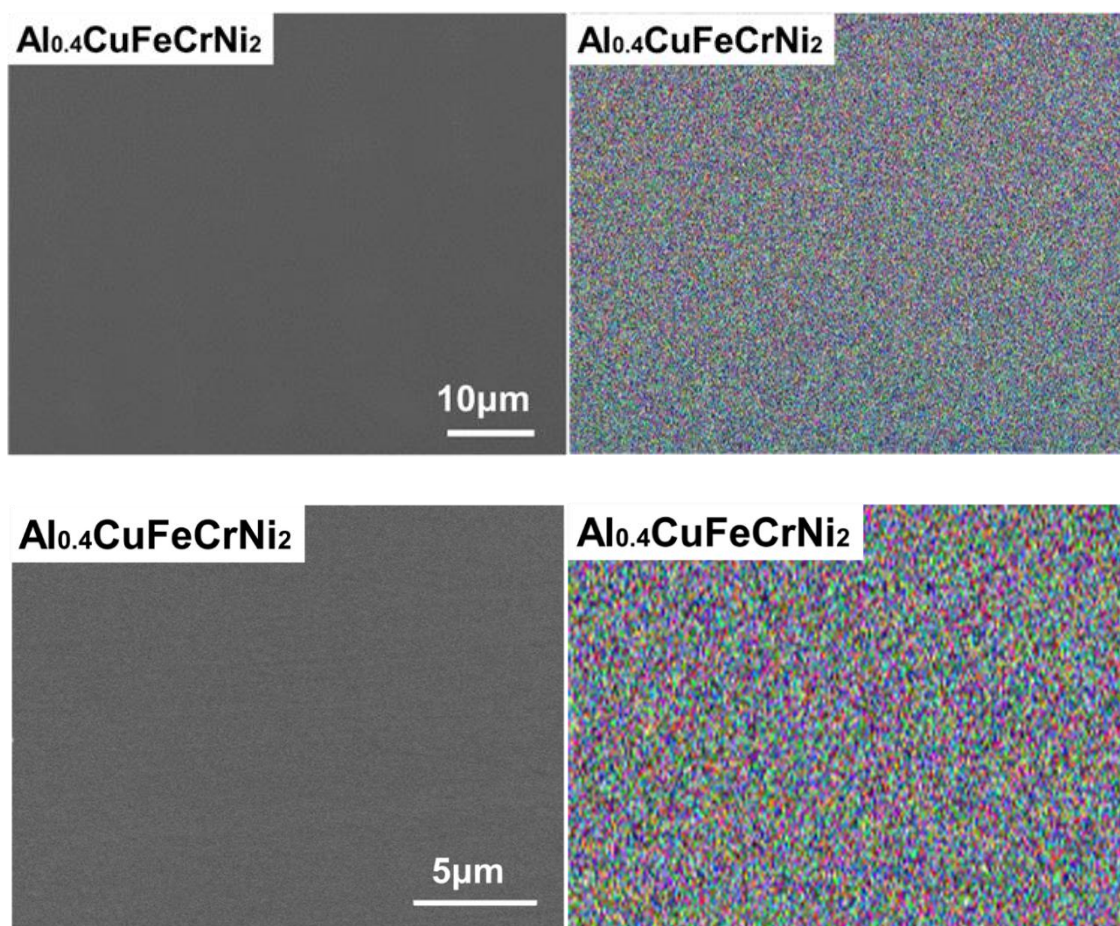
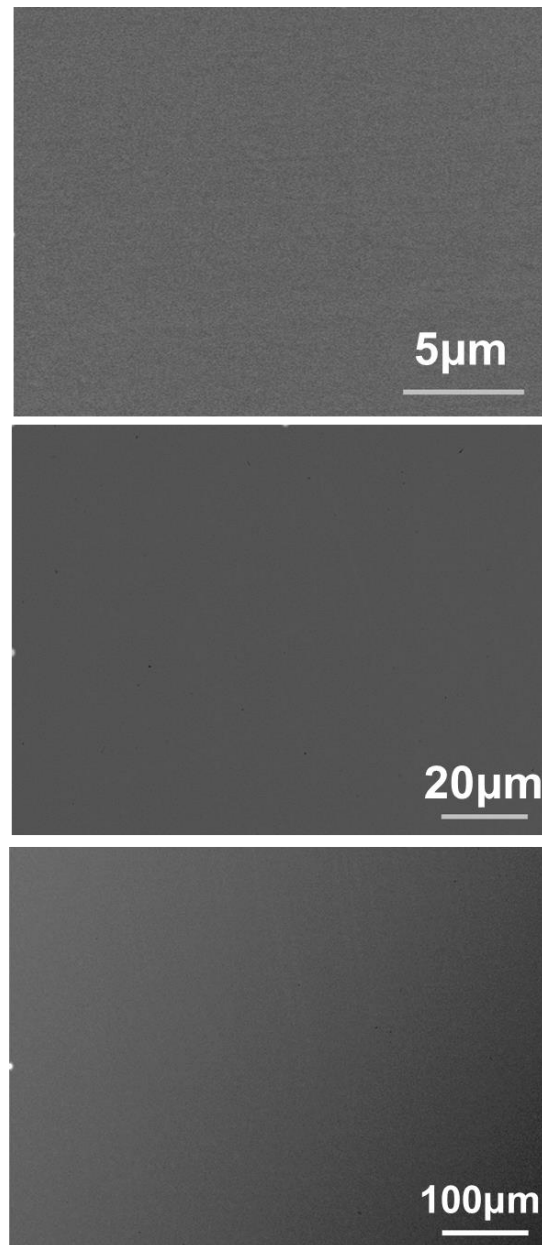


Figure 3.6 Typical SEM-BEC images and EDS Mapping images of solution annealed  $\text{Al}_{0.4}\text{CuFeCrNi}_2$



**Figure 3.7** Typical SEM-BEC images of Al<sub>0.4</sub>CuFeCrNi<sub>2</sub> at different magnifications (X5000, X1000, and X200)

On the other hand, the SEM-BEC image of as-cast Cu<sub>0.3</sub>NiFeCr alloy showed inhomogeneously. Figure 3.7 shows the SEM-BEC images and the EDS mapping images of as-cast and 1000 °C/24h annealed Cu<sub>0.3</sub>NiFeCr alloy. The as-cast Cu<sub>0.3</sub>NiFeCr alloy included the Cu-rich phase shown in light gray contrast in the SEM-BEC image and red color in the EDS mapping (Figure 3.8a). As mentioned above, the diffraction peaks of Cu<sub>0.3</sub>NiFeCr alloy matched with a

single-phase FCC Cu, meaning that the matrix and Cu-rich phase were not distinguished by XRD. Figure 3.8b shows the microstructure of  $\text{Cu}_{0.3}\text{NiFeCr}$  alloy annealed at 1000 °C for 24 hours. During annealing, a new Cr-rich phase (dark contrast) formed on the Cu-rich (light gray contrast) phase as shown in the EDS mapping. This phenomenon was caused probably due to the low solubility of copper and chromium. Based on the Cu-Cr phase diagram, the eutectic temperature (1076 °C) was chosen as the annealing temperature of  $\text{Cu}_{0.3}\text{NiFeCr}$ . Figure 3.9(a)-(d) shows the SEM-BEC images of  $\text{Cu}_{0.3}\text{NiFeCr}$  annealed at 1076 °C for 24, 48, 72 and 120 hours. In the as-cast  $\text{Cu}_{0.3}\text{NiFeCr}$ , the Cu-rich phase existed in the matrix as a dendritic structure (Fig 3.9a). The dendritic Cu-rich phase seemed to be decomposed after annealing at 1076 °C for 24 hours (Fig 3.9b). Furthermore, the Cu-rich phase enriched at the grain boundaries after annealing for 48 hours (Fig 3.9c) and disappeared after 120 hours (Fig 3.9d). Finally, a single-phase FCC structure of  $\text{Cu}_{0.3}\text{NiFeCr}$  alloy was obtained after annealing at 1076 °C for 120 hours.

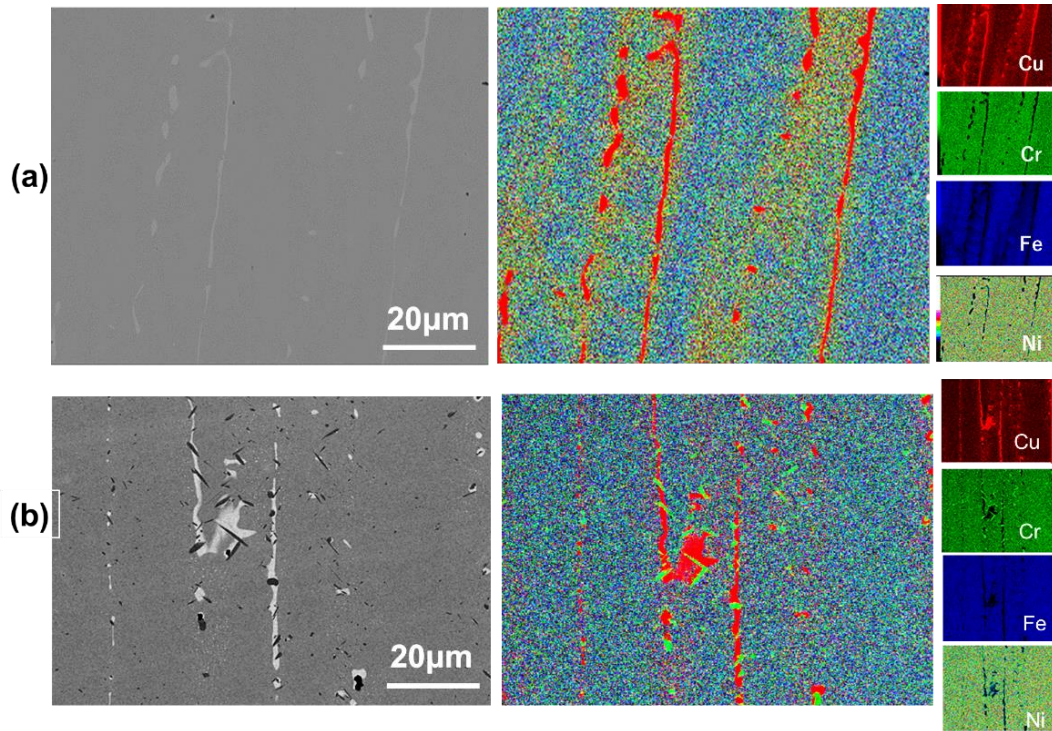


**Figure 3.8** Typical SEM BEC images and the EDS Mapping of (a) as-cast and (b) 1000 °C/24h annealed  $\text{Cu}_{0.3}\text{NiFeCr}$  alloy.

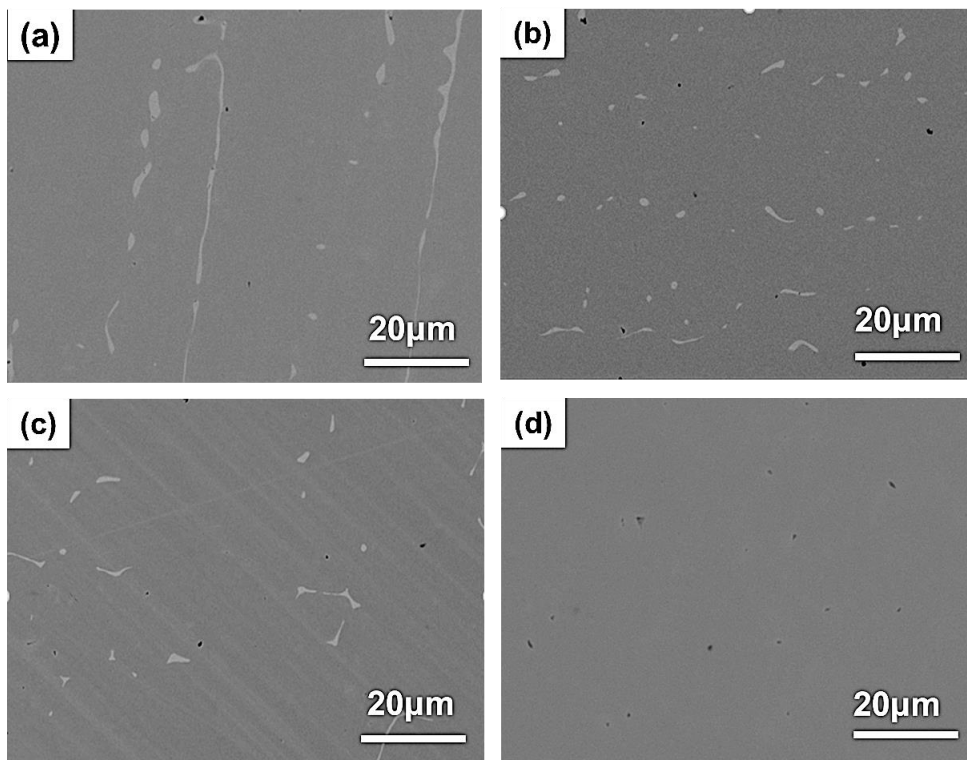


**Figure 3.9** Typical SEM-BEC images of  $\text{Cu}_{0.3}\text{NiFeCr}$  annealed at 1076°C for (a) 24, (b) 48, (c) 72 and (d) 120 hours.



### 3.4 Vickers hardness

The hardness of the samples was measured using Vickers indenter (Struers) at room temperature under a load of 1 kg with a dwell time of 15 s. Figure 3.10 shows the Vickers hardness of the as-cast and the solution-annealed alloys. The Vickers hardness of annealed alloys was similar to that of as-cast alloys. While the hardness seemed to increase with increasing the number of elements. This would be due to the general solid solution hardening effect. It should be noted that the hardness of  $\text{Al}_{0.4}\text{CuFeCrNi}_2$  exhibited much higher (204 HV) compared to that of CuCrZr alloy (68-93 HV), which would be used for the high heat flux components of the International Thermonuclear Experimental Reactor (ITER)[80].

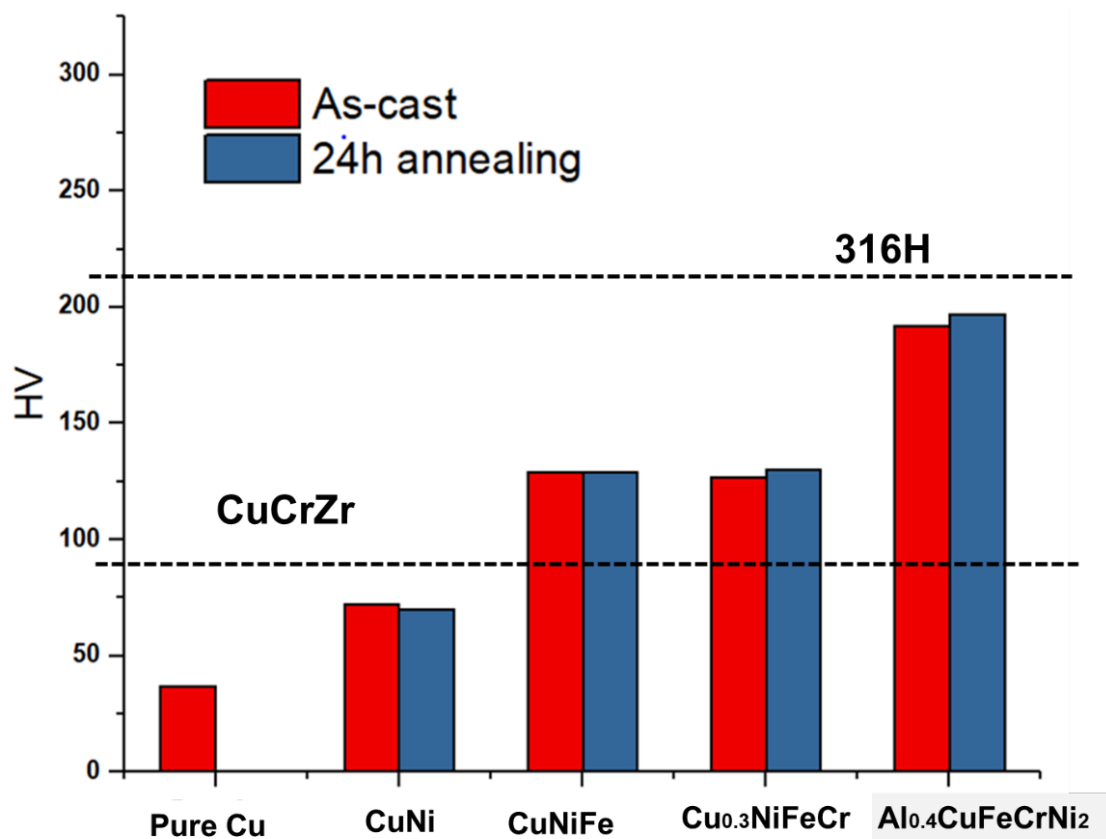


Figure 3.10 Vickers Hardness of all the alloys of as-cast and solution-annealed for 24 hours.



### 3.5 Tensile strength

Tensile tests were performed out for SSJ-type small tensile samples (the gauge section dimension of 0.25 x 1 x 5 mm) at a strain rate of  $10^{-3} \text{ s}^{-1}$  with an INSTRON 5564 tensile tester at room temperature. While these yield points could obviously not be obtained, the tensile yield strengths were read at a 0.2 percent strain offset. Three or more tests were conducted out for each alloy.

Figure 3.11 shows the stress-strain curves of all the solution-annealed alloys, 316H steel and CuCrZr alloy as a comparison. The values of ultimate strength, yield strength ( $\sigma_{0.2}$ ) and elongation of all the alloys at room temperature are listed in Table 3.4. The results showed the increase in strength with increasing the number of elements probably due to the solid solution strengthening effect. The  $\text{Al}_{0.4}\text{CuFeCrNi}_2$  exhibited the highest strength and the smallest elongation. Comparing with the tensile property of 316H steel and CuCrZr alloy, the  $\text{Al}_{0.4}\text{CuFeCrNi}_2$  showed higher strength and lower elongation. Besides, the elongation of  $\text{Al}_{0.4}\text{CuFeCrNi}_2$  was almost similar to that of CuNiFe and  $\text{Cu}_{0.3}\text{NiFeCr}$  alloy, suggesting that the  $\text{Al}_{0.4}\text{CuFeCrNi}_2$  would have a higher ductility than CuNiFe and  $\text{Cu}_{0.3}\text{NiFeCr}$  alloy. In order to improve the ultimate elongation of  $\text{Al}_{0.4}\text{CuFeCrNi}_2$ , a detailed analysis of the fracture surface and the optimization of the annealing condition would be needed. It has been known that the catastrophic fracture mechanism occurs in three stages: 1) nucleation, 2) growth, and 3) coalescence of voids [83]. Generally, under the same fracture conditions, the larger the dimple size, the lower the plasticity of the material. And, the solution treatment and aging affect the dimple size, thereby changing the type of failure [84]. Therefore, analysis of the effect of different solution treatment temperature and aging time on the plasticity of samples would be needed.

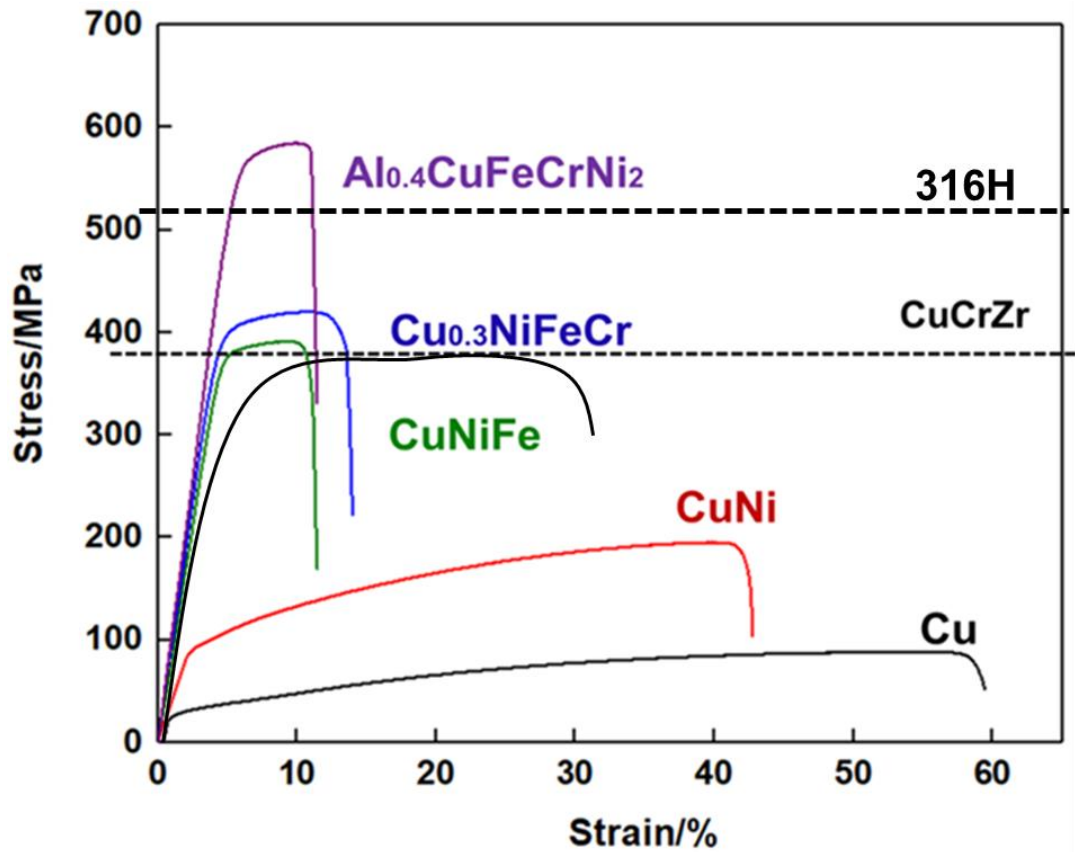


Figure 3.11 Stress-strain curves of all the solution-annealed alloys, 316H, and CuCrZr as a comparison.

Table 3.4 The values of ultimate strength, yield strength ( $\sigma_{0.2}$ ) and elongation of the alloys

	Ultimate Strength (MPa)	Yield Strength ( $\sigma_{0.2}$ )	Elongation (%)
Cu	88.4	42.8	59.50
CuNi	195.5	86.5	42.75
CuNiFe	391.6	359.5	11.45
Cu <sub>0.3</sub> NiFeCr	420.2	381.6	14.01
Al <sub>0.4</sub> CuFeCrNi <sub>2</sub>	612.23	553.5	11.45
CuCrZr [1]	380	240	29
316H [2]	515	205	40

### 3.6 Summary

In this Chapter, the Co-free Cu-containing solid solution concentrated alloys, Cu, CuNi, CuNiFe, Cu<sub>0.3</sub>NiFeCr, Al<sub>0.4</sub>CuFeCrNi<sub>2</sub> were investigated in order to find a proper high entropy alloy for nuclear reactor application. Solution-annealed CuNi, CuFeNi, and Al<sub>0.4</sub>CuFeCrNi<sub>2</sub> showed single-phase FCC structures with the homogeneous atomic distribution. Solution-annealed Cu<sub>0.3</sub>NiFeCr alloy included the dendritic Cu-rich phase in matrix, however, a single-phase FCC structure of Cu<sub>0.3</sub>NiFeCr alloy was finally obtained after annealing at 1076 °C for 120 hours due to the decomposition of the Cu-rich phase. Mechanical property examinations revealed that the order of the Vickers hardness and the Tensile strength was Cu < CuNi < CuNiFe < Cu<sub>0.3</sub>NiFeCr < Al<sub>0.4</sub>CuFeCrNi<sub>2</sub>. The results indicate that the Al<sub>0.4</sub>CuFeCrNi<sub>2</sub> alloy would have the potential to be a Co-free high-entropy alloy applicable to nuclear reactor components. Further experiments on the irradiation resistance properties, such as ion and electron beam irradiation, of these alloys would be needed.

## Chapter 4

---

### Irradiation effects at 500°C in Cu- containing HEAs

---

## 4.1 Introduction

Random solid solutions in lead HEAs exhibit excellent properties, such as high thermal stability, high mechanical properties and great corrosion resistance [71-75,85]. Also, it reported that the high-level lattice distortions due to the atomic size of the elements and compositional complexities in HEAs can reduce the mean free path of electrons, phonon and magnons, thereby modifying defect generation and interaction of irradiation [86,87]. Future nuclear energy systems require radiation doses up to 100-200 displacements per atoms (dpa), and there are no austenitic stainless steels that are widely used as structural materials in the current water-cooled nuclear fission reactors available for the next generation of nuclear energy systems. Therefore, FCC type HEAs could be one of the candidate materials for next-generation nuclear reactor components. Co-based HEAs were reported to exhibit excellent mechanical behavior and constitute a good solution for the use in next-generation nuclear energy systems [6,7,19]. The past studies on in-situ 1 MeV krypton ion irradiation up to 1 dpa found that the evolution of the loop and the resulting hardening were comparative for two HEAs ( $\text{Al}_{0.3}\text{CoCrFeNi}$  and  $\text{CoCrFeMnNi}$ ) and 316H SS at 300 °C [88]. As the temperature is a strong function of the diffusion and effect of configurational entropy, the defect evolution in HEAs is expected to differ at high temperatures. At temperatures above 300°C, the advantage of alloying complexity that affects the defect evolution may be more efficient. The nanoindentation results, the study by Wei-Ying Chen et al. [46], show that the irradiation hardening at 500 °C was lower in the two HEAs ( $\text{Al}_{0.3}\text{CoCrFeNi}$  and  $\text{CoCrFeMnNi}$ ) than in the 316H SS, consistent with the loop density observation. Their study result is a reasonable prediction for HEA applications in high-temperature (500 °C) nuclear reactors.

To understand the irradiation effects and analyze the impact of the compositional complexity in Co-free high entropy alloys at high temperature. High purity face-centered cubic Co-free Cu-

containing solid solution concentrated alloys, CuNi, Cu<sub>0.3</sub>NiFeCr, Al<sub>0.4</sub>CuFeCrNi<sub>2</sub> without apparent preexisting defect sinks were performed in-situ ion irradiation experiments with 1 MeV Kr ion irradiation at 500°C up to 1 dpa. The irradiated microstructures of HEA (Al<sub>0.4</sub>CuFeCrNi<sub>2</sub>) were compared with that of CuNi and Cu<sub>0.3</sub>NiFeCr to assess their irradiation response at 500°C. The irradiation-induced microstructure has been investigated using transmission electron microscopy. The irradiation effects were assessed through the measurement of the defect type, defect density and defect size. Orowan equation was applied to estimate the irradiation hardening contributed by SFTs, black dots and loops. The lowest estimated irradiation hardening in high entropy alloy (Al<sub>0.4</sub>CuFeCrNi<sub>2</sub>) indicated the potential for the nuclear application of Co-free high-entropy alloy at 500°C.

## 4.2 Kr ions irradiation experiment

CuNi, Cu<sub>0.3</sub>NiFeCr, and Al<sub>0.4</sub>CuFeCrNi<sub>2</sub> were included in this study. All of these alloys have a single-phase face-centered cubic (fcc) crystal structure, and these alloys have been investigated for their microstructural and mechanical properties [89]. CuNi alloy was prepared by arc-melting with the buttons flipped and melted more than ten times to ensure good mixing before drop-casting into a copper mold. Cu<sub>0.3</sub>NiFeCr and Al<sub>0.4</sub>CuFeCrNi<sub>2</sub> alloys were prepared by induction furnace in a high-purity argon atmosphere. Table 4.1 shows the chemical compositions of the three alloys. Thick disks of the alloys were cold-rolled down to 150  $\mu\text{m}$ , and 3 mm-diameter disks were punched out from these foils. All these disks were annealed at 800 °C for 24 hours to remove strain field caused by cold rolling, followed by electropolishing (Table 4.2) using a Tenupol-5 jet polisher with an electrolyte of 5% perchloric acid +95% ethanol electrolyte at  $255 \pm 5$  K, a voltage of  $45 \pm 5$  V, and a current of  $105 \pm 10$  mA. The TEM thin foils were irradiated with 1 MeV Kr ions at 500°C to 1 dpa under in-situ observation using

the Intermediate Voltage Electron Microscope (IVEM)-Tandem Facility at Argonne National Laboratory (ANL) with a flux of  $6.3 \times 10^{15}$  ions/(m<sup>2</sup>·s). And the irradiation condition was summarized in Table 4.3. The ion irradiation dose was computed by the Stopping and Range of Ions in Matter (SRIM) code with the quick Kinchin-Pease option [90] shown in Figure 4.1. The defect evolution was observed in the same area of an [011]-oriented foil. The area was ~150 nm thick as assessed from the spacing of the thick fringes. The microscope was operated at 300 kV.

**Table 4.1 The nominal chemical composition (at%) of Co-free Cu-containing alloys**

Alloys	Cu	Ni	Fe	Cr	Al	C	N
CuNi	49.9	49.9	-	-	-	0.007	0.0008
Cu <sub>0.3</sub> NiFeCr	9.9	29.9	29.9	29.9	-	0.005	0.0007
Al <sub>0.4</sub> CuFeCrNi <sub>2</sub>	18.4	37	18.4	18.4	7.4	0.011	0.0004

**Table 4.2 Electro-polishing conditions of Co-free Cu-containing alloys**

Electrolyte	Ethanol: Perchloric acid = 19:1
Voltage (V)	30.0~50.0
Current (mA)	90~120
Temperature (°C)	-20.0~ -30.0

**Table 4.3 Kr ion irradiation conditions of Co-free Cu-containing alloys**

Acceleration voltage	1 MeV
Temperature	500 °C
Dose rate	$1.0 \times 10^{-3}$ dpa/s
Irradiation dose	~1dpa

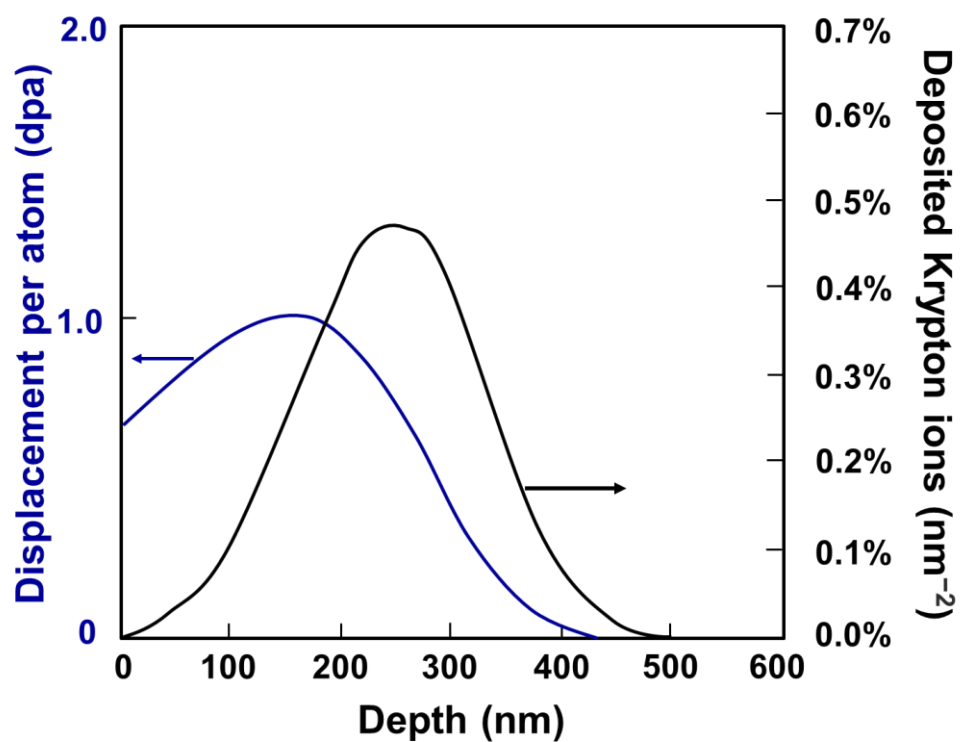
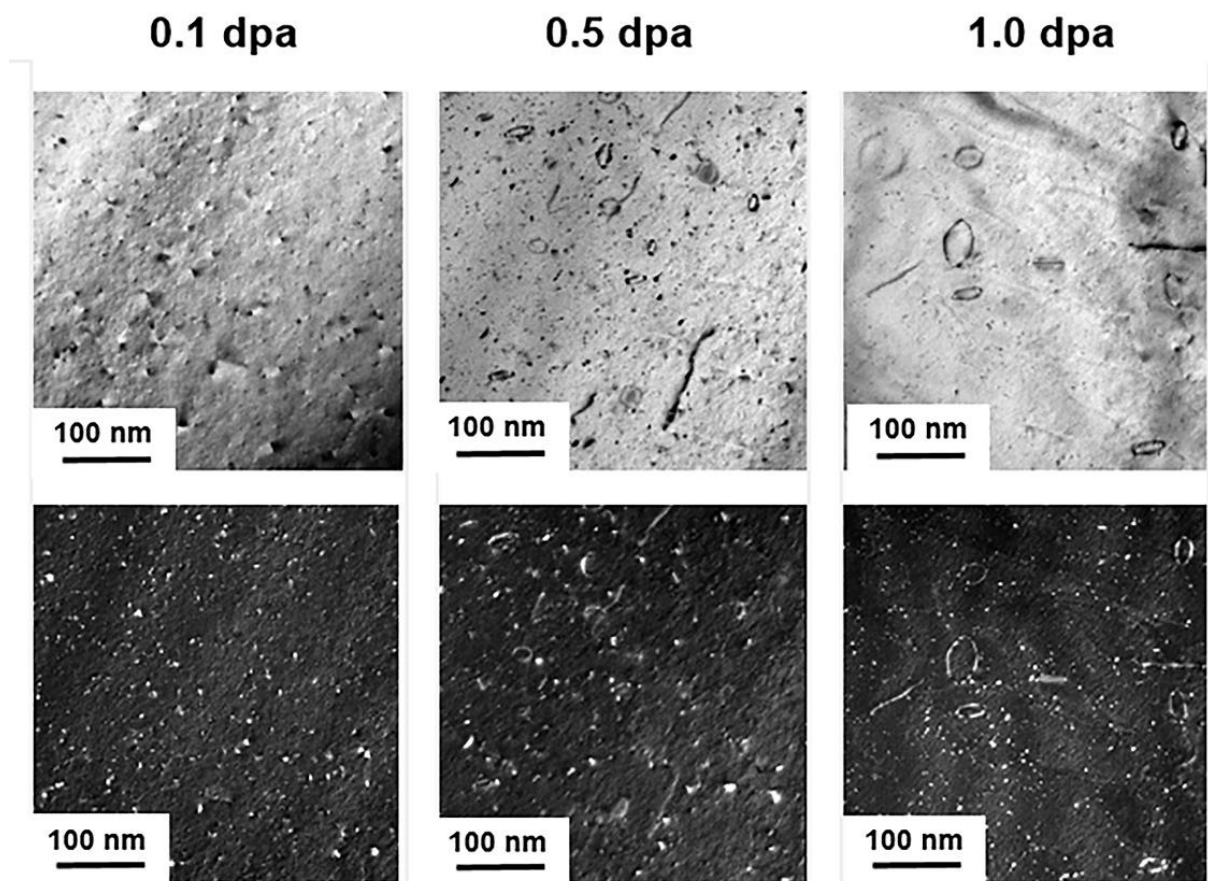


Figure 4.1 SRIM plots showing the calculated damage (blue line) and implanted ion profiles (black line) of 1 MeV Krypton ions in CSAs normalized to an ion fluence of  $6.3 \times 10^{14}$  ions/cm<sup>2</sup>.



### 4.3 Irradiation effects on microstructure

Figure 4.2-4.4 shows the evolution of defect structure as a function of ion dose at 500°C in CuNi, Cu<sub>0.3</sub>NiFeCr, and Al<sub>0.4</sub>CuFeCrNi<sub>2</sub>. Irradiation-induced black dots and Frank loops were observed in the irradiated area of all materials and grew with increasing irradiation dose. No void was observed. In the binary alloy CuNi, as shown in Figure 4.2, the irradiated microstructures consist of a high density of stacking fault tetrahedra (SFTs). Between an ion dose of 0.5-1 dpa the defect density decreased and some large loops appeared. In the quaternary alloy Cu<sub>0.3</sub>NiFeCr, as shown in Figure 4.3, only a few defect clusters are SFTs, while the other features don't have a well-defined shape. The defects density at 0.1 dpa appears to be qualitatively similar to that in CuNi. With increasing ion dose to 1 dpa, in contrast to the CuNi alloy, higher density and smaller size of loops were observed in Cu<sub>0.3</sub>NiFeCr. In high-entropy alloy Al<sub>0.4</sub>CuFeCrNi<sub>2</sub>, as shown in Figure 4.4, no SFTs was observed. And much higher density and smaller size of loops in Al<sub>0.4</sub>CuFeCrNi<sub>2</sub> at 1 dpa observed than that in CuNi and Cu<sub>0.3</sub>NiFeCr. It is well known that the agglomeration of vacancies may result in the formation of stacking fault tetrahedra (SFTs) in the face-centered cubic (fcc) lattice, and irradiation-induced stacking fault tetrahedra in fcc metals, pure Cu, Ni, and Al were reported [91], which shows that Cu presents 90% of SFTs while Ni present values of 40–50%. Al is not shown. The phenomenon that no SFTs were observed in Al<sub>0.4</sub>CuFeCrNi<sub>2</sub> may be understood by the cocktail effect. For the HEAs that break through the traditional design concept, the cocktail effect does not mean that the performance of the alloys is simply a superposition of the properties of each component. There are also interactions between different elements that eventually lead to a composite effect in HEAs [92].



**Figure 4.2** The BF (top) and WBDF (bottom) TEM micrographs of CuNi irradiated with 1 MeV Kr ions at 500 °C. The WBDF diffraction condition was  $g = 200$  ( $g, 5g$ ) at 011zone.

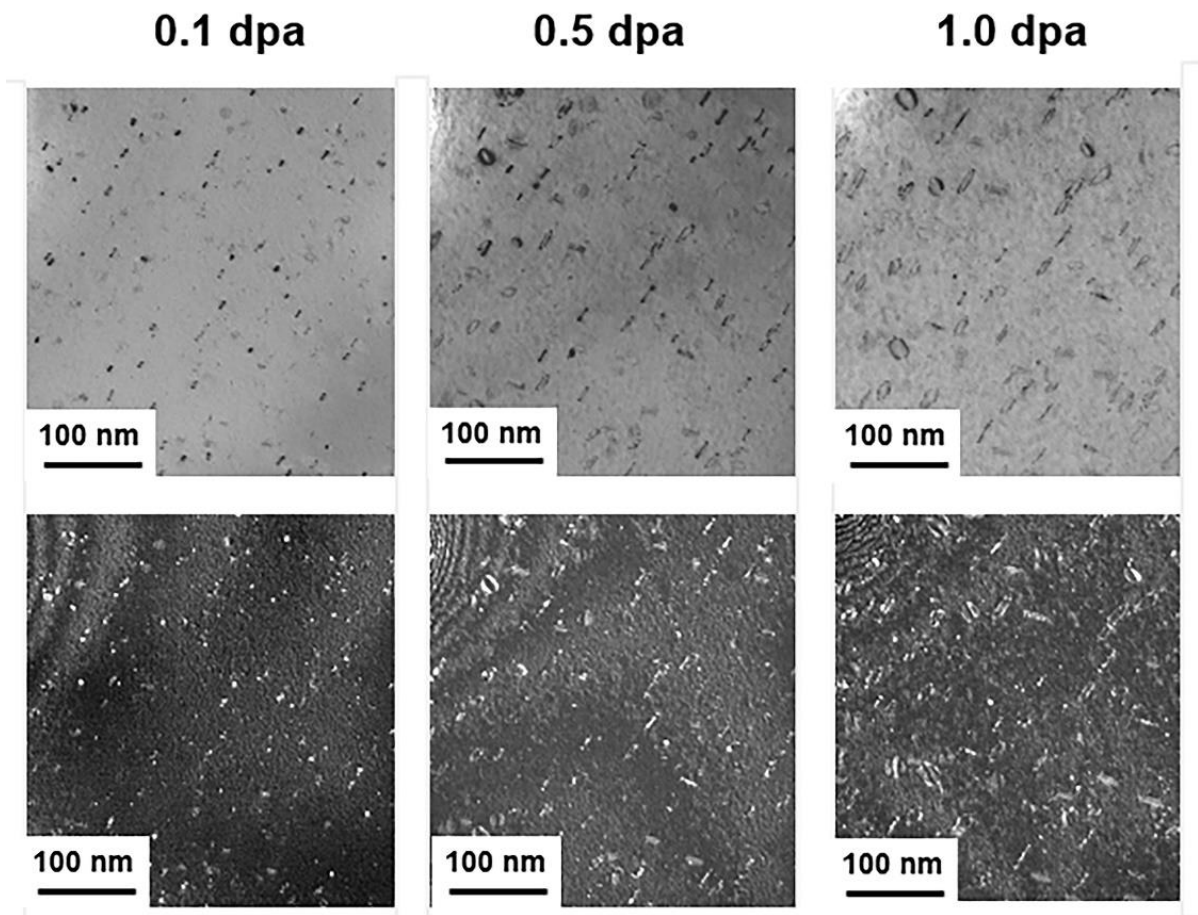


**Figure 4.3** The BF (top) and WBDF (bottom) TEM micrographs of  $\text{Cu}_{0.3}\text{NiFeCr}$  irradiated with 1 MeV Kr ions at 500 °C. The WBDF diffraction condition was  $g = 200$  ( $g, 5g$ ) at 011zone.

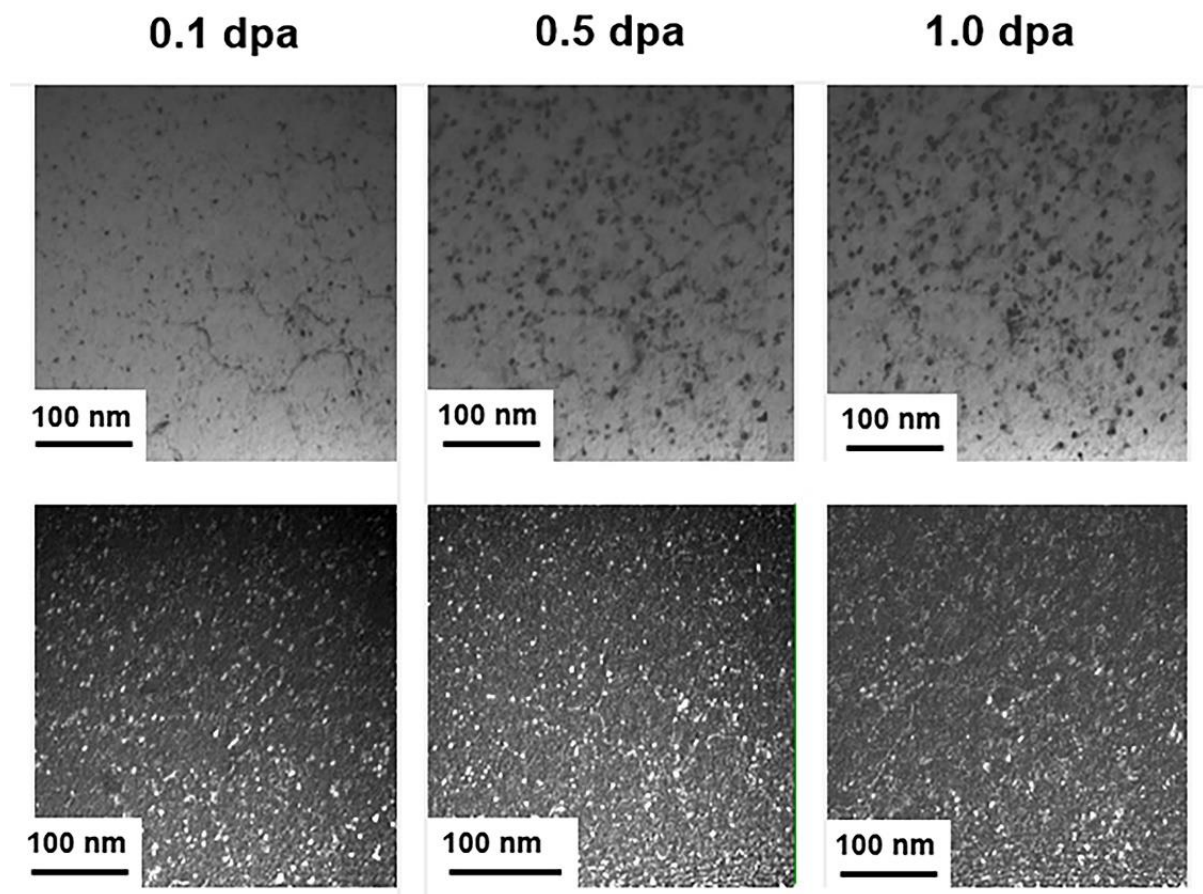


**Figure 4.4** The BF (top) and WBDF (bottom) TEM micrographs of  $\text{Al}_{0.4}\text{CuFeCrNi}_2$  irradiated with 1 MeV Kr ions at 500 °C. The WBDF diffraction condition was  $g = 200$  ( $g, 5g$ ) at 011zone.

Figure 4.5-4.7 shows the Bright-field images and the size distribution of SFTs, black dots, and Frank loops in of CuNi, Cu<sub>0.3</sub>NiFeCr, and Al<sub>0.4</sub>CuFeCrNi<sub>2</sub> irradiated with 1 MeV Kr ions at 500 °C to 1 dpa. The surface effect needs to be studied as a function of foil thickness to understand the microstructural evolution of thin foils. Thus, ex-situ TEM images were taken at different foil thickness of ~60 nm and ~200 nm after irradiation to 1 dpa.

Most of the defects found at a foil thickness of ~60 nm are small defect clusters for all materials. Over 90% of defect clusters were identified as SFTs in the CuNi. While for the Cu<sub>0.3</sub>NiFeCr, and Al<sub>0.4</sub>CuFeCrNi<sub>2</sub>, a high portion of defects clusters (black dots) do not have a well-defined shape and are considered as vacancy clusters. And the presence of vacancy clusters in the thin regions might be explained with two mechanisms. On the one hand, as the migration energy of interstitials is much smaller than that of vacancies, the surface-affected zone for interstitials clusters was much deeper than that for vacancy clusters. This imbalance between interstitials and vacancies can reduce the recombination and enhance the formation of vacancy clusters in the vicinity of the foil surface [93]. As a result, there were still sufficient vacancies to form SFTs or vacancy clusters in the thin regions while large interstitial loops were absent. On the other hand, the vacancies can cluster by cascade collapse [94]. The migration energy of vacancies would be further increased after clustered, and the chance to be lost to the foil surface for vacancies would be trivial.

Large dislocation loops began to occur uniformly when the foil thickness was greater than 100 nm for all materials. With the foil thickness, the areal density of dislocation loops increased. Up to 200 nm in thickness, no quantitative measurement was conducted on the SFTs and small defect clusters because small defect clusters are difficult to picture in foils thicker than 60 nm.

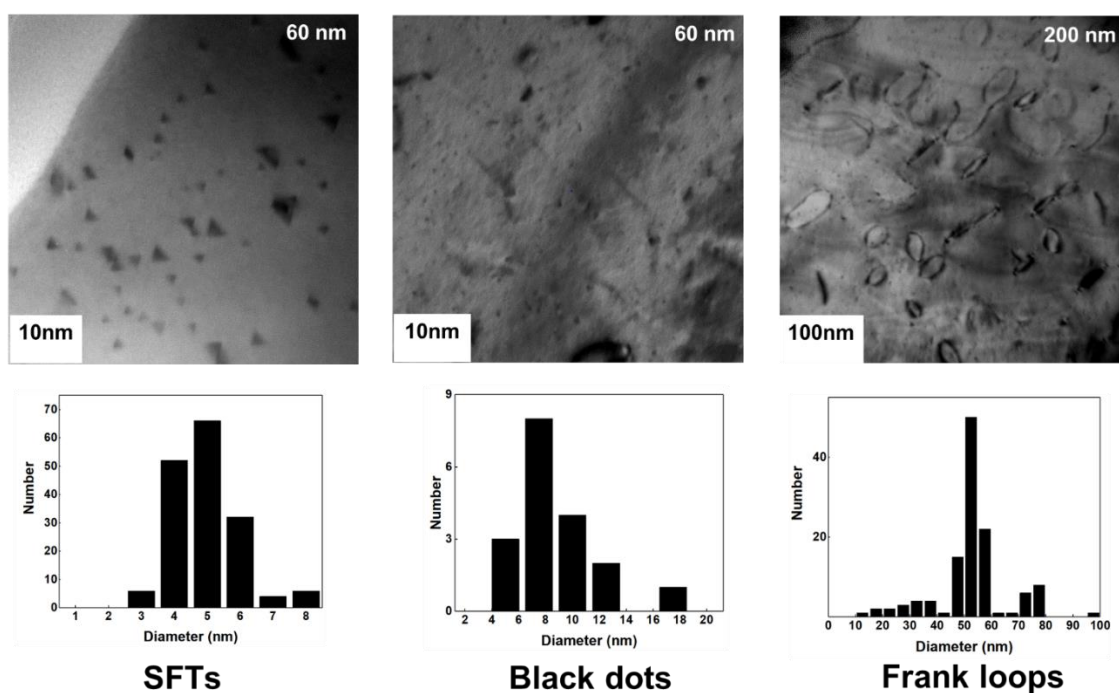


**Figure 4.5** Bright-field TEM images and the size distribution of SFTs, black dots, and Frank loops in CuNi irradiated with 1 MeV Kr ions at 500 °C to 1 dpa. Micrographs were taken of the foil at 011zone where  $g = 111$  was strongly reflected.

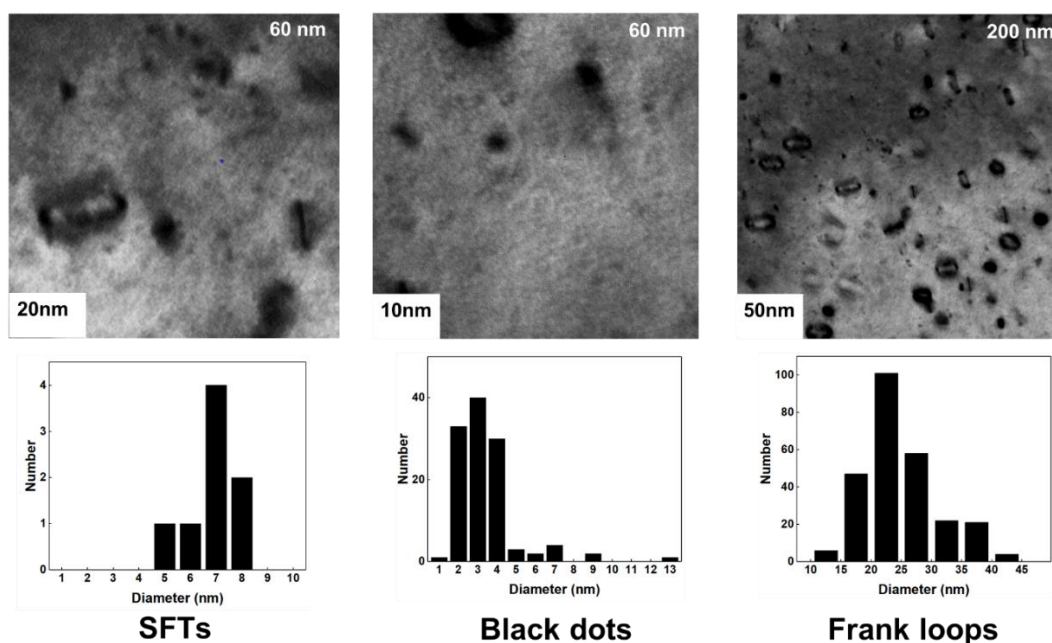


**Figure 4.6** Bright-field TEM images and the size distribution of SFTs, black dots, and Frank loops in  $\text{Cu}_{0.3}\text{NiFeCr}$  irradiated with 1 MeV Kr ions at 500 °C to 1 dpa. Micrographs were taken of the foil at 011zone where  $g = 111$  was strongly reflected.

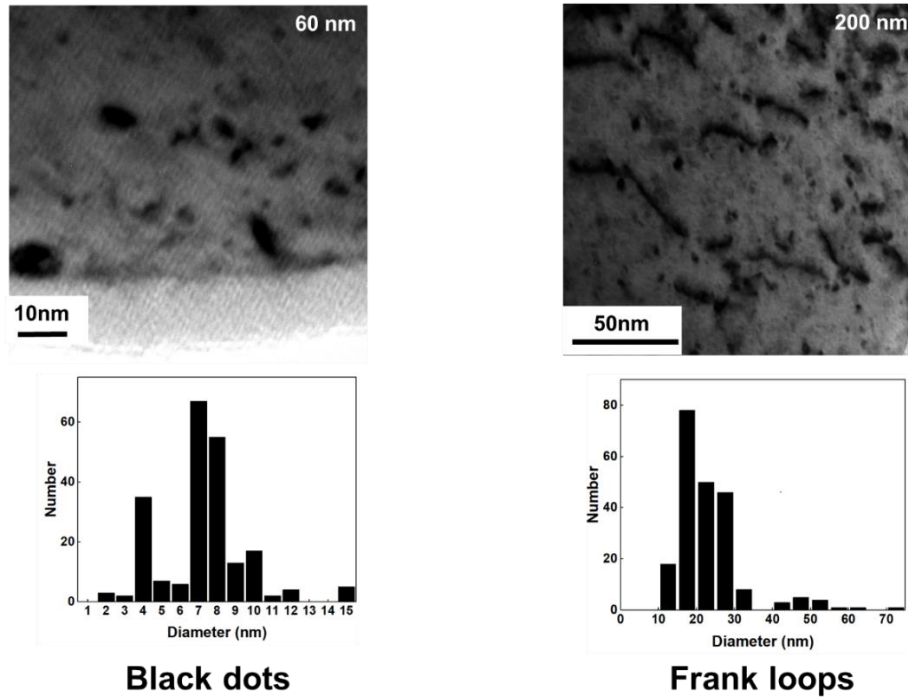


**Figure 4.7** Bright-field TEM images and the size distribution of SFTs, black dots, and Frank loops in  $\text{Al}_{0.4}\text{CuFeCrNi}_2$  irradiated with 1 MeV Kr ions at 500 °C to 1 dpa. Micrographs were taken of the foil at 011zone where  $g = 111$  was strongly reflected.

The number density and average size of stacking fault tetrahedra (SFTs), black dots and Frank loops in CuNi,  $\text{Cu}_{0.3}\text{NiFeCr}$ , and  $\text{Al}_{0.4}\text{CuFeCrNi}_2$  Kr ion irradiated at 500 °C to 1 dpa was shown in Figure 4.8. They show the respective contributions of SFTs, black dots, and Frank loop visible populations. It appears that CuNi presents 90% of SFTs while  $\text{Cu}_{0.3}\text{NiFeCr}$  presents values of less than 1%.  $\text{Al}_{0.4}\text{CuFeCrNi}_2$ , as it contains a high concentration of defect clusters that appear as black spots, which were not identified. And the black dots in all materials were too small to distinguish from tiny Frank loops. In this study, we defined black dots as 10 nm or less in size and loops as 10nm or over in size, respectively.

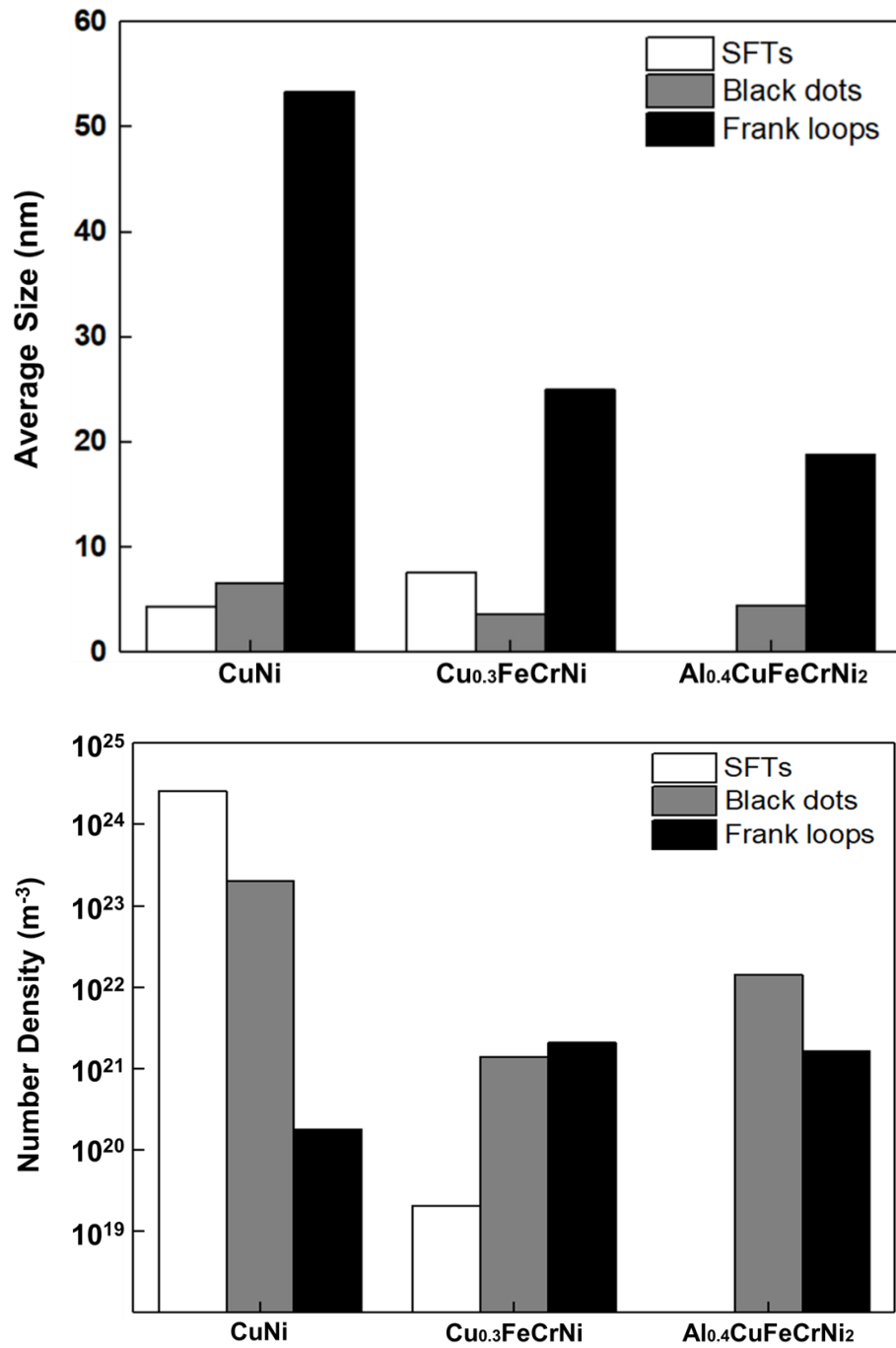


**Figure 4.8** Number density and average size of stacking fault tetrahedra (SFTs), black dots and Frank loops in CuNi, Cu<sub>0.3</sub>NiFeCr, and Al<sub>0.4</sub>CuFeCrNi<sub>2</sub> irradiated with 1 MeV Kr ions at 500 °C to 1 dpa.



In order to understand the microstructure evolution in face-centered cubic Co-free Cu-containing solid solution concentrated alloys, the influence of increasing the number of elements in the alloy on the intrinsic properties is taken into consideration. The diffusion of elements has been reported to be more sluggish in the more complex alloys and to be chemically inhomogeneous [95], which will impact the formation of defects as well as the segregation of elements to them. And the calculation research has shown that the band structures are smeared even in the binary alloys, and smeared out larger in the quaternary alloy [96]. This smearing is related to the electronic mean free path, which is expected that energy dissipation through the electronic system will be reduced through the addition of elements to the alloy. Besides, each atom experiences its own compositional environment as its nearest neighbors are different for all materials. And contributions from both the composition and the local environment surrounding each element will serve to reduce the phonon mean free path, which will reduce the capacity of the system to transport energy [7]. These effects predicted that the lifetime of displacement cascades will be increased. Hence, there is greater recombination of interstitials and vacancies, thereby the smaller dislocation loops produced by irradiation with increasing alloy content would be predicted.

The phenomenon of the lowest number density of SFTs and the lowest average loop size of Frank loops in HEA ( $\text{Al}_{0.4}\text{CuFeCrNi}_2$ ) may be explained by stacking fault energy and the shear modulus of the material. Lower stacking fault energies (SFE) in materials would form stacking fault-type defects, such as stacking fault tetrahedron (SFT) and Frank loops (FLs) in the matrix after irradiated in a wide temperature range [97]. It is reported that stacking fault energy and the shear modulus of the material are the conditions for the formation and stabilization of SFTs in fcc metals. When the reduced stacking fault energy,  $\gamma/\mu b$ , is smaller than about 1/50 SFTs are favourable [91]. Also, in the studies by Hashimoto [98], higher SFE may be dependent on

the Mn concentration in irradiated CoCrFeNiMnx alloys, leading to a smaller average loop size of Frank loops. Thus, it is possible that Al<sub>0.4</sub>CuFeCrNi<sub>2</sub> had a lower stacking fault energy,  $\gamma/\mu b$ , that leads to a lower number density of SFTs and a lower average loop size of Frank loops.

## 4.4 Irradiation hardening

Orowan equation was used to estimate the hardening related to the microstructures observed by TEM. The formulas are given as follows:

$\Delta\sigma_y = M\alpha\mu b\sqrt{Nd}$	(4.1)
$\Delta H_c = K\Delta\sigma_y$	(4.2)

where  $\Delta\sigma_y$  and  $\Delta H_c$  are the calculated increase in yield strength and hardness after irradiation, respectively. The barrier strength factor  $\alpha$  of Frank loops is 0.4, and the barrier strength factor  $\alpha$  of SFTs and black dots (vacancy clusters) is 0.2 [99,100]. The Burgers vector  $b$  is 0.257 nm for all materials. The shear modulus  $\mu$  is 77 GPa, the same as that of austenitic steels [88]. Taylor factor,  $M$ , is selected as 3.06 for equiaxed fcc. The  $N$  and  $d$  are the density and size of the dislocation loops at 1 dpa, respectively. The constant  $K$  is 3 for irradiated austenitic stainless steels [88,101]. As suggested in Refs [102], the radiation hardening of alloys was measured using the root-sum-square law,  $\Delta\sigma_y = \sqrt{\sum_i (\Delta\sigma_{y,i})^2}$ , for defects with similar strength. As shown in Table 4.3, the calculated increases in hardness  $\Delta H_c$  for the  $\text{Cu}_{0.3}\text{NiFeCr}$  and  $\text{Al}_{0.4}\text{CuFeCrNi}_2$  alloys were similar, while it was much lower than the CuNi. Compared with reported irradiation hardening of 316H SS at 500°C, which ignored the effect of SFTs and vacancy dislocation loops [46], the HEA shows the lowest level of irradiation hardening than the low-entropy alloy (CuNi) and the 316H SS. This result provides a promising sign for the applications of Co-free high-entropy alloys at high-temperature nuclear reactors, such as molten salt reactor (550-700°C) and sodium fast reactor (400-600°C) [103]. However, nanoindentation measurement would be needed to assess the accuracy of the estimated results due to the parameters of the hardening model (e.g.  $\alpha$  and  $K$ ).

**Table 4.4 Mean diameter and number density of SFTs, black dots, Frank loops, and hardness measured of Co-free Cu-containing alloys**

		$N_d$ (m <sup>-3</sup> )	$d_{ave}$ (nm)	$\Delta\sigma_y$ (GPa)	$\Delta H_c$ (GPa)
CuNi	SFTs	$4.1 \times 10^{24}$	4.4	4.90	16.20
	Black dots	$3.1 \times 10^{23}$	6.6	0.74	
	Frank loops	$2.5 \times 10^{20}$	53.4	0.27	
Cu <sub>0.3</sub> NiFeCr	SFTs	$3.2 \times 10^{19}$	7.6	0.04	1.95
	Black dots	$1.5 \times 10^{21}$	3.6	0.09	
	Frank loops	$3.2 \times 10^{21}$	25	0.65	
Al <sub>0.4</sub> CuFeCrNi <sub>2</sub>	SFTs	0	0	0	1.65
	Black dots	$1.6 \times 10^{22}$	4.5	0.30	
	Frank loops	$2.2 \times 10^{21}$	18.8	0.47	
316H [46]	Frank loops	$2.3 \times 10^{22}$	10	1.10	3.30

## 4.5 Summary

The Co-free Cu-containing solid solution concentrated alloys, CuNi, Cu<sub>0.3</sub>NiFeCr, Al<sub>0.4</sub>CuFeCrNi<sub>2</sub> were irradiated at 500 °C with 1 MeV krypton ions to 1 dpa with in-situ TEM observations. The irradiation damage resulted in a high density of defects in all three materials. SFTs were observed in the CuNi and Cu<sub>0.3</sub>NiFeCr after irradiation, but not in Al<sub>0.4</sub>CuFeCrNi<sub>2</sub>. The loop density was dependent on the alloy composition. The alloy composition influences the type of defect. At 1 dpa, the order of maximum loop size was Al<sub>0.4</sub>CuFeCrNi<sub>2</sub> < Cu<sub>0.3</sub>NiFeCr < CuNi.

The order of loop density was CuNi < Cu<sub>0.3</sub>NiFeCr < Al<sub>0.4</sub>CuFeCrNi<sub>2</sub>. The calculated hardening results indicate that the irradiation hardening at 500°C was less in HEA (Al<sub>0.4</sub>CuFeCrNi<sub>2</sub>) and Cu<sub>0.3</sub>NiFeCr than in CuNi and 316H SS. While further nanoindentation experiments for measured hardening results are still needed. The results indicate that the Al<sub>0.4</sub>CuFeCrNi<sub>2</sub> alloy would have the potential to be a Co-free high-entropy alloy applicable to nuclear reactor components at high temperatures.

## Chapter 5

---

# Computational approach on the stability of HEAs by the first-principles DFT calculations

---

## 5.1 Introduction

High entropy alloys (HEAs) have become a hot topic in materials science field. Due to the extraordinary properties of HEAs family such as excellent mechanical properties [33,100,101], good corrosion resistance [32,102] and high irradiation tolerance [54,93,103-105], many efforts have been devoted to study the nature of HEA [106-112], develop HEA with more remarkable properties [100,101,113] and also explore the new HEAs family [110,114-116]. The high irradiation tolerance of HEAs makes the application of HEAs as nuclear materials in energy industries be possible [117,118]. Therefore, the irradiation behavior of kinds of HEAs has been studied with experimental method in the past works. Experimental study focused on the irradiation behavior of NiCoFeCr [54,93,119], NiCoFeCrMn [54], CoCrCuFeNi [120] Al<sub>0.1</sub>CoCrFeNi [121] and CrMnFeCoNi [122] are reported. It is noticeable that in these works, cobalt is contained in the HEAs. So far, there is just a few works report Co-free HEA. Kumar et al. studied the ion irradiation behavior of FeNiMnCr [42]. They found that FeNiMnCr is stable after ion irradiation 400-700 °C. And, the Fe-Ni-Mn-Cr HEA has better swelling resistance than conventional Fe-Cr-Ni austenitic alloys. Furthermore, The lower defect cluster size and higher cluster density for the irradiated Fe-Ni-Mn-Cr HEA compared to conventional Fe-Cr-Ni alloys at 400-700 °C was observed in their experimental observation, which is consistent with reduced point defect mobility for HEAs. They attributed this phenomenon to the reduction in the mobility of point defects. Li et al studied the neutron irradiation behavior of FeNiMnCr. They concluded that FeNiMnCr has comparable mechanical performance and phase stability as commercial stainless steel after a low dose, near room temperature neutron irradiation. However, there was also a lack of quantitative knowledge of the energies involved in these systems and the impact of ordering within these alloys.

Interstitial atoms like hydrogen (H), Helium (He), carbon (C) and nitrogen (N) are well known to have a significant impact on the mechanical properties of metals. Very recently, several research works focused on the doping effect of these interstitials on the CrCoFeNi HEA family. It is found that H with appropriate amount can be utilized to tune beneficial strengthening and toughening mechanisms rather than undergoing catastrophic failure due to hydrogen embrittlement [104]. C doping can increase the yield strength, ultimate tensile strengths as well as plasticity of HEA [105]. Moreover, N increases the hardness of HEA [106]. These researches have proved that the doping effect of interstitial in CrCoFeNi HEAs is significant and particular. However, the solution behavior of these interstitials and how they affect the physical properties of CrCoFeNi HEA have not been completely understood.

In the previous chapters, experimental techniques were conducted to face-centered cubic Co-free concentrated solid solution alloys (CSAs) to assess the potential of application in the fusion reactor. In this chapter, properties of the face-centered cubic Co-free alloys CuNi, CuNiFe, CuNiFeCr, and Cu<sub>0.3</sub>NiFeCr are investigated by density functional theory calculation. And the vacancy formation energy  $E_v^f$  and interstitial formation energy  $E_i^f$  of Cu and Ni elements in alloys are considered. Also, the fundamental phenomena of H, He, C and N in CrCoFeNi HEA, and their effect on the physical properties, electronic structures of CrCoFeNi HEA are investigated with density functional theory (DFT) calculation.



## 5.2 Calculation method

All the calculations in this work are performed with the program packages GPAW [107]. The Generalized Gradient Approximation (GGA) PBE [108] functional is used for exchange-correlation. The interaction between the valence and core electrons is modelled with projector augmented wavefunctions [109]. A plane wave cut-off of 500 eV is applied together with a smearing of electronic states of 0.1 eV. According to our experimental results, CuNi, CuNiFe, CuNiFeCr, Cu<sub>0.3</sub>NiFeCr and CrCoFeNi HEA are considered to be solid solutions with fcc structure. They are modelled with a  $(3 \times 3)$  fcc supercell which containing 108 atoms. A  $3 \times 3 \times 3$  k-point grid is utilized for sampling Brillouin zones. The randomness of solutes in the lattice sites is achieved by implementing the special quasi-random structure (SQS) method, as used in previous work [110]. Spin-polarization effects are taken into consideration for all calculations. Each structure is fully relaxed until the atomic force is less than 0.03 eV. Furthermore, for the calculation includes H atom, due to the small mass of H atom, zero-point vibrational (ZPV) energy is considered.

### 5.3 Fundamental properties of CuNi, CuNiFe, CuNiFeCr and Cu<sub>0.3</sub>NiFeCr alloys

The XRD patterns of annealed CuNi, CuNiFe, CuNiFeCr and Cu<sub>0.3</sub>NiFeCr are seen in Fig 5.1. It is obvious that all the annealed alloys have fcc structures and no other structure can be found in the XRD pattern, which demonstrates that annealed alloys are all solid solutions with fcc structures.

The lattice constants of CuNi, CuNiFe, CuNiFeCr, and Cu<sub>0.3</sub>NiFeCr was determined from the XRD measurements and the first estimates of the principles. The findings are shown in Table 5.1. The lattice constants of Cu and Ni are also calculated as a reference. It can be found that the CuNi ternary alloy has the smallest lattice constant of 3.575 Å. Besides, alloys with more than three 2 components have a larger lattice constants, which is consistent with the previous study on other HEAs [110]. In all cases, the lattice constant calculated from first principles calculations is consistent with the experimental value, the maximum difference between them is less than 1%. Furthermore, for CuNi, a recent report is found which reports almost the same value of lattice of CuNi (3.57 Å) as the value obtained in this work. These facts prove the validity of the calculation results.

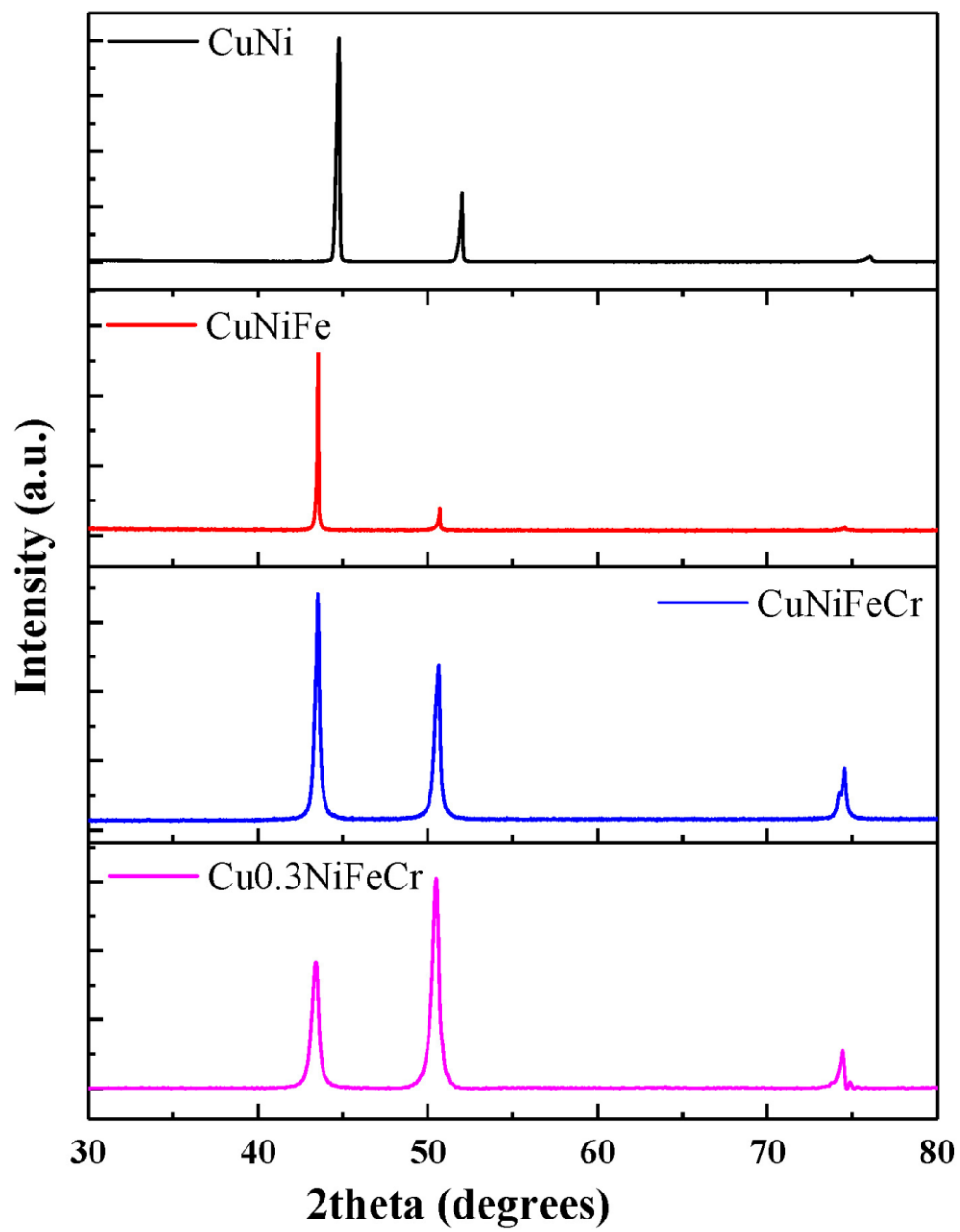


Figure 5.1 XRD patterns of annealed CuNi, CuNiFe, CuNiFeCr and Cu<sub>0.3</sub>NiFeCr alloys.

The thermodynamic stability of alloys can be estimated by calculating the cohesive energy and formation enthalpy. In contrast to the gas state, cohesive energy is the energy obtained from arranging the atoms in a crystalline state, and the standard formation enthalpy is characterized as a change in enthalpy when one mole of a substance in the standard state (1 atm of pressure and 298.15 K) is formed by its pure elements under the same conditions. In general, negative values of the cohesive energy and formation enthalpy indicate the alloy systems are thermodynamically stable. And, the smaller the negative values of these two thermodynamic parameters, the more stable the alloys. The cohesive energy and formation enthalpy for CuNi, CuNiFe, CuNiFeCr and Cu<sub>0.3</sub>NiFeCr alloys are calculated and summarized in Table 5.1, which indicates that face-centered cubic Co-free alloys we have developed are stable alloys. The calculated cohesive energy and formation enthalpy of CuNi is highly consistent with the previous report [111].

**Table 5.1** Lattice constant, cohesive energy and formation enthalpy of CuNi, CuNiFe, CuNiFeCr and Cu<sub>0.3</sub>NiFeCr alloys

	Lattice constant		Cohesive energy (eV/atom)	Formation enthalpy (eV/atom)
	Exp.	Cal.		
Cu	3.616 Å [112]	3.636 Å	-	-
Ni	3.524 Å [113]	3.520 Å	-	-
CuNi	3.575 Å	3.579 Å 3.57 Å [111]	-4.16	0.026
CuNiFe	3.597 Å	3.593 Å	-4.62	-0.098
CuNiFeCr	3.606 Å	3.606 Å	-4.38	0.040
Cu <sub>0.3</sub> NiFeCr	3.602 Å	3.581 Å	-4.63	0.016

One characteristic of HEAs is the local structural disorder. Local structural disorder of HEAs can be traced by computing structural corrugation within HEAs. Structural corrugation is defined as the difference between the larger and smaller Z coordinates of the atoms in each atom layer [114]. In this work, the structural corrugation in (100), (110), and (111) plane of CuNi, CuNiFe, CuNiFeCr, and Cu<sub>0.3</sub>NiFeCr alloys are checked, the results are given in Fig 5.2. It is clear that with increases in component, the structural corrugation in different plane increases. For CuNi and CuNiFe alloys, it seems no significant difference in the structural corrugation in different planes. For CuNiFeCr and Cu<sub>0.3</sub>NiFeCr alloys, however, it is found that the structural corrugation in the different plane is different from each to each. (111) plane has the most severe structural corrugation and followed by (110) plane and (100) plane. Obviously, structural corrugation in equimolar HEA (CuNiFeCr) is more extreme than in non-equimolar HEA (Cu<sub>0.3</sub>NiFeCr), which suggests that the higher entropy, the stronger local structural disorder.

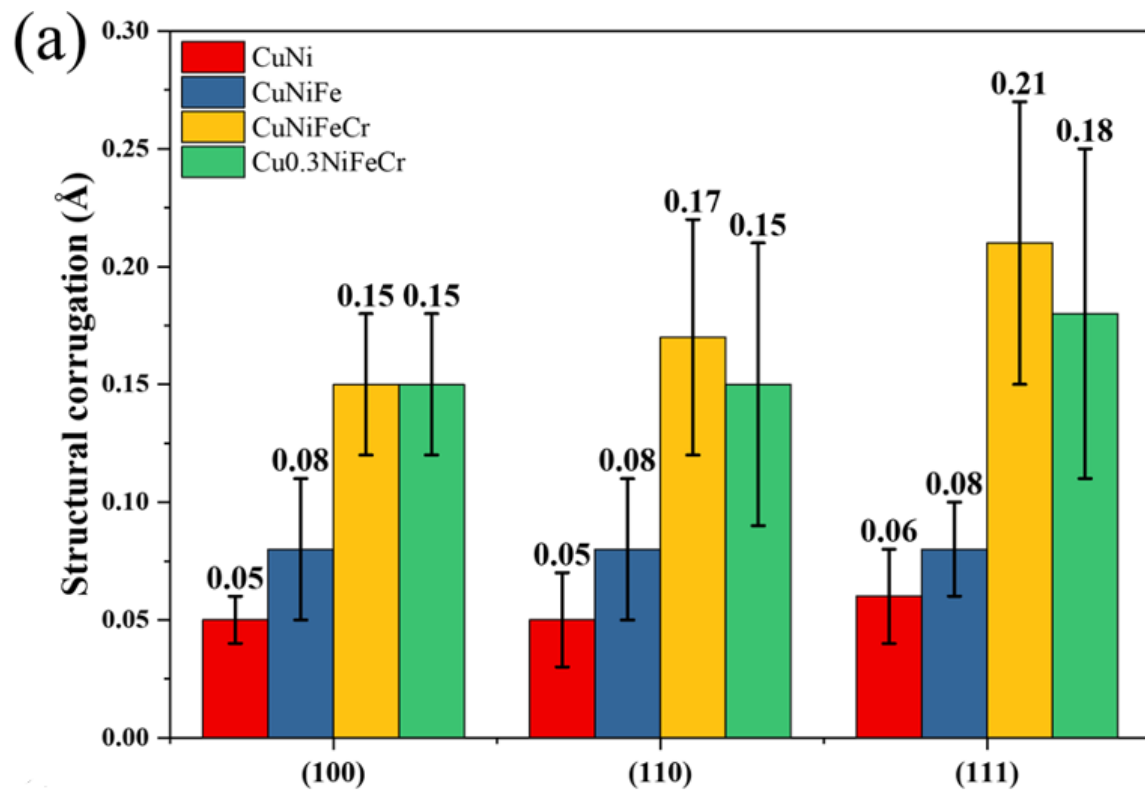
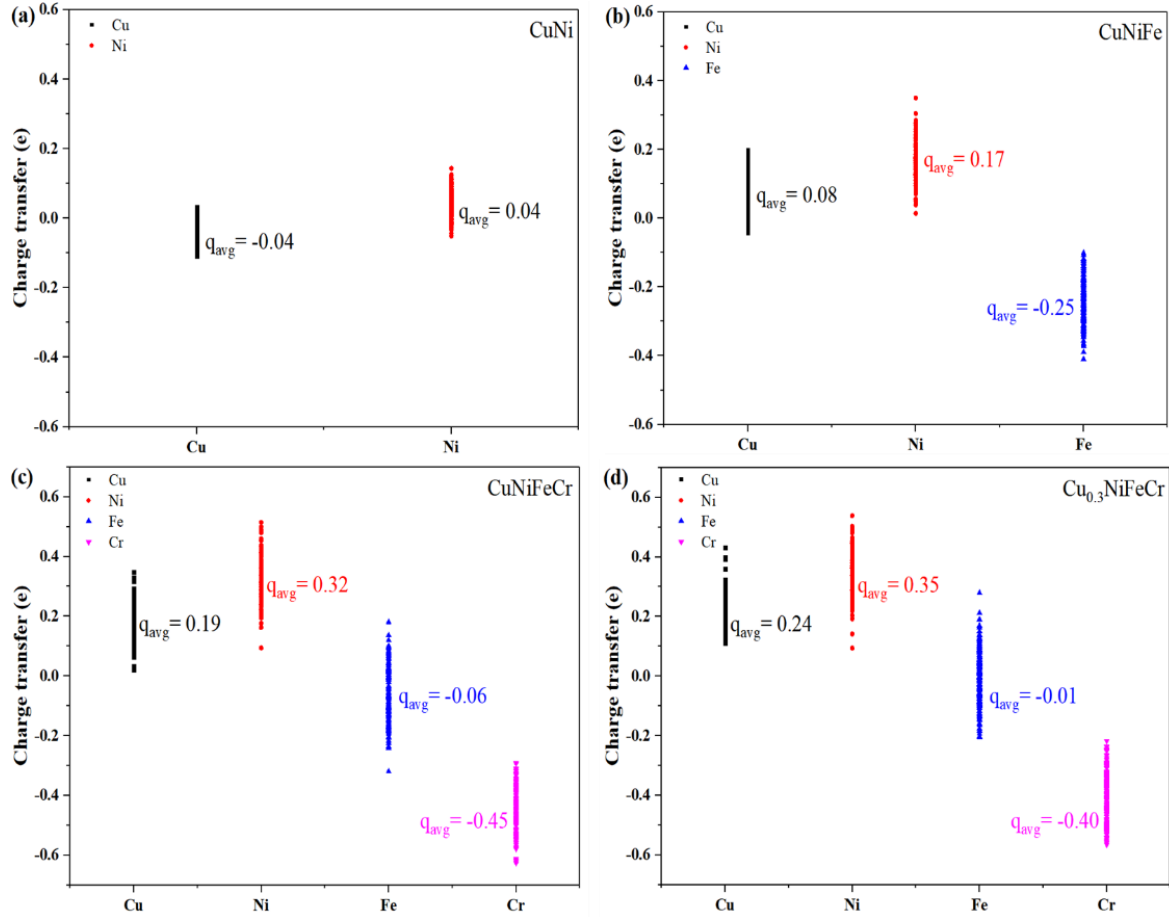


Figure 5.2 Structural corrugation in (100), (110) and (111) plane of CuNi, CuNiFe, CuNiFeCr and Cu<sub>0.3</sub>NiFeCr alloys.

## 5.4 Magnetic and electronic properties of CuNi, CuNiFe, CuNiFeCr and Cu<sub>0.3</sub>NiFeCr alloys



**Figure 5.3** Charge transfer of each solute atom in (a)CuNi, (b)CuNiFe, (c)CuNiFeCr and (d)Cu<sub>0.3</sub>NiFeCr alloys.

The charge transfer of each solute atom in CuNi, CuNiFe, CuNiFeCr and Cu<sub>0.3</sub>NiFeCr is present in Fig 5.3. As shown in Fig 5.3 (a), in CuNi, there is no significant electrons transferred occurred between Cu and Ni. In average, Cu atoms have a negative charge of -0.04 electrons and Ni atoms have a positive charge of 0.04 electrons. In CuNiFe (Fig 5. (b)), it is clear that Cu and Ni atoms have positive charges and Fe atoms have negative charges. which means Cu and Ni atoms tend to be the electron acceptor, while Fe atoms tend to be the electron donor. In Fig 5.3(c) and Fig 5.3(d), It can be found that after Cr is added, Cr atoms become the main electron donor in

the alloys. Cu and Ni atoms are still the electron acceptor. For Fe atoms, half of them play the role of electron donor but another half play the role of electron acceptor, and as a result, Fe has the charge value close to 0 electrons.

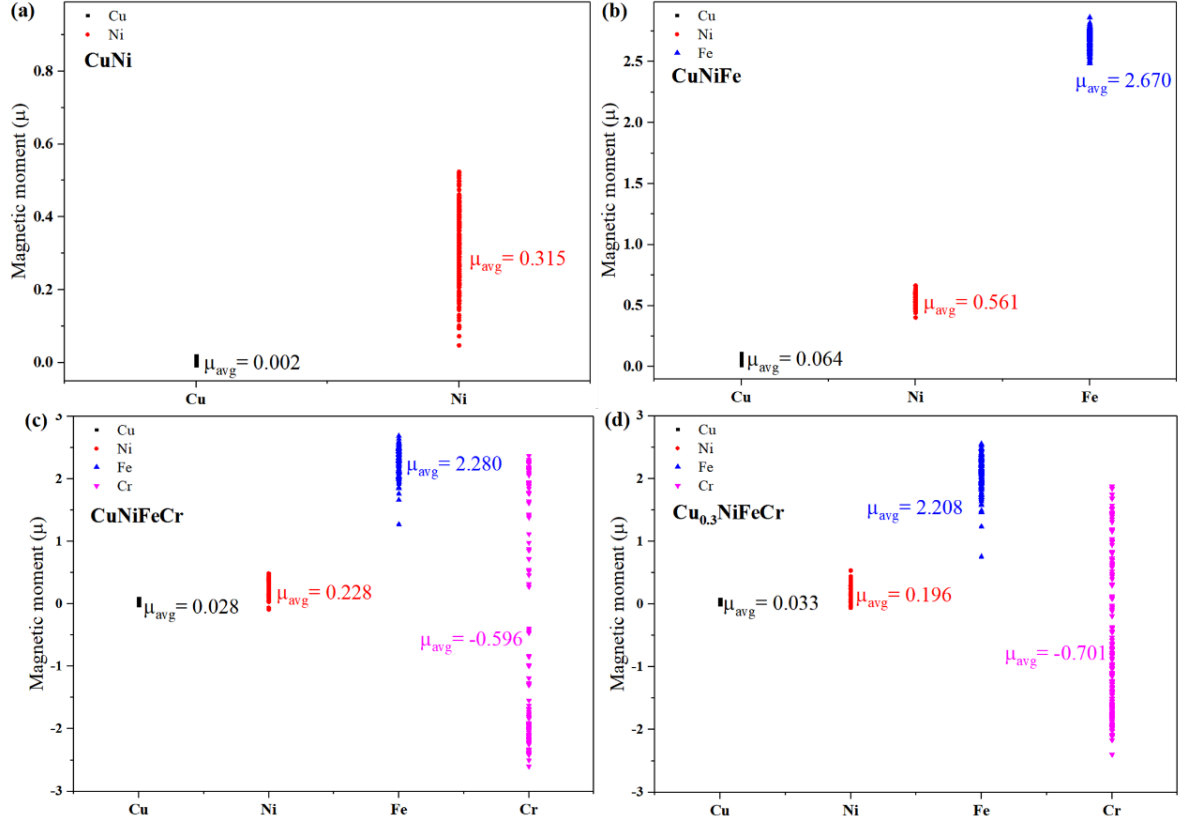


**Figure 5.4** Magnetic moment of each solute atom in (a)CuNi, (b)CuNiFe, (c)CuNiFeCr and (d)Cu<sub>0.3</sub>NiFeCr alloys.

In this work, CuNi, CuNiFe, CuNiFeCr and Cu<sub>0.3</sub>NiFeCr alloys are all calculated to be ferromagnetic, which is the same as the reported CoCrFeNi [115]. The Magnetic moment of each solute atom in CuNi, CuNiFe, CuNiFeCr and Cu<sub>0.3</sub>NiFeCr alloys are shown in Fig 5.4. In these alloys, it is clear that the magnetic moment of Cu atoms shows a very small value, which is consistent with the paramagnetic property of Cu atoms in bulk. And, Fe and Ni are the main solutes that produce the magnetic moment in the same direction. However, Cr is always antiferromagnetically aligned to the ferromagnetic Fe and Ni. The phenomenon of Cr being



antiferromagnetically aligned with other ferromagnetic atoms is also reported in CoCrFeNi [116] and CoCrFeMnNi [117] alloys. Fe and Ni atoms have high magnetic moment values in CuNiFe alloy, compared with in other alloys. Compared to the magnetic moment of solutes in CuNiFeCr and Cu<sub>0.3</sub>NiFeCr alloys, one can discern that changing in Cu concentration does not have a significant influence on the magnetic moment of solutes in the alloys.

## 5.5 Monovacancy and self-interstitial in CuNi, CuNiFe, CuNiFeCr and Cu<sub>0.3</sub>NiFeCr alloys

In order to further explore and discuss the radiation resistance of Cu-containing solid solution concentrated alloys, the behavior of defects in CuNi, CuNiFe, CuNiFeCr and Cu<sub>0.3</sub>NiFeCr alloys deserve to be investigated. The monovacancy and self-interstitial are the elementary defects that could be generated under irradiation. There may be two approaches to achieve high radiation resistance. One is that high-entropy alloys are more difficult to generate point defects than traditional metals to improve radiation resistance. The other is that the evolution after defects formation is more difficult in high-entropy alloys, such as dislocations that are difficult to move. Theoretical calculations have been reported to reveal the defect energies in a series of equiatomic concentrated solid solution alloys [118]. They found that the formation energies of the interstitials in the NiCoCr and NiCoFeCr alloys are smaller than those of the pure Ni, although the formation energies of the vacancies are higher. In addition, there is a wide overlap between the migration barrier of interstitials and vacancies in the NiCoCr and NiCoFeCr alloys. These findings indicate possible enhanced interactions between interstitials and vacancies in (concentrated solid solution alloys) CSAs, which may promote recombination and annihilation of the defect. But this study did not statistics the interstitial and vacancy formation energy of each kind of atom separately.

In this work, it is speculated that different elements may have different effects on energy, especially copper. Compared with other elements, as is discussed in Chapter 5.4, Cu has one of the biggest characteristics that Cu always exhibits paramagnetism. Therefore, We calculated the defect energy  $E_i^f$  and the vacancy formation energy  $E_v^f$  of Cu and Ni atoms in these alloys respectively. The defect energy (the interstitial formation energies  $E_i^f$ ) of Cu and Ni atoms in CuNi, CuNiFe, CuNiFeCr and Cu<sub>0.3</sub>NiFeCr alloys are shown in Fig 5.5. It can be seen that the

defect energy  $E_i^f$  of Cu and Ni atoms in the high-entropy alloy is smaller than that of the binary and ternary alloy. Therefore, it can be inferred that only an increase in composition would not definitely make the formation of interstitial defects difficult. It may also be easier to form such defects. The vacancy formation energy  $E_v^f$  for Cu and Ni atomic positions in CuNi, CuNiFe, CuNiFeCr and Cu<sub>0.3</sub>NiFeCr alloys are shown in Fig 5.6. The vacancy formation energy  $E_v^f$  of the Cu position seems to be not very sensitive to the number of components, and there is no obvious change. However, as the number of components increases, the vacancy formation energy  $E_v^f$  of Ni positions increases. This supports the original assumption, to some degree, that different elements do have different energy effects. Therefore it can be inferred that the selection of elements should not be random in the development of high entropy alloys and that not all elements can be affected by the entropy value, thus improving the resistance to radiation.

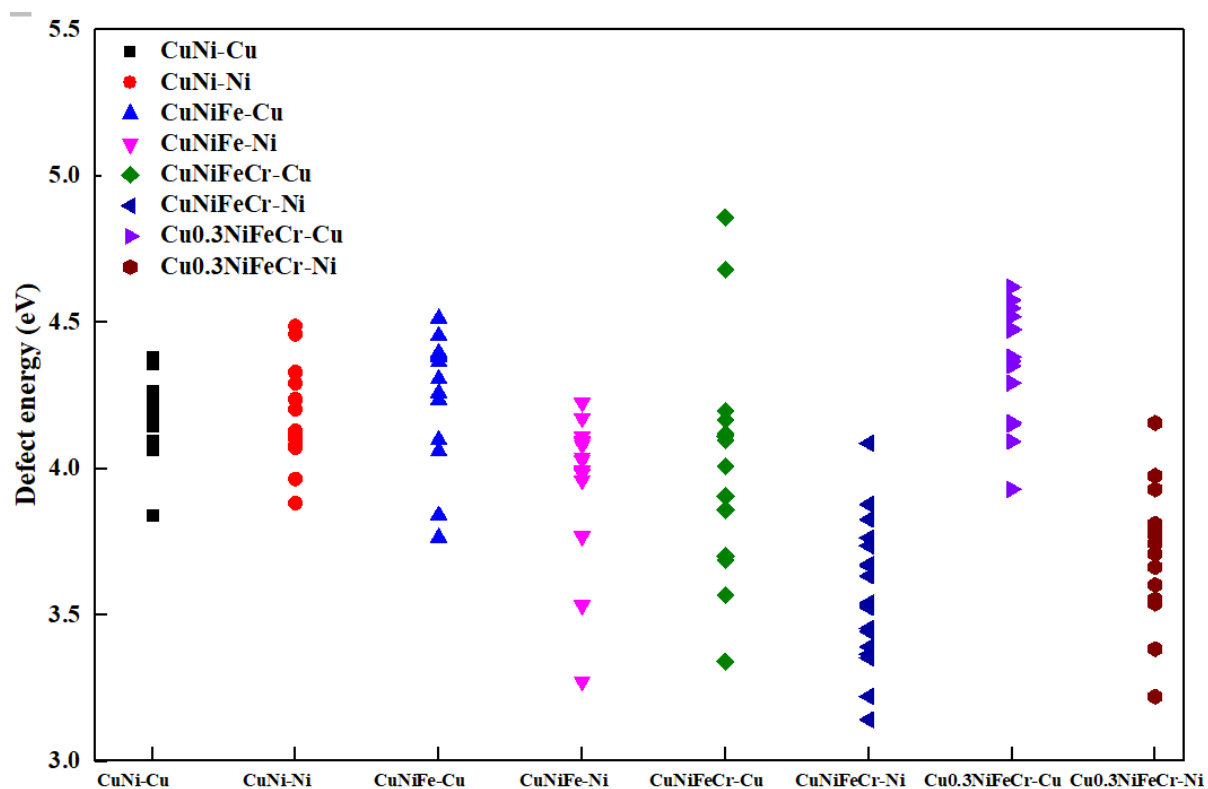


**Figure 5.5** The defect energy of Cu and Ni atoms in CuNi, CuNiFe, CuNiFeCr and Cu<sub>0.3</sub>NiFeCr alloys.

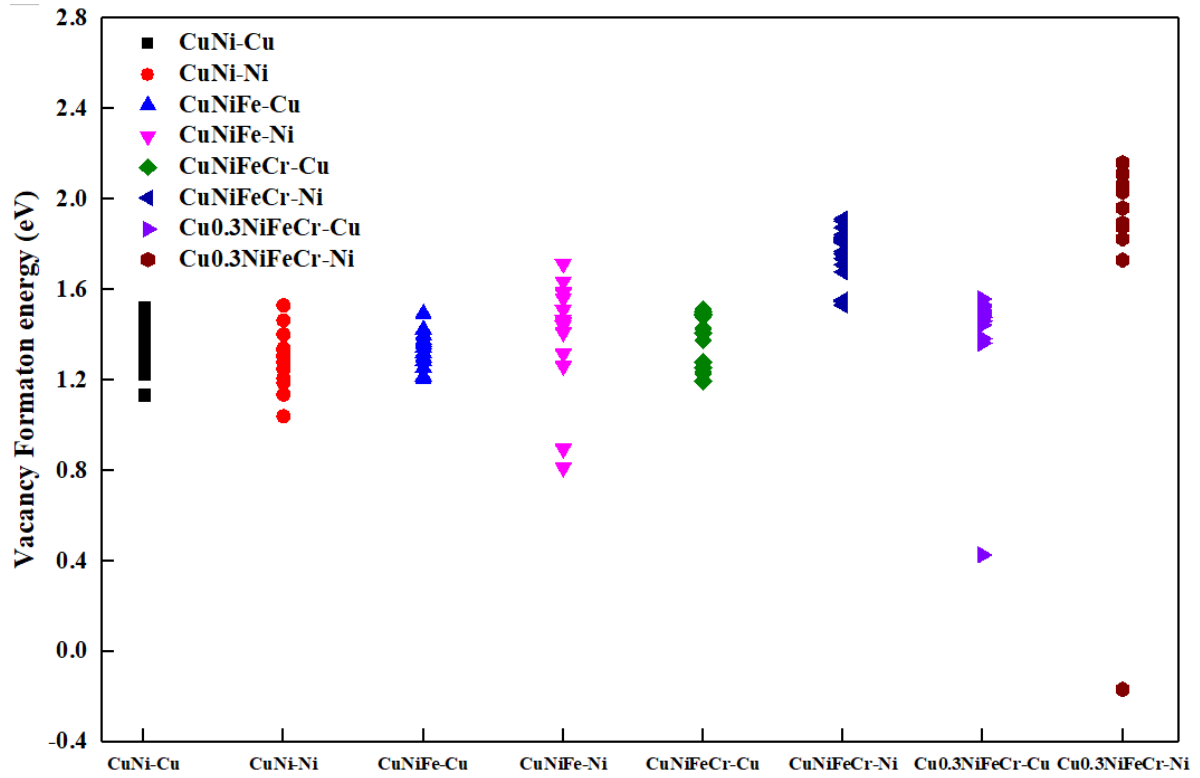


Figure 5.6 The vacancy formation energy for Cu and Ni atomic positions in CuNi, CuNiFe, CuNiFeCr and Cu<sub>0.3</sub>NiFeCr alloys.

## 5.6 Physical properties of CrCoFeNi HEA

To achieve a large number of possible arrangements of HEAs, 6 random solid solutions of CrCoFeNi are created with SQS method. At first, the lattice constant of each CrCoFeNi HEA is checked. Results are shown in Table 5.2. The lattice constant of CrCoFeNi HEA is calculated to be 3.51 Å in average, which is in good agreement with the former report [110,115]. It is smaller than the experimental value [110], but the difference is only about 1%.

**Table 5.2** The calculated lattice constant of CrCoFeNi HEA in comparison with the previous studies.

	Lattice constant (Å)
This work	Average 3.51 Å
Previous theoretical calculation	3.54 Å <sup>22</sup> 3.51 Å <sup>23</sup>
Previous experiment	3.57 Å <sup>22</sup>

The magnetic property of CrCoFeNi HEA is calculated to be ferromagnetic, which is the same as in previous reports [115]. The magnetic moment of each solute is shown in Fig 5.7(a). It can be seen that Fe, Co and Ni produce magnetic moment in the same direction with 1.87  $\mu$ , 0.95  $\mu$  and 0.26  $\mu$  in average, respectively. While the average magnetic moment of Cr is  $-0.66 \mu$ . Most Cr atoms in CrCoFeNi HEA show the opposite magnetic moment against Fe, Co and Ni, but still, some Cr atoms produce the magnetic moment in the same direction as Fe, Co and Ni. Moreover, it is notable that all these four solutes show a variety in magnetic moment value. The variation in the magnetic moment of Cr is large, while the variation in the magnetic moment of Ni is small.

Furthermore, the charge transfers of each solute in CrCoFeNi HEA are analyzed, as presented in Fig 5.7(b). Clearly, in all the cases, Ni atoms have electrons positive charges and Cr atoms have negative charges. For Co atoms, in most cases they have positive charges, but a few Co atoms have negative charges. For Fe atoms, half of them have positive charges and another half have negative charges. This means that within CrCoFeNi HEA, Cr atoms play as the main electron donor, Ni atoms play as the main electron acceptor. For Co and Fe atoms, they can be electron donor or electron acceptor, which depends on the local configuration surround them.

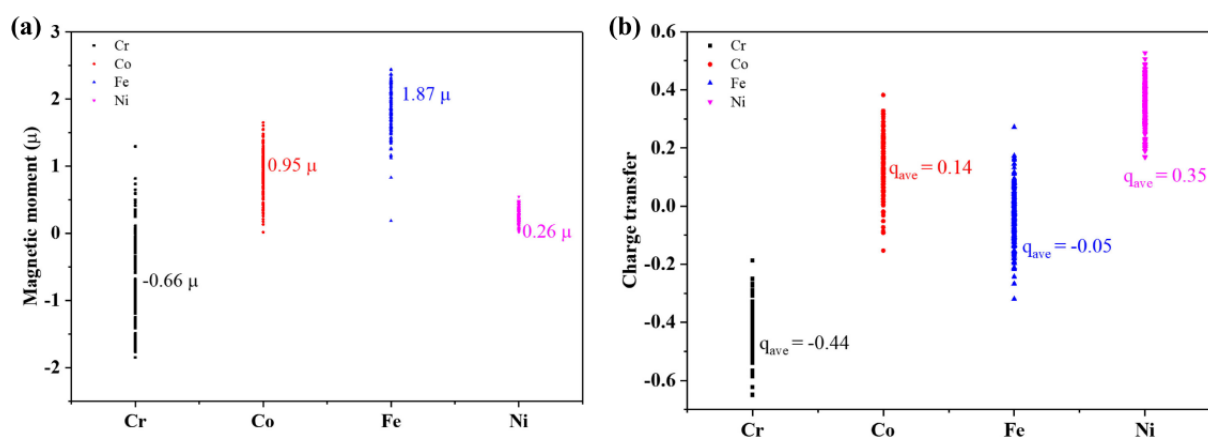


**Figure 5.7** The magnetic moment (a) and charge transfer (b) of each solute in CrCoFeNi HEA

## 5.7 Dissolution of H, He, C and N in CrCoFeNi HEA

The dissolution behavior of H, He, C and N in CrCoFeNi HEA is studied. As first, the site preference of H, He, C and N is investigated by calculating the dissolution energy ( $E_{\text{dis}}$ ) of these interstitials at tetrahedral site (T site) and octahedral site (O site) in CrCoFeNi HEA, respectively. Considering that  $E_{\text{dis}}$  may be different from site to site in CrCoFeNi HEA, 3 tetrahedral sites and 3 octahedral sites for each interstitial are considered to obtain the  $E_{\text{dis}}$ .

The  $E_{\text{dis}}$  is calculated by the following formula:

$$E_{\text{dis}} = E_{\text{tol}} - E_{\text{HEA}} - E_{\text{Inter}} \quad (5.1)$$

Where  $E_{\text{tol}}$  is the total energy of the CrCoFeNi HEA with interstitial atom,  $E_{\text{HEA}}$  is the energy of the CrCoFeNi HEA without interstitial atom, and  $E_{\text{Inter}}$  is the energy of the interstitial atom. For H and N, to take chemical potential of them into consideration,  $E_{\text{Inter}}$  is calculated as half energy of one  $\text{H}_2$  molecule and one  $\text{N}_2$  molecule, respectively. For C,  $E_{\text{Inter}}$  is the energy of one C atom in graphite.

Calculated average  $E_{\text{dis}}$  of H, He, C and N in CrCoFeNi HEA are presented in Table 5.3. Results show that H, C and N atom at O site have lower  $E_{\text{dis}}$  compared with they are at T site, indicating they are more stable at O site rather than T site. However, He is more stable at T site with lower  $E_{\text{dis}}$  compared with O site. The result is similar to the case of H, He, C and N in Ni and fcc Fe as reported before [119,120].

**Table 5.3** The calculated average dissolution energy (eV) of H, He, C and N at T site and O site in CrCoFeNi HEA.

	H	He	C	N
T site	0.50±0.06	4.71±0.04	3.26±0.07	2.10±0.10
O site	0.10±0.03	4.94±0.05	0.71±0.06	0.39±0.04

In further study, to systematically investigate the dissolution behavior of H, He, C and N, they are put at the different sites in CrCoFeNi HEA, and the  $E_{\text{dis}}$  is calculated. For each interstitial, 24 different interstitial sites are considered. According to the previous results, in these calculations, the occupation site of H, C and N is considered to be O site, while the occupation site preference of He is considered to be T site. Figure 5.8 shows the  $E_{\text{dis}}$  of H, He, C and N at 24 different interstitial sites. It can be seen that H has the lowest average  $E_{\text{dis}}$ , while He has the highest average  $E_{\text{dis}}$ . Although the atom radius of C and N is much larger than it of He, the  $E_{\text{dis}}$  of C and N is below it of He. It is noticeable that N has a lower  $E_{\text{dis}}$  than C in CrCoFeNi HEA. Former researches also show that N has a lower  $E_{\text{dis}}$  than C in Ni and bcc Fe [121-124].



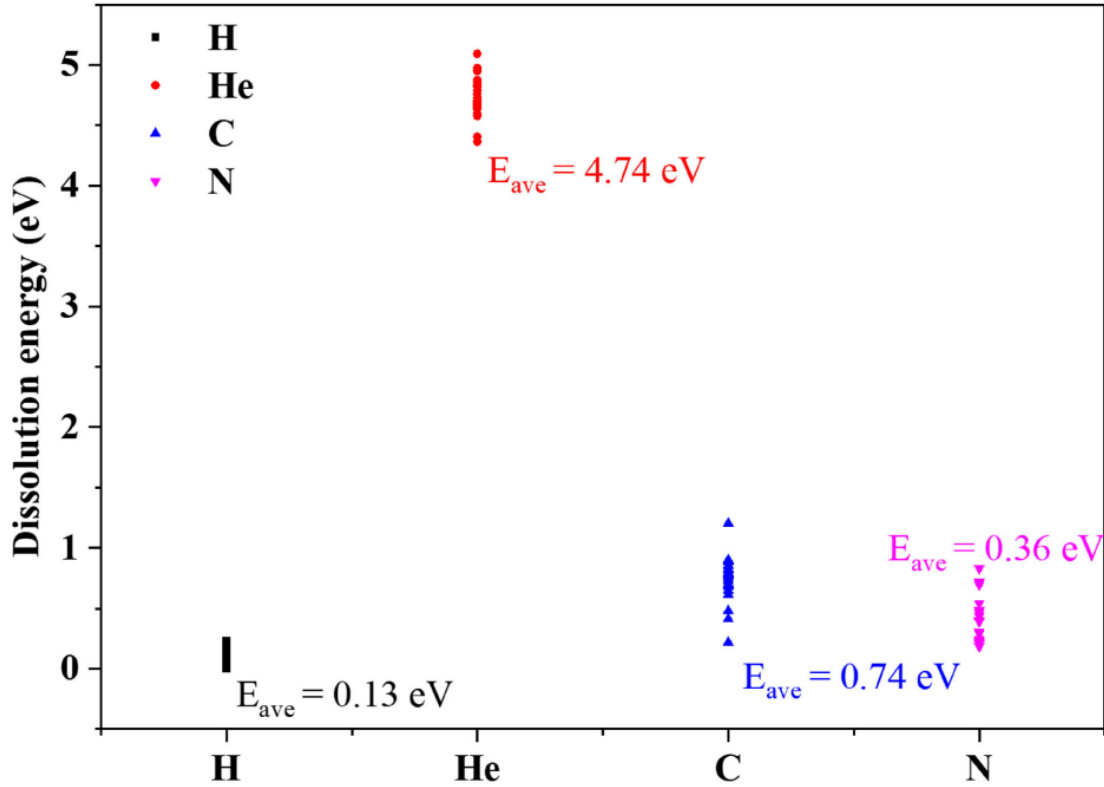


Figure 5.8 The dissolution energy of H, He, C and N in CrCoFeNi HEA.

Furthermore, it can be seen that the  $E_{dis}$  H, He, C and N shows different variety. The variation in  $E_{dis}$  of H is small. However, the variation in  $E_{dis}$  of He, C and N is quite large. It implies that the dissolution behavior of H at different sites is similar, while the dissolution behavior of He, C and N may strongly depend on the local configuration, for example, the distribution of solute (Cr, Co, Fe and Ni) atoms.

To investigate the relation between the dissolution behavior of interstitial atom and the local distribution of solute (Cr, Co, Fe and Ni) atoms. For each interstitial, 5 configurations with high  $E_{dis}$  of interstitial and 5 configurations with low  $E_{dis}$  of interstitial are picked, then the number of solute atoms located at the first coordination shell of the interstitial atom (nearest-neighbor, or NN) are counted. Results are shown in Figure 5.9. Apparently, H, He and N has low  $E_{dis}$  at the site with more Cr atoms as shown in Figure 5.9(a) (b) and (d), indicating that H, He and N

are more stable at the site with high Cr concentration. However, it seems C has low  $E_{\text{dis}}$  at the site with less Ni atoms (Figure 5.9(c)). The result suggests that an attractive interaction may exist between Cr and H, He, N interstitials. The attractive interaction between Cr and interstitial is considered to be due to the reactive chemical property of Cr. The DFT calculation data of Cr related compounds in Materials Project database [125] is investigated. The formation energy of Cr related compounds,  $\text{Cr}_3\text{C}_2$ ,  $\text{CrH}_2$  and  $\text{Cr}_3\text{N}_2$ , always has a negative value, while the formation energy of Co, Fe, Ni related compounds, such as  $\text{Fe}_3\text{C}$ ,  $\text{Co}_2\text{C}$  and  $\text{NiC}$ , has a positive value. It means that Cr containing compounds can be easily formed, which also reveals the high attraction effect of Cr to H, C and N. The attractive interaction between Cr and interstitial was also reported in previous study [120,126]. However, in this work, no obvious attraction between C and Cr is found. Instead, it seems there is a strong repulsive interaction between C and Ni. After investigating the formation energy of Ni related compounds, it is found that the formation energy of Ni-C compounds is very high. For example, the formation energy of  $\text{NiC}$  is very high with 1.10 eV, while the formation energy of  $\text{Fe}_3\text{C}$  is only 0.053 eV. It reveals that the repulsion effect of Ni to C is strong. Also, previous study reported that there is repulsive interaction between C and Ni [127].

Moreover, to get a more complete understanding on the interaction between interstitial and solutes, the bond length of interstitial-solute is investigated, as shown in Figure 5.9(e). The bond length of C-solute and N-solute are longer than that of H-solute and He-solute, which is considered to be due to the large size of C and N. It is found that the bond length of He-solute is the shortest, which may be mainly due to He occupies T site but other interstitials occupy O site. The bond length of H-solute, C-solute and N-solute show a similar tendency. Bond with Co has a shorter length, while bond with Cr has a longer length. However, for He, He-Cr bond has the shortest length, while He-Ni bond has the longest length. It implies that the nature of

the interaction between H, C, N and the solutes may be very different from the interaction between He and the solutes.

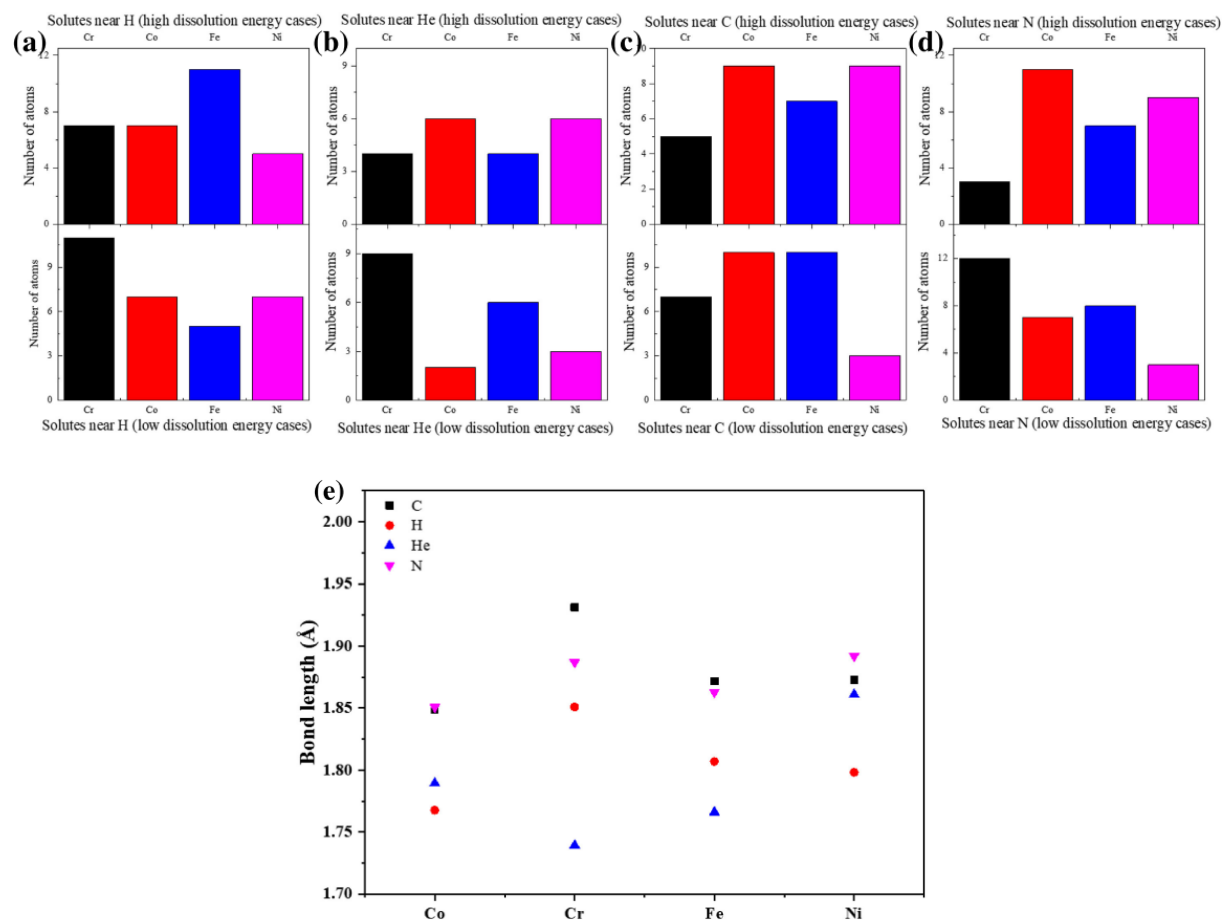


**Figure 5.9** The number of solutes (Cr, Co, Fe and Ni) located at the first coordination shell of H (a), He (b), C (c) and He (d), and the average bond length between interstitial atoms and solutes (e)

## 5.8 Effect of H, He, C and N on the physical properties of CrCoFeNi HEA

The effect of H, He, C and N on the magnetic properties of solutes in CrCoFeNi HEA are investigated. The magnetic moment of Cr, Co, Fe and Ni located at the first coordination shell of the interstitial atoms (nearest-neighbor, or NN) is presented in Figure 5.10. Although different interstitial atom shows the different effect on magnetic properties of solutes, all of them have the effect of decreasing magnetic moment of Cr, Co, Fe and Ni. Among Cr, Co, Fe and Ni, Fe is the element which is the most affected by interstitial, an obvious decreasing in magnetic moment is observed in Figure 5.10(a). While Ni is the least affected one, the decreasing in magnetic moment of Ni near interstitial is within  $0.1 \mu_B$  in average as shown in Figure 5.10(d). Compared with C and N, the effect of H and He on the magnetic moment of elements in CrCoFeNi HEA is weak. It is considered that the magnetic properties of atoms are strongly related to the charge transfer between atoms since it results in the changing in the unpaired spins of atoms. So the charge transfer of H, He, C and N are investigated as shown in Figure 5.10(e). It can be seen that due to the closed-shell structure of He, the electron transferred to He is very limited, only 0.16 electrons in average. It indicates only weak interaction exists between He and the elements in CrCoFeNi HEA. And, consequently, He has little influences on the magnetic properties of solutes. Compared with He, electrons transferred to H is 0.37 electrons in average, which is also low but higher than the cases of He. Therefore, H has a stronger influence on the magnetic moment than He. Electrons transferred to C and N is much higher with 1.04 electrons and 1.14 electrons in average, respectively. It results in the strong effect of C and N on decreasing the magnetic moment of Cr, Co, Fe and Ni.

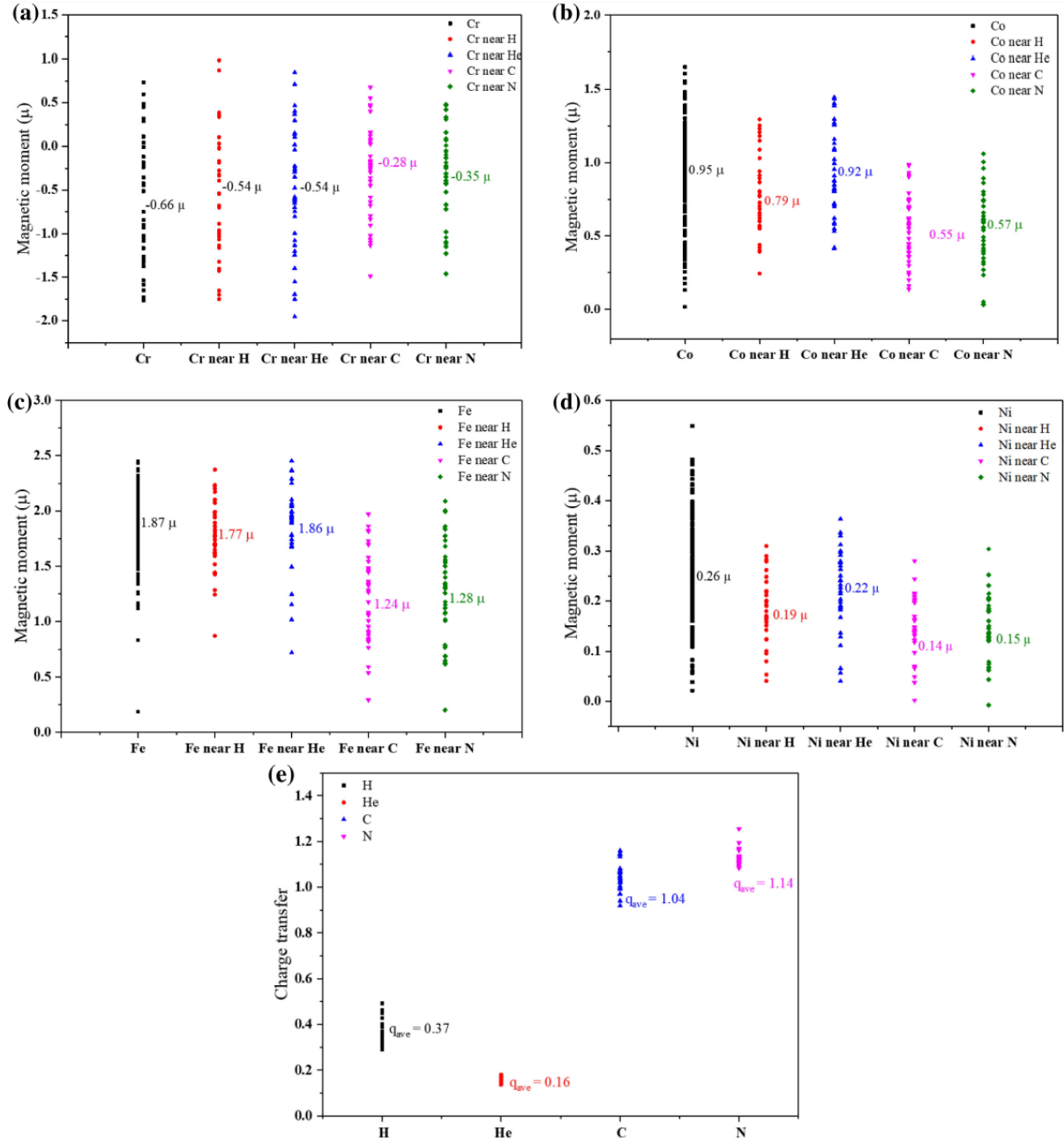


**Figure 5.10** The magnetic moment of Cr (a), Co (b), Fe (c) and Ni (d) next to interstitial in CrCoFeNi HEA and the charge transfer of interstitial atoms (e)

Last, the electronic structures of HEA with H, He, C and N are investigated. Figure 5.11 shows the projected density of states (PDOS) of the solutes and the interstitial in HEA. The dot line in Figure 5.11 represents the Fermi level. Figure 5.11(a) shows the PDOS of Cr, Co, Fe and Ni of d-state in HEA without interstitial. The calculated PDOS of Cr, Co, Fe and Ni agree with the

former report [128], the major peaks in the PDOS are located above the Fermi level for Cr and below the Fermi level for Co, Fe and Ni. It proves that Cr is more chemically reactive than the other three solutes in CrCoFeNi HEA.

In Figure 5.11(b), it can be seen that at the position of  $-9$  eV, the PDOS of H overlapped with the PDOS of Cr, Co, Fe and Ni which are nearest-neighbor of H, indicating H does slightly interact with Cr, Co, Fe and Ni. This weak interaction is also shown in charge transfer since only 0.37 electrons transferred to H in average. The PDOS of He doesn't overlap with any solutes as shown in Figure 5.11 (c). It means no chemical interaction between He and Cr, Co, Fe and Ni, which is mainly due to the closed-shell structure of He. Compared with H and He, the interaction between C, N and Cr, Co, Fe and Ni is much stronger. Figure 5.11(d) and (e) show that strong hybridization between C, N and Cr, Co, Fe and Ni exists. Moreover, the PDOS of N overlaps with PDOS of Cr, Co, Fe and Ni in the broader region than the PDOS of C, indicating the interaction between N and Cr, Co, Fe and Ni is slightly stronger than the interaction between C and Cr, Co, Fe and Ni.

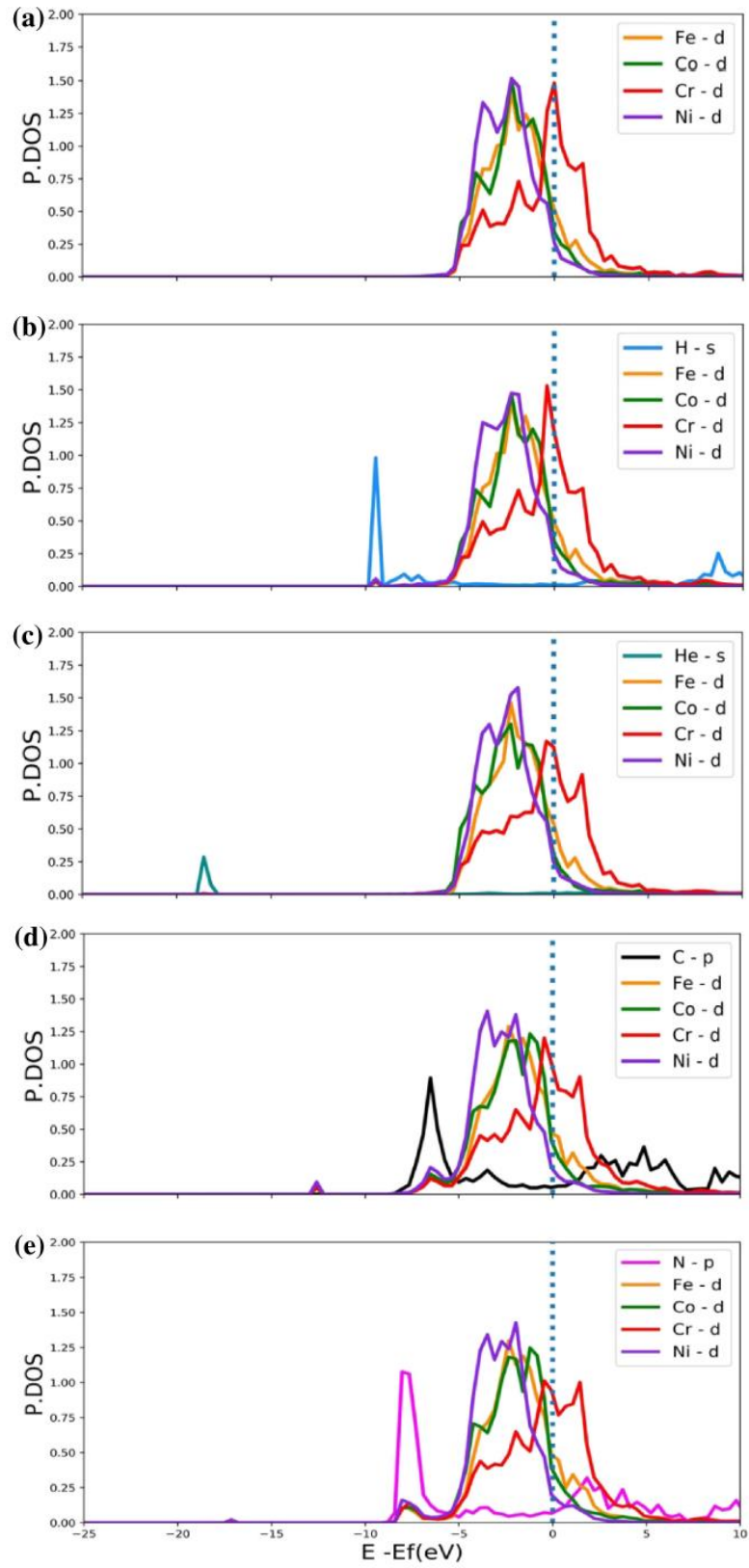


**Figure 5.11** The projected density of states of Cr, Co, Fe and Ni of d-state in HEA without interstitial (a), s-state of H (b) and He (c), p-state of C (d) and N (e), and the nearest Cr, Co, Fe and Ni of d-state.

## 5.9 Summary

In this chapter, first-principles DFT calculations have been performed to investigate the properties and formation energies of point defects (The monovacancy and self-interstitial) in the face-centered cubic Co-free alloys, CuNi, CuNiFe, CuNiFeCr, and Cu<sub>0.3</sub>NiFeCr. The consistency of the results of the XRD measurements and the first estimates proves the validity of the calculation. Calculated coherent energy and formation enthalpy for CuNi, CuNi, CuNiFeCr, and Cu<sub>0.3</sub>NiFeCr alloys suggest that the face-centred Co-free alloys we have produced are stable alloys. And the largest structural corrugation in equimolar HEA (CuNiFeCr) indicates that higher entropy is the stronger local structural disorder. Also, the calculated defect energy (interstitial formation energy  $E_i^f$ ) and the vacancy formation energy  $E_v^f$  of Cu and Ni atoms in these alloys show the different elements may have different effects on energy, which can also be implied that the selection of elements should not be arbitrary in the creation of a high entropy alloy and that not all elements may be influenced by the value of the entropy, thereby improving resistance to radiation. In addition, the dissolution behavior of H, He, C and N in CrCoFeNi high entropy alloys (HEAs) is studied with density functional theory calculation method. The site preference of H, C and N in CrCoFeNi HEAs is the octahedral site, while the site preference of He is the tetrahedral site. The dissolution energy of H is the lowest and it of He is the highest. The high dissolution energy of He is considered to be due to the closed-shell electronic structure of He. Moreover, H, He and N is found to be more stable at the position with more Cr atoms, while C is found to be more stable at the position with less Ni atoms. Furthermore, the effect of H, He, C and N on the physical properties of CrCoFeNi HEAs is studied. H, He, C and N have the effect of decreasing the magnetic moments of solutes in CrCoFeNi HEAs. Electronic structures analysis shows that, for C and N, there is hybridization between C, N and solutes. It implies the chemical bonding between C, N and solutes is strong.



# Chapter 6

---

## Conclusions

---

High entropy alloys have aroused the greatest interest due to their peculiar criteria of composition, and hence the wide realm of compositions. However, this very recent and young definition also lacks evidence on the effect of multiplication elements on microstructure and properties, mainly on their radiation behaviour. Currently, the basic development of such alloys starts with the formation of a stable single phase of the equimolar or near-equimolar mixing of elements. I got the chance to take this first step in creating a new branch of high entropy alloys. Those considerations led to open through my study the development of face-centred cubic Co-free solid solution high entropy alloys, and trying new compositions to get fresh new results.

The work presented in Chapter 3 was performed on five Co-free Cu-containing solid solution concentrated alloys, Cu, CuNi, CuNiFe, Cu<sub>0.3</sub>NiFeCr, Al<sub>0.4</sub>CuFeCrNi<sub>2</sub>. CuNi and CuNiFe alloys of the equal molar ratio were prepared by arc-melting, and Cu<sub>0.3</sub>NiFeCr and Al<sub>0.4</sub>CuFeCrNi<sub>2</sub> alloys were prepared by induction furnace in a high purity argon atmosphere. All the as-cast alloys were identified as single-phase FCC alloys by X-ray diffraction analysis. Solution-annealed CuNi, CuFeNi, Cu<sub>0.3</sub>NiFeCr, and Al<sub>0.4</sub>CuFeCrNi<sub>2</sub> alloys showed single-phase FCC structures with the homogeneous atomic distribution under the scanning electron microscope (SEM, JSM-6510LA) equipped with an energy dispersive spectrometer (EDS). Mechanical property examinations for all five Co-free Cu-containing solid solution concentrated alloys are the main focus of Chapter 3. Due to the general solid solution hardening effect, the hardness and strength seemed to increase with increasing the number of elements. The order of the Vickers hardness and the Tensile strength was Cu < CuNi < CuNiFe < Cu<sub>0.3</sub>NiFeCr < Al<sub>0.4</sub>CuFeCrNi<sub>2</sub>. Mechanical property examinations indicated the highest Vickers hardness, the highest Tensile strength, and the smallest elongation in the Al<sub>0.4</sub>CuFeCrNi<sub>2</sub> alloy. The results indicate that the Al<sub>0.4</sub>CuFeCrNi<sub>2</sub> alloy would have the potential to be a Co-free high-entropy alloy applicable to nuclear reactor components.

In Chapter 4, the evolution of ion damage at 500°C in high purity face-centered cubic Co-free Cu-containing solid solution concentrated alloys, CuNi, Cu<sub>0.3</sub>NiFeCr, Al<sub>0.4</sub>CuFeCrNi<sub>2</sub> without apparent preexisting defect sinks are explored. The irradiation-induced microstructure has been investigated using transmission electron microscopy. The irradiation effects were assessed through the measurement of the defect type, defect density and defect size. The irradiation damage resulted in a high density of defects in all three materials. CuNi, Cu<sub>0.3</sub>NiFeCr alloys but Al<sub>0.4</sub>CuFeCrNi<sub>2</sub> present stacking fault tetrahedra (SFTs). The irradiation introduced a high density of SFTs in CuNi alloy. The high entropy alloy (Al<sub>0.4</sub>CuFeCrNi<sub>2</sub>) had the smallest loop size (the highest density), followed by Cu<sub>0.3</sub>NiFeCr and then CuNi. The loop density was dependent on the alloy composition. The alloy composition influences the type of defect. At 1 dpa, the order of maximum loop size was Al<sub>0.4</sub>CuFeCrNi<sub>2</sub> < Cu<sub>0.3</sub>NiFeCr < CuNi. The order of loop density was CuNi < Cu<sub>0.3</sub>NiFeCr < Al<sub>0.4</sub>CuFeCrNi<sub>2</sub>. Orowan equation was used to measure the irradiation hardening contributed by SFTs, black dots and loops. The calculated hardening results indicate that the irradiation hardening at 500°C was less in HEA (Al<sub>0.4</sub>CuFeCrNi<sub>2</sub>) and Cu<sub>0.3</sub>NiFeCr than in CuNi and 316H SS. The lowest calculated irradiation hardening in high entropy alloy (Al<sub>0.4</sub>CuFeCrNi<sub>2</sub>) suggested the possibility for the nuclear application of Co-free high-entropy alloy at 500°C.

Although the high entropy alloy (Al<sub>0.4</sub>CuFeCrNi<sub>2</sub>) exhibited higher strength than CuCrZr alloy and 316H SS, the lower elongation still makes it difficult to be applied. Therefore, the detailed analysis of the fracture surface and the optimization of annealing condition would be needed to improve the ultimate elongation of Al<sub>0.4</sub>CuFeCrNi<sub>2</sub>. Also, adjusting the composition of aluminum in Al<sub>0.4</sub>CuFeCrNi<sub>2</sub> alloy can be considered to optimize alloy mechanical properties. Besides, although the calculated hardening results show the irradiation hardening at 500°C was

the lowest in HEA ( $\text{Al}_{0.4}\text{CuFeCrNi}_2$ ). Due to the parameters of the hardening model (e.g.  $\alpha$  and  $K$ ), errors will exist between the outcomes measured and the experimental results. Measurements of nanoindentations will then be required to determine the precision of the predicted effects. Furthermore, since this research aims to study Cu-containing high entropy alloys for nuclear fusion applications, higher radiation doses and higher temperature radiation experiments also need to be conducted to evaluate the radiation resistance of those Co-free Cu-containing solid solution concentrated alloys.

In Chapter 5, properties of the face-centered cubic Co-free alloys CuNi, CuNiFe, CuNiFeCr, and  $\text{Cu}_{0.3}\text{NiFeCr}$  are studied through density functional theory calculation. And the vacancy formation energy  $E_v^f$  and interstitial formation energy  $E_i^f$  of Cu and Ni elements in alloys are regarded. The consistency of the results of the XRD measurements and the first estimates proves the validity of the calculation. Calculated coherent energy and formation enthalpy for CuNi, CuNi, CuNiFeCr, and  $\text{Cu}_{0.3}\text{NiFeCr}$  alloys CuNi alloys suggest that the face-centred Co-free alloys we have produced are stable alloys. Local structural disorder of the HEAs was traced by the calculation of structural corrugation within the HEAs, which clear that with increases in component, the structural corrugation in different plane increases. And the outcomes of structural corrugation in equimolar HEA (CuNiFeCr) are more severe than in non-equimolar HEA ( $\text{Cu}_{0.3}\text{NiFeCr}$ ) indicates that higher entropy is the stronger local structural disorder. Also, the defect energy (interstitial formation energy  $E_i^f$ ) and the vacancy formation energy  $E_v^f$  of Cu and Ni atoms in these alloys are calculated. It is found that element selection in high-entropy alloys has a significant impact on the defect energetics. The defect energy  $E_i^f$  of Cu and Ni atoms in the high-entropy alloy is lower than that of the binary and ternary alloy, whereas the vacancy formation energy  $E_v^f$  of Ni positions in the high-entropy alloy is higher. However, the vacancy energy of the Cu position does not appear to be very sensitive to the number of

components, and there is no apparent change. This may be because Cu always exhibits paramagnetism. These results suggest different elements do have different effects on energy, which can also be implied that the choice of elements should not be random in the development of a high entropy alloy and that not all elements can be influenced by the value of the entropy, thereby improving resistance to radiation. In addition, the dissolution behavior of H, He, C and N in CrCoFeNi high entropy alloys (HEAs) is studied with density functional theory calculation method. The site preference of H, C and N in CrCoFeNi HEAs is the octahedral site, while the site preference of He is the tetrahedral site. The dissolution energy of H is the lowest and it of He is the highest. The high dissolution energy of He is considered to be due to the closed-shell electronic structure of He. Moreover, H, He and N is found to be more stable at the position with more Cr atoms, while C is found to be more stable at the position with less Ni atoms. Furthermore, the effect of H, He, C and N on the physical properties of CrCoFeNi HEAs is studied. H, He, C and N have the effect of decreasing the magnetic moments of solutes in CrCoFeNi HEAs. Electronic structures analysis shows that, for C and N, there is hybridization between C, N and solutes. It implies the chemical bonding between C, N and solutes is strong.

## References

1. Chepeliev M, van der Mensbrugghe D. Global fossil-fuel subsidy reform and Paris Agreement. *Energy Economics*. 2020 2020/01/01/;85:104598.
2. Soutter ARB, Möttus R. “Global warming” versus “climate change”: A replication on the association between political self-identification, question wording, and environmental beliefs. *Journal of Environmental Psychology*. 2020 2020/06/01/;69:101413.
3. 95/04751 Nuclear power reactors in the world. *Fuel and Energy Abstracts*. 1995 1995/09/01/;36(5):340.
4. A Technology Roadmap for Generation IV Nuclear Energy Systems Executive Summary. United States 2003.
5. Allen T, Busby J, Meyer M, et al. Materials challenges for nuclear systems. *Materials Today*. 2010 2010/12/01/;13(12):14-23.
6. Shi S, Bei H, Robertson IM. Impact of alloy composition on one-dimensional glide of small dislocation loops in concentrated solid solution alloys. *Materials Science and Engineering: A*. 2017;700:617-621.
7. Shi S, He M-R, Jin K, et al. Evolution of ion damage at 773K in Ni-containing concentrated solid-solution alloys. *Journal of Nuclear Materials*. 2018;501:132-142.
8. Naslain R. Design, Preparation and Properties of Non-Oxide CMCs for Application in Engines and Nuclear Reactor: An Overview. *Composites Science and Technology*. 2004 02/01/;64:155-170.
9. Duan Z, Yang H, Satoh Y, et al. Current status of materials development of nuclear fuel cladding tubes for light water reactors. *Nuclear Engineering and Design*. 2017 2017/05/01/;316:131-150.
10. Non-ferrous metals. *Materials and Corrosion*. 1992 1992/08/01/;43(8):R160-R167.
11. Bever MB. *Encyclopedia of materials science and engineering*. United States: Pergamon Press; 1985.
12. Smith CO. MATERIALS DEVELOPMENT WITH REFERENCE TO NUCLEAR REACTORS. *Naval Engineers Journal*. 1967 1967/08/01/;79(4):563-567.

13. Ursu I. Physics and technology of nuclear materials. United Kingdom: Pergamon Press; 1985.
14. Yvon P, Carré F. Structural Materials Challenges for Advanced Reactor Systems. *Journal of Nuclear Materials*. 2009 03/01;385:217-222.
15. Little EA, Bullough R, Wood MH. On the Swelling Resistance of Ferritic Steel. *Proceedings of the Royal Society of London Series A, Mathematical and Physical Sciences*. 1980;372(1751):565-579.
16. Abe F. Precipitate design for creep strengthening of 9% Cr tempered martensitic steel for ultra-supercritical power plants. *Sci Technol Adv Mater*. 2008;9(1):013002-013002.
17. Wakai E, Okubo N, Ando M, et al. Reduction method of DBTT shift due to irradiation for reduced-activation ferritic/martensitic steels. *Journal of Nuclear Materials*. 2010 2010/03/01;398(1):64-67.
18. Noh S, Ando M, Tanigawa H, et al. Friction stir welding of F82H steel for fusion applications. *Journal of Nuclear Materials*. 2016 2016/09/01;478:1-6.
19. Yeh JW, Chen SK, Lin SJ, et al. Nanostructured high - entropy alloys with multiple principal elements: novel alloy design concepts and outcomes. *Advanced Engineering Materials*. 2004;6(5):299-303.
20. Hsu C-Y, Yeh J-W, Chen S-K, et al. Wear resistance and high-temperature compression strength of Fcc CuCoNiCrAl<sub>0.5</sub>Fe alloy with boron addition. *Metallurgical and Materials Transactions A*. 2004 2004/05/01;35(5):1465-1469.
21. Huang PK, Yeh JW, Shun TT, et al. Multi-Principal-Element Alloys with Improved Oxidation and Wear Resistance for Thermal Spray Coating. *Advanced Engineering Materials*. 2004 2004/02/05;6(1 - 2):74-78.
22. Yeh J-W, Lin S-J, Chin T-S, et al. Formation of simple crystal structures in Cu-Co-Ni-Cr-Al-Fe-Ti-V alloys with multiprincipal metallic elements. *Metallurgical and Materials Transactions A*. 2004 2004/08/01;35(8):2533-2536.
23. Murty BS, Yeh J-W, Ranganathan S, et al. High-entropy alloys. Elsevier; 2019.
24. Gao MC. Progress in High-Entropy Alloys. *JOM*. 2014 2014/10/01;66(10):1964-1965.

25. Zhang Y, Zuo TT, Tang Z, et al. Microstructures and properties of high-entropy alloys. *Progress in Materials Science*. 2014 2014/04/01/;61:1-93.
26. Pickering EJ, Jones NG. High-entropy alloys: a critical assessment of their founding principles and future prospects. *International Materials Reviews*. 2016 2016/04/02;61(3):183-202.
27. Tsai M. (Review) Physical Properties of High Entropy Alloys. *Entropy*. 2013 12/01;15:2013.
28. Gao MC, Yeh J-W, Liaw PK, et al. High-entropy alloys. Cham: Springer International Publishing. 2016.
29. Yeh JW. Recent progress in high-entropy alloys. *Annales de Chimie Science des Materiaux (Paris)*. 2006;31(6):633-648.
30. Cantor B, Chang ITH, Knight P, et al. Microstructural development in equiatomic multicomponent alloys. *Materials Science and Engineering: A*. 2004 2004/07/01/;375-377:213-218.
31. Guo S, Ng C, Lu J, et al. Effect of valence electron concentration on stability of fcc or bcc phase in high entropy alloys. *Journal of Applied Physics*. 2011;109(10):103505.
32. Miracle DB, Senkov ON. A critical review of high entropy alloys and related concepts. *Acta Materialia*. 2017 2017/01/01/;122:448-511.
33. Gludovatz B, Hohenwarter A, Catoor D, et al. A fracture-resistant high-entropy alloy for cryogenic applications. *Science*. 2014;345(6201):1153-1158.
34. Gali A, George EP. Tensile properties of high- and medium-entropy alloys. *Intermetallics*. 2013 2013/08/01/;39:74-78.
35. Zaddach AJ, Scattergood RO, Koch CC. Tensile properties of low-stacking fault energy high-entropy alloys. *Materials Science and Engineering: A*. 2015 2015/06/11/;636:373-378.
36. Otto F, Dlouhý A, Somsen C, et al. The influences of temperature and microstructure on the tensile properties of a CoCrFeMnNi high-entropy alloy. *Acta Materialia*. 2013 2013/09/01/;61(15):5743-5755.



37. Wu Y, Liu W, Wang X, et al. In-situ neutron diffraction study of deformation behavior of a multi-component high-entropy alloy. *Applied Physics Letters*. 2014;104(5):051910.
38. Salishchev GA, Tikhonovsky MA, Shaysultanov DG, et al. Effect of Mn and V on structure and mechanical properties of high-entropy alloys based on CoCrFeNi system. *Journal of Alloys and Compounds*. 2014 2014/04/05/;591:11-21.
39. Schuh B, Mendez-Martin F, Völker B, et al. Mechanical properties, microstructure and thermal stability of a nanocrystalline CoCrFeMnNi high-entropy alloy after severe plastic deformation. *Acta Materialia*. 2015 2015/09/01/;96:258-268.
40. Stepanov N, Tikhonovsky M, Yurchenko N, et al. Effect of cryo-deformation on structure and properties of CoCrFeNiMn high-entropy alloy. *Intermetallics*. 2015 2015/04/01/;59:8-17.
41. Zinkle SJ, Snead LL. Designing Radiation Resistance in Materials for Fusion Energy. *Annual Review of Materials Research*. 2014;44(1):241-267.
42. Kumar NAPK, Li C, Leonard KJ, et al. Microstructural stability and mechanical behavior of FeNiMnCr high entropy alloy under ion irradiation. *Acta Materialia*. 2016 2016/07/01/;113:230-244.
43. Zhang Y, Stocks GM, Jin K, et al. Influence of chemical disorder on energy dissipation and defect evolution in concentrated solid solution alloys. *Nature Communications*. 2015 2015/10/28;6(1):8736.
44. Lu C, Niu L, Chen N, et al. Enhancing radiation tolerance by controlling defect mobility and migration pathways in multicomponent single-phase alloys. *Nat Commun*. 2016 Dec 15;7:13564.
45. Lu C, Niu L, Chen N, et al. Enhancing radiation tolerance by controlling defect mobility and migration pathways in multicomponent single-phase alloys. *Nature Communications*. 2016 2016/12/15;7(1):13564.
46. Chen W-Y, Kirk MA, Hashimoto N, et al. Irradiation effects on Al<sub>0.3</sub>CoCrFeNi and CoCrMnFeNi high-entropy alloys, and 316H stainless steel at 500 °C. *Journal of Nuclear Materials*. 2020 2020/10/01/;539:152324.

47. Beyramali Kivy M, Asle Zaeem M. Generalized stacking fault energies, ductilities, and twinnabilities of CoCrFeNi-based face-centered cubic high entropy alloys. *Scripta Materialia*. 2017 2017/10/01/;139:83-86.
48. Bleskov I, Hickel T, Neugebauer J, et al. Impact of local magnetism on stacking fault energies: A first-principles investigation for fcc iron. *Physical Review B*. 2016 06/29/;93(21):214115.
49. Gong P, Jin J, Deng L, et al. Room temperature nanoindentation creep behavior of TiZrHfBeCu(Ni) high entropy bulk metallic glasses. *Materials Science and Engineering: A*. 2017 2017/03/14/;688:174-179.
50. George E, Curtin WA, Tasan CC. High entropy alloys: A focused review of mechanical properties and deformation mechanisms. *Acta Materialia*. 2019:Medium: ED; Size: p. 435-474.
51. Enkovaara J, Rostgaard C, Mortensen JJ, et al. Electronic structure calculations with GPAW: a real-space implementation of the projector augmented-wave method. *J Phys Condens Matter*. 2010 Jun 30;22(25):253202.
52. Bonny G, Terentyev D, Pasianot RC, et al. Interatomic potential to study plasticity in stainless steels: the FeNiCr model alloy. *Modelling and Simulation in Materials Science and Engineering*. 2011 2011/11/03;19(8):085008.
53. Senkov ON, Wilks GB, Miracle DB, et al. Refractory high-entropy alloys. *Intermetallics*. 2010 2010/09/01/;18(9):1758-1765.
54. Shi S, He M-R, Jin K, et al. Evolution of ion damage at 773K in Ni- containing concentrated solid-solution alloys. *Journal of Nuclear Materials*. 2018 2018/04/01/;501:132-142.
55. Waszczuk P, Wieckowski A, Zelenay P, et al. Adsorption of CO poison on fuel cell nanoparticle electrodes from methanol solutions: a radioactive labeling study. *Journal of Electroanalytical Chemistry*. 2001 2001/09/21/;511(1):55-64.
56. Kim D, Jo A, Yang H-M, et al. Colorimetric detection and removal of radioactive Co ions using sodium alginate-based composite beads. *Journal of Hazardous Materials*. 2017 2017/03/15/;326:69-76.

57. Guo S, Ng C, Liu CT. Anomalous solidification microstructures in Co-free Al<sub>x</sub>CrCuFeNi<sub>2</sub> high-entropy alloys. *Journal of Alloys and Compounds*. 2013 2013/04/25/;557:77-81.
58. Goldstein JI, Newbury DE, Echlin P, et al. Scanning electron microscopy and X-ray microanalysis. A text for biologists, materials scientists, and geologists. New York, N.Y. 10013: Plenum Publishing Corporation; 1981. English.
59. Wang G, Fang N. Chapter four - Detecting and Tracking Nonfluorescent Nanoparticle Probes in Live Cells. In: conn PM, editor. *Methods in Enzymology*. Vol. 504: Academic Press; 2012. p. 83-108.
60. Williams DB, Carter CB. Weak-Beam Dark-Field Microscopy. In: Williams DB, Carter CB, editors. *Transmission Electron Microscopy: A Textbook for Materials Science*. Boston, MA: Springer US; 2009. p. 463-481.
61. Chang S-Y, Chen M-K. High thermal stability of AlCrTaTiZr nitride film as diffusion barrier for copper metallization. *Thin Solid Films*. 2009 2009/07/01/;517(17):4961-4965.
62. Chen T-K, Wong M-S. Thermal stability of hard transparent Al<sub>x</sub>CoCrCuFeNi oxide thin films. *Surface and Coatings Technology*. 2008 2008/12/25/;203(5):495-500.
63. Dolique V, Thomann AL, Brault P, et al. Thermal stability of AlCoCrCuFeNi high entropy alloy thin films studied by in-situ XRD analysis. *Surface and Coatings Technology*. 2010 2010/03/15/;204(12):1989-1992.
64. Huang C, Zhang Y, Shen J, et al. Thermal stability and oxidation resistance of laser clad TiVCrAlSi high entropy alloy coatings on Ti–6Al–4V alloy. *Surface and Coatings Technology*. 2011 2011/12/15/;206(6):1389-1395.
65. Huang Y-S, Chen L, Lui H-W, et al. Microstructure, hardness, resistivity and thermal stability of sputtered oxide films of AlCoCrCu<sub>0.5</sub>NiFe high-entropy alloy. *Materials Science and Engineering: A*. 2007 2007/05/25/;457(1):77-83.
66. Ng C, Guo S, Luan J, et al. Entropy-driven phase stability and slow diffusion kinetics in an Al<sub>0.5</sub>CoCrCuFeNi high entropy alloy. *Intermetallics*. 2012 2012/12/01/;31:165-172.

67. Sriharitha R, Murty BS, Kottada RS. Alloying, thermal stability and strengthening in spark plasma sintered  $\text{Al}_x\text{CoCrCuFeNi}$  high entropy alloys. *Journal of Alloys and Compounds*. 2014 2014/01/15/;583:419-426.
68. Tsai M-H, Wang C-W, Tsai C-W, et al. Thermal stability and performance of  $\text{NbSiTaTiZr}$  high-entropy alloy barrier for copper metallization. *Journal of the Electrochemical Society*. 2011;158(11):H1161-H1165.
69. Jiang L, Lu Y, Dong Y, et al. Annealing effects on the microstructure and properties of bulk high-entropy  $\text{CoCrFeNiTi}_{0.5}$  alloy casting ingot. *Intermetallics*. 2014 2014/01/01/;44:37-43.
70. Takeuchi A, Amiya K, Wada T, et al. Alloy designs of high-entropy crystalline and bulk glassy alloys by evaluating mixing enthalpy and delta parameter for quinary to decimal equi-atomic alloys. *Materials Transactions*. 2014:M2013352.
71. Zhang Y, Wang X, Li J, et al. Deformation mechanism during high-temperature tensile test in an eutectic high-entropy alloy  $\text{AlCoCrFeNi}_{2.1}$ . *Materials Science and Engineering: A*. 2018 2018/05/02/;724:148-155.
72. Xia S, Zhang Y. Deformation mechanisms of  $\text{Al}_{0.1}\text{CoCrFeNi}$  high entropy alloy at ambient and cryogenic temperatures. *Materials Science and Engineering: A*. 2018 2018/08/22/;733:408-413.
73. Huo W, Fang F, Zhou H, et al. Remarkable strength of  $\text{CoCrFeNi}$  high-entropy alloy wires at cryogenic and elevated temperatures. *Scripta Materialia*. 2017;141:125-128.
74. Hu BC, Chang YJ, Yeh AC, et al. Evolution of high temperature yield strength of  $\text{AlCoCrFeNiTi}$  high entropy alloys. *Procedia Manufacturing*. 2018;15:364-371.
75. Chen J, Zhou X, Wang W, et al. A review on fundamental of high entropy alloys with promising high-temperature properties. *Journal of Alloys and Compounds*. 2018;760:15-30.
76. Lim KR, Lee KS, Lee JS, et al. Dual-phase high-entropy alloys for high-temperature structural applications. *Journal of Alloys and Compounds*. 2017;728:1235-1238.
77. Qiu X. Microstructure and mechanical properties of  $\text{CoCrFeNiMo}$  high-entropy alloy coatings. *Journal of Materials Research and Technology*. 2020 2020/03/19/.

78. Hahn R, Kirnbauer A, Bartosik M, et al. Toughness of Si alloyed high-entropy nitride coatings. *Materials Letters*. 2019 2019/09/15/;251:238-240.
79. George EP, Curtin WA, Tasan CC. High entropy alloys: A focused review of mechanical properties and deformation mechanisms. *Acta Materialia*. 2020 2020/04/15/;188:435-474.
80. Gusarov A, Pohl C, Pfalz T, et al. Assessment of creep in reactor-irradiated CuCrZr alloy intended for the ITER first wall panels. *Fusion Engineering and Design*. 2018 2018/12/01/;137:112-123.
81. Kovacs A, Brown D, Ek F. Exothermic Reactions in the Partially Molten Li–Ni–Cu Alloy. *Journal of Condensed Matter Nuclear Science*. 2017 11/22;25.
82. Divinski S, Hisker F, Herzig C, et al. Self and Interdiffusion in Ternary Cu-Fe-Ni Alloys. *Defect and Diffusion Forum*. 2005 04/01/;237-240:50-61.
83. Rizal S, Homma H. Dimple fracture under short pulse loading. *International Journal of Impact Engineering*. 2000 2000/01/01/;24(1):69-83.
84. Shekhar S, Sarkar R, Kar SK, et al. Effect of solution treatment and aging on microstructure and tensile properties of high strength  $\beta$  titanium alloy, Ti–5Al–5V–5Mo–3Cr. *Materials & Design*. 2015 2015/02/05/;66:596-610.
85. Otto F, Yang Y, Bei H, et al. Relative effects of enthalpy and entropy on the phase stability of equiatomic high-entropy alloys. *Acta Materialia*. 2013 2013/04/01/;61(7):2628-2638.
86. Zhang Y, Jin K, Xue H, et al. Influence of chemical disorder on energy dissipation and defect evolution in advanced alloys. *Journal of Materials Research*. 2016;31(16):2363-2375.
87. Jin K, Lu C, Wang L, et al. Effects of compositional complexity on the ion-irradiation induced swelling and hardening in Ni-containing equiatomic alloys. *Scripta Materialia*. 2016;119:65-70.
88. Chen W-Y, Liu X, Chen Y, et al. Irradiation effects in high entropy alloys and 316H stainless steel at 300 °C. *Journal of Nuclear Materials*. 2018 2018/11/01/;510:421-430.

89. Lei Y, Hashimoto N, Isobe S. Cu-Containing High Entropy Alloys for Nuclear Fusion Application. MATERIALS TRANSACTIONS. 2020;advpub.
90. Stoller RE, Toloczko MB, Was GS, et al. On the use of SRIM for computing radiation damage exposure. Nuclear instruments and methods in physics research section B: beam interactions with materials and atoms. 2013;310:75-80.
91. Schäublin \* R, Yao Z, Baluc N, et al. Irradiation-induced stacking fault tetrahedra in fcc metals. Philosophical Magazine. 2005 2005/02/01;85(4-7):769-777.
92. Jien-Wei Y. Recent progress in high entropy alloys. Ann Chim Sci Mat. 2006;31(6):633-648.
93. Zinkle SJ, Snead L. Opportunities and limitations for ion beams in radiation effects studies: Bridging critical gaps between charged particle and neutron irradiations. Scripta Materialia. 2017 07/01;143.
94. de la Rubia TD, Averback RS, Benedek R, et al. Role of thermal spikes in energetic displacement cascades. Physical Review Letters. 1987 10/26;59(17):1930-1933.
95. Zhao S, Osetsky Y, Zhang Y. Preferential diffusion in concentrated solid solution alloys: NiFe, NiCo and NiCoCr. Acta Materialia. 2017;128:391-399.
96. Zhang Y, Stocks GM, Jin K, et al. Influence of chemical disorder on energy dissipation and defect evolution in concentrated solid solution alloys. Nature communications. 2015;6:8736.
97. Zinkle S. 1.03-Radiation-Induced effects on microstructure. Comprehensive nuclear materials. 2012;1:65-98.
98. Hashimoto N, Fukushi T, Wada E, et al. Effect of stacking fault energy on damage microstructure in ion-irradiated CoCrFeNiMnx concentrated solid solution alloys. Journal of Nuclear Materials. 2020 2020/11/01/:152642.
99. Yoshida N. Microstructure formation and its role on yield strength in AISI 316 SS irradiated by fission and fusion neutrons. Journal of Nuclear Materials. 1990 1990/11/02;174(2):220-228.
100. Lucas GE. The evolution of mechanical property change in irradiated austenitic stainless steels. Journal of Nuclear Materials. 1993 1993/11/02;206(2):287-305.

101. Busby JT, Hash MC, Was GS. The relationship between hardness and yield stress in irradiated austenitic and ferritic steels. *Journal of Nuclear Materials*. 2005 2005/02/01/;336(2):267-278.
102. Tan L, Busby JT. Formulating the strength factor  $\alpha$  for improved predictability of radiation hardening. *Journal of Nuclear Materials*. 2015 2015/10/01/;465:724-730.
103. Zinkle SJ, Busby JT. Structural materials for fission & fusion energy. *Materials Today*. 2009 2009/11/01/;12(11):12-19.
104. Luo H, Li Z, Raabe D. Hydrogen enhances strength and ductility of an equiatomic high-entropy alloy. *Scientific Reports*. 2017 2017/08/29;7(1):9892.
105. Fan JT, Zhang LJ, Yu PF, et al. Improved the microstructure and mechanical properties of AlFeCoNi high-entropy alloy by carbon addition. *Materials Science and Engineering: A*. 2018 2018/06/13/;728:30-39.
106. Moravcik I, Cizek J, Gouvea LdA, et al. Nitrogen Interstitial Alloying of CoCrFeMnNi High Entropy Alloy through Reactive Powder Milling. *Entropy*. 2019;21(4):363.
107. Enkovaara J, Rostgaard C, Mortensen JJ, et al. Electronic structure calculations with GPAW: a real-space implementation of the projector augmented-wave method. *J Phys: Condens Matter*. 2010;22(25):253202.
108. Perdew JP, Burke K, Ernzerhof M. Generalized Gradient Approximation Made Simple. *Phys Rev Lett*. 1996 10/28/;77(18):3865-3868.
109. Mortensen JJ, Hansen LB, Jacobsen KW. Real-space grid implementation of the projector augmented wave method. *Physical Review B*. 2005 01/21/;71(3):035109.
110. Zaddach AJ, Niu C, Koch CC, et al. Mechanical Properties and Stacking Fault Energies of NiFeCrCoMn High-Entropy Alloy. *JOM*. 2013 2013/12/01/;65(12):1780-1789.
111. Tang K, Wang T, Qi W, et al. Debye temperature for binary alloys and its relationship with cohesive energy. *Physica B: Condensed Matter*. 2018 2018/02/15/;531:95-101.
112. Smura CF, Parker DR, Zbiri M, et al. High-spin cobalt (II) ions in square planar coordination: structures and magnetism of the oxysulfides Sr<sub>2</sub>CoO<sub>2</sub>Cu<sub>2</sub>S<sub>2</sub> and Ba<sub>2</sub>CoO<sub>2</sub>Cu<sub>2</sub>S<sub>2</sub> and their solid solution. *Journal of the American Chemical Society*. 2011;133(8):2691-2705.

113. Kittel C, McEuen P, McEuen P. Introduction to solid state physics. Vol. 8. Wiley New York; 1996.
114. González C, Iglesias R, Demkowicz MJ. Point defect stability in a semicoherent metallic interface. *Physical Review B*. 2015 02/11/;91(6):064103.
115. Middleburgh SC, King DM, Lumpkin GR, et al. Segregation and migration of species in the CrCoFeNi high entropy alloy. *Journal of Alloys and Compounds*. 2014 2014/06/25/;599:179-182.
116. Niu C, Zaddach AJ, Oni AA, et al. Spin-driven ordering of Cr in the equiatomic high entropy alloy NiFeCrCo. *Appl Phys Lett*. 2015;106(16):161906.
117. Ma D, Grabowski B, Körmann F, et al. Ab initio thermodynamics of the CoCrFeMnNi high entropy alloy: Importance of entropy contributions beyond the configurational one. *Acta Mater*. 2015 2015/11/01/;100:90-97.
118. Zhao S, Egami T, Stocks G, et al. Effect of d electrons on defect properties in equiatomic NiCoCr and NiCoFeCr concentrated solid solution alloys. *Physical Review Materials*. 2018;2:013602.
119. Timoshevskii AN, Timoshevskii VA, Yanchitsky BZ. The influence of carbon and nitrogen on the electronic structure and hyperfine interactions in face-centred-cubic iron-based alloys. *Journal of Physics: Condensed Matter*. 2001 2001/01/25/;13(5):1051-1061.
120. Zhang X, Ren C-L, Han H, et al. Theoretical study of the substitutional solute effect on the interstitial carbon in nickel-based alloy [10.1039/C7RA01823A]. *RSC Advances*. 2017;7(33):20567-20573.
121. Zhang X, Ren C-L, Han H, et al. First-principles prediction of interstitial carbon, nitrogen, and oxygen effects on the helium behavior in nickel. *Journal of Applied Physics*. 2017;122(6):065901.
122. Paranjape P, Gopal P, Srinivasan SG. First-principles study of diffusion and interactions of hydrogen with silicon, phosphorus, and sulfur impurities in nickel. *Journal of Applied Physics*. 2019;125(12):125104.



123. Connétable D, Andrieu É, Monceau D. First-principles nickel database: Energetics of impurities and defects. *Computational Materials Science*. 2015 2015/04/15/;101:77-87.
124. Sakuraya S, Takahashi K, Hashimoto N, et al. The effect of point defects on diffusion pathway within  $\alpha$ -Fe. *Journal of Physics: Condensed Matter*. 2015 2015/04/02;27(17):175007.
125. Jain A, Ong SP, Hautier G, et al. Commentary: The Materials Project: A materials genome approach to accelerating materials innovation. *APL Materials*. 2013;1(1):011002.
126. Tang B, Jiang L, Hu R, et al. Correlation between grain boundary misorientation and M23C6 precipitation behaviors in a wrought Ni-based superalloy. *Materials Characterization*. 2013 2013/04/01/;78:144-150.
127. Sawada H, Kawakami K, Sugiyama M. Interaction between Substitutional and Interstitial Elements in  $\alpha$  iron Studied by First-principles Calculation. *MATERIALS TRANSACTIONS*. 2005;46(6):1140-1147.
128. Tian F, Varga LK, Chen N, et al. Ab initio investigation of high-entropy alloys of 3d elements. *Physical Review B*. 2013 02/26/;87(7):075144.